To the Graduate Council:

I am submitting herewith a thesis written by Bryan Randall Barnard entitled "Applied Stress Effects on the Isothermal and Cyclic High-Temperature Oxidation Behavior of Superalloys." I have examined the final electronic copy of this thesis for form and content and recommend that it be accepted in partial fulfillment of the requirements for the degree of Master of Science, with a major in Materials Science and Engineering.

Peter K. Liaw, Major Professor
_____

We have read this thesis
and recommend its acceptance:

Carl J. McHargue
_____

Thomas R. Watkins
_____

Accepted for the Council:

Carolyn R. Hodges, Vice Provost
and Dean of the Graduate School
_____

(Original signatures are on file with official student records.)

# APPLIED STRESS EFFECTS ON THE ISOTHERMAL AND CYCLIC HIGH-TEMPERATURE OXIDATION BEHAVIOR OF SUPERALLOYS

A Thesis
Presented for the
Masters of Science
Degree
The University of Tennessee, Knoxville

Bryan Randall Barnard
May 2008

# DEDICATION

I would like to dedicate this thesis to my parents, Mr. Randall Barnard and Mrs. Darless Barnard, and my brother, Mr. Brent Barnard, whose unending love, inspiration, and support have seen me through my time at the University of Tennessee; as well as to God for giving me the patience and endurance to overcome the numerous challenges that I've had to deal with during my time as a graduate student.

# ACKNOWLEDGEMENTS

I would like to thank my advisors, Drs. Peter K. Liaw and Raymond A. Buchanan, for all of their help and guidance throughout my graduate studies. I would also like to thank my committee members, Drs. Peter K. Liaw, Carl J. McHargue, and Thomas Watkins. I'm grateful for the help and advice of the co-authors of my publications, Drs. P. Liaw, R. Buchanan, B. Pint, W. Ren, E. Lara-Curzio, T. Watkins, D. L. Klarstrom, and Mr. L. Walker. I am also grateful to Drs. D. L. Klarstrom and L. Pike of HAYNES® International, Kokomo, IN, for providing the materials necessary to conduct the studies and for their helpful suggestions and comments on the research. I also thank DIRATS laboratories in Westfield, Massachusetts, for their help with the chemical analyses of the specimens. I would like to thank Dr. P. Tortorelli for his help, ideas, and critical comments regarding the research. I appreciate the assistance of Drs. J. E. Spruiell, T. T. Meek, D. C. Joy, G. Bhat, J. P. Shingledecker, W. Jiang, G. Wang, Y. Lu, G. Fan, M. Morrison, B. Peter, and R. Steward. I'm grateful for help from Mr. G. Garner, Mr. G. S. Bell, Mr. M. Neal, Mr. G. Jones, Mr. M. Benson, Mr. S. White, Ms. B. Green, Mr. T. White, Mr. D. Wiesner, Mr. B. Barlow, Mr. J. Holt, Mr. A. Keyser, Ms. L. Barker, Mr. C. Stephens, Mr. E. Huang, Mr. K. Johanns, Ms. L. Li, Mr. R. Mcdaniels, Ms. S. Maples, Ms. C. Lawrence, Ms. C. Winn, Ms. R. Cook, Mr. A. Pratt, Ms. D. Qiao, Mr. A. Chuang, Mr. F. Holiway, Mr. R. Stookesbury, Mr. D. Fielden, the UT machine shop, and Mr. J. M. Scott.

I gratefully acknowledge the financial support from the National Science Foundation (NSF), the Integrative Graduate Education and Research Training (IGERT) Program, under DGE-9987548, to the University of Tennessee (UT), Knoxville, with Drs. C. J. Van Hartesveldt, J. D. Giordan, D. Dutta, L. Clesceri, W. Jennings, and L. Goldberg as contract monitors, respectively. I would also like to thank HAYNES International, Inc. for providing the superalloy materials.

Portions of this research were sponsored by the Assistant Secretary for Energy Efficiency and Renewable Energy, Office of FreedomCAR and Vehicle Technologies, as part of the High Temperature Materials Laboratory User Program; and the Industrial Technologies Program, Industrial Materials for the Future Program, Materials Processing Laboratory Users Project, Oak Ridge National Laboratory. Both programs are managed by UT-Battelle, LLC, for the U. S. Department of Energy under contract number DE-AC05-00OR22725.

# Abstract

The effects of applied tensile stresses on the isothermal and cyclic oxidation behavior of two nickel-based superalloys, HAYNES® 75® and HAYNES® 230®, were investigated through measurements of specific mass change, oxide morphology and thickness, degree and depth of internal oxidation, compositional changes in and around the oxide scales, and x-ray diffraction. Here, an applied tensile stress generally led to larger Cr/Ni ratios in the oxide scales, greater chromium depletion in areas directly under the oxide scales, lower specific-mass-change values, and thinner oxide scales. These improvements in oxidation resistance are attributed to a greater concentration of dislocations, defects, etc. in the grain boundaries caused by the applied stress. These defects could act as fast diffusion paths for the Cr atoms to diffuse to the surface, causing a reduction in the duration of the less-protective transient-oxidation period and promoting faster formation of the more protective $Cr_2O_3$ layer.

Overall, the 230-alloy specimens demonstrated better oxidation and creep resistance than the 75-alloy specimens, likely due to their compositional differences, and the 230 alloy's larger average grain size. The oxide scales of the 230-alloy specimens were generally thinner and formed at slower rates than those of the 75-alloy specimens. The 230-alloy specimens also demonstrated fewer internal oxidation penetrations than those of the 75 alloy under all conditions.

The effects of the applied stresses on the residual-stress states of substrates and surface oxides were characterized using x-ray diffraction. For both substrates and oxides, residual strains were compressive. Substrate residual strains were smaller in magnitude

than those in the oxides due to relative thickness effects between oxide and substrate, and possibly to recovery and creep surface-residual-stress-relief processes in the substrate. For stressed specimens, these processes were possibly enhanced by dislocation creep. The residual stresses in the substrates were still compressive likely due to internal oxidation effects as well as a shallow x-ray penetration depth.

# TABLE OF CONTENTS

# LIST OF TABLES

**Part I.**

# LIST OF FIGURES

# 1.0 Introduction

Elevated-temperature corrosion/oxidation is a leading cause of failure among engineering components that are expected to perform at high temperatures. Nickel-based superalloys, such as the two materials chosen for this study, HAYNES® 230® and HAYNES® 75® alloys, are candidate materials for such high-temperature engineering components. The 75 alloy has been employed in several low-stress fabricated-part applications in the aerospace and gas-turbine industries and is used in general industrial-heating applications [1]. The 230 alloy is employed in gas and land-based turbine engine combustors, and other key stationary components [1]. The 230 alloy is also utilized in superheater tubes, baskets and fixtures in the heat-treating and industrial-heating industries [1]. Further, the 230 alloy is used in the chemical/petrochemical process industry for such applications as supports for nitric acid catalyst grids [1]. Other applications for the 230 alloy include: high-temperature expansion bellows, wire-annealing fixtures, conveyor fixtures, retorts, dampers, and substrate holders in the semiconductor industry [1]. The 230 alloy has additional applications in fossil-energy plants [1].

Nickel-based superalloys are selected as high-temperature engineering components due to their ability to form oxide surface layers that protect the alloy substrates from further negative effects of elevated-temperature corrosion [2-8]. It is due to their excellent resistance to aggressive environments that heat-resistant Ni-Cr-containing alloys are used in such applications as nuclear reactors, electrical-resistance heating, and in the petrochemical and heat-treating industry [9-11]. Nickel-based superalloys and Ni-Cr alloys specifically are often employed in gas turbines as turbine-

disc components, which operate at temperatures of up to around 700°C [3]. Specifically, these components include: gas-turbine blades and vanes [4]. Nickel-based alloys are also being considered for used in supercritical steam plants [12]. Additionally, cast alloys based in the Ni-Cr system are also employed within porcelain-fused-to-metal dental restorations [13]. While oxidation studies of nickel-based superalloys are common in literature, very few studies have attempted to characterize the effects of applied stresses on their oxidation behavior [13-16]. Cyclic temperature changes are also a common condition encountered by elevated-temperature components [2-3]. The aforementioned changes in stress state and temperature can also impact a material's residual-stress distributions. Residual stresses are known to play an important part in the failure mechanisms of materials [17-18]. Thus, the subject of this thesis is to characterize the effects of applied stresses on the oxidation properties and the residual-stress states of the two superalloy materials under isothermal and cyclic oxidation conditions.

The extent of oxidation for stressed and unstressed specimens of the two superalloys will be studied by examining the thicknesses of the oxide layers and the extent of internal-oxidation damage by light microscopy. Since oxidation is often accompanied by an increase in specimen mass, specific mass change as a function of oxidation time data will be collected and compared for stressed and unstressed specimens. Scanning-electron-microscopy (SEM) studies will be conducted on plane-view specimens in order to characterize possible differences caused by the applied stresses on the oxide morphologies of the alloy specimens. Electron-microprobe analyses (EMPA) will be employed in order to analyze possible changes in the elemental composition in and around the oxide scales due to the applied stresses. X-ray diffraction

will be employed in order to examine and compare the residual-stress states of stressed and unstressed specimens in their oxide layers and alloy substrates. The findings of this research will be useful to HAYNES® International and will further future studies in this research area.

# 2.0 Literature Review

## 2.1 Materials

As stated previously, the research in this study was conducted on two nickel-based, chromia-forming superalloys, HAYNES® 75® and HAYNES® 230®.

### (a) HAYNES® 75® Alloy

The 75 alloy is a solid-solution strengthened alloy and is advertised to have moderate strength up to temperatures of 650°C [1]. The 75 alloy is employed mostly in high-temperature, low-stress applications where "reasonable oxidation resistance" is required [1]. No useful information could be found in literature regarding this alloy.

### (b) HAYNES® 230® Alloy

The 230 alloy is also solid-solution strengthened [1]. The 230 alloy is advertised to have the most favorable balance of such high-temperature properties as strength, thermal stability, oxidation resistance, thermal-cycling resistance, and fabricability in comparison with other major high-temperature alloys. It is advertised to have "excellent high-temperature strength" and is effective at 650°C or higher "for very long-term applications [1]." A cyclic-oxidation study was found in the literature for the HAYNES® 230®, HR-120®, and HR-160® alloys, where the alloys were oxidized for 2 years at 982°C and 1 year at 1,093°C, 1,149°C, and 1,204°C [2]. Each thermal cycle in the study was comprised of 30 days at the desired temperatures, followed by around 4 hours at ambient temperatures [2]. All of the alloys were attacked internally "in the form of internal oxidation and void formation," which was the main cause of degradation [2]. The 230 alloy outperformed the two other alloys at almost every temperature because it "exhibited partial scale spallation," which allowed for an "easier formation of a

protective or semiprotective $Cr_2O_3$-rich scale during subsequent oxidation" [2]. This trend was attributed to the fact that the 230 alloy contained about 0.02 wt.% La [2]. Additions of the reactive element lanthanum decrease the amount of oxide scale spallation at alloying contents less than about 1.0 weight percent (wt.%) [2]. The 0.02 wt.% La in the 230 alloy provided a stronger adhesion at the interface of the substrate and its oxide layer [2]. Two additional studies involving the 230 alloy found that it demonstrated "the slowest oxidation kinetics," and therefore, the best oxidation resistance of a group of alloys consisting of Inconel 625, Inconel 718, and Hastelloy X, when subjected to several thousand hours of oxidation in air at 800 to 1,100°C [19], and when oxidized for several hundred hours in wet hydrogen at 700 to 1,100°C [20]. In both studies, the specimens were allowed to cool and then were removed from the furnaces at various times throughout the studies in order to record mass-change values [19-20]. Another study involving the 230 alloy found that its oxidation resistance was clearly superior to an alloy known as Crofer 22APU when cyclically oxidized every 24 hours for 1,400 hours at 750°C and just over 300 hours at 800°C [21].

## 2.2 Oxidation of Nickel-Based Alloys

Very little oxidation-related information could be found on the above HAYNES® alloys in the literature, and no information was available on how applied stresses influence the oxidation of these alloys. However, a great deal of information was available in the literature on the oxidation of nickel-based superalloys, and Ni-Cr alloys of similar compositions, mostly Ni-20Cr alloys.

Ni-Cr containing alloys were created to resist high-temperature corrosion in high-oxygen-activity atmospheres [9, 22]. The chromium content of these alloys endows them

with the resistance to oxidation and sulfidation [10]. The oxidation rate of materials tends to increase with increasing chromium contents of up to 7%, and for up to 9% chromium, internal oxidation takes place, thus depleting the amount of chromium in the matrix [10]. To offset the effects of this depletion, Ni-Cr alloys are made up of around 18-20%Cr to be reasonably resistant to the effects of oxidation [23]. There is a marked reduction in the values of the parabolic oxidation rate constants, $k_p$s, in the case of binary Ni-Cr alloys if the amount of Cr present is increased from around 10 to 20 wt.% [24]. Also, it has been reported that a chromium content of above 20% is needed to obtain favorable resistance to carburization [9]. The amount of Cr is kept below 30 wt.% in order to allow for the addition of other elements that provide favorable mechanical properties as well as oxidation resistance [3]. In addition, chromium contents of over about 50% cause the oxidation properties to deteriorate towards values that are similar to those of metallic chromium [10].

The high nickel content of these alloys helps provide resistance to oxidation, nitriding, and carburization [10]. The high nickel content is also the major factor in promoting resistance to halogen gases as well as chloride and molten alkaline salts [10]. Al has often been added to Ni-Cr alloys because it has been proven to be beneficial to the resistance of oxide scale-spallation [2]. Solid-solution strengthening and favorable high-temperature mechanical properties have been introduced into nickel-based alloys by alloying with Mo, W, and Ta [3].

Most high-temperature alloys that are employed in commercial applications are dependent on the formation of protective chromium oxide ($Cr_2O_3$) scales for resistance to oxidation and carburization at high temperatures and prolonged service lives [2, 9-10]. In

fact, for applications in a temperature range of 600-1,000°C, the best protection is usually provided by a layer of $Cr_2O_3$ [5]. Provided that these scales are adherent to the surface of the material, and are coherent, continuous, dense, slow-growing, thermodynamically stable, compact, and free from cracks and pores, they provide the material with a degree of resistance to the effects of elevated-temperature corrosion in oxidizing, carburizing, sulfidizing, and/or chloridizing environments [3, 5-6]. This phenomenon is due to the fact that an oxide layer is able to reduce the rate of oxidation by impeding the diffusion of reacting species [6]. In order to achieve the best protection against oxidation, this coherent and continuous oxide layer must not only be formed, but also maintained [2]. Therefore, the alloy must have an adequate supply of chromium to initially form the protective oxide layer, and the diffusive supply of chromium in the underlying substrate must also be adequately high for the continued growth of the protective oxide layer to be maintained [2]. The need for continued growth of the protective oxide layer is to offset the effects of cracking and spalling of pieces of the oxide during service.

In addition to the formation of a protective $Cr_2O_3$ oxide layer, NiO and $NiCr_2O_4$ (a spinel) oxide layers have been identified at some conditions as well [10]. The presence of the additional oxide layers is due to the fact that even though chromia can form immediately in grain boundaries during the initial stages of oxidation due to a greater rate of chromium diffusion in the grain boundaries and preferential nucleation sites, oxides that contain nickel form on the outer grain surfaces and grow much faster than chromia [23, 25]. Therefore, a great deal of the less-protective NiO and $NiCr_2O_4$ will form prior to the formation of a continuous chromia layer [23]. This effect is commonly referred to as transient oxidation [23]. Transient oxidation is an effect that is common to alloys

operating at elevated temperatures, and it can affect the formation of the most stable oxides [23]. In Ni-Cr alloys, the effects of transient oxidation can be decreased by certain variables, such as increased chromium contents, that promote a faster formation of the chromia layer [23].

The growth of the underlying chromia scales is due to the countercurrent, grain-boundary diffusion of oxygen and chromium, and islands of new chromium oxide form first at grain boundaries of the material [25-26]. A layer of the continuous chromia then forms near grain boundaries and diffuses laterally from the grain boundaries all along the grains due to the coalescence of chromia islands [5, 25]. The degree of the lateral diffusion increases as the oxidizing temperature increases [25]. If there is a sufficient degree of lateral diffusion of chromium, a continuous $Cr_2O_3$ oxide layer will form under the initially-formed Ni-containing oxide layers after a critical time period [25]. This time period is necessary to connect the islands of chromia through the lateral diffusion process along the oxide-substrate interface [25]. Since the outward diffusion of chromium is greater than that of the inward diffusion of oxygen, the formation of the new oxide occurs in the outer portion of the oxide layer [26]. Further oxidation will then be controlled by transport through the $Cr_2O_3$ scale [4]. The chromia scale is more stable than Ni-containing oxide scales, and thus, the initially formed Ni-containing oxide layers will be reduced by chromium due to a displacement reaction involving chromium and NiO [3]. However, the formation of the continuous chromium-oxide layer will cause a depletion of chromium in the alloy substrate, and this depletion increases as the thickness of the $Cr_2O_3$ scale increases [25]. A schematic diagram of this process is presented in the Appendix section as Figure 1. Tables appear in Appendix A, and figures appear in Appendix B.

Figure 1 (f) is an exaggeration of the final result of the oxidation process. The oxide will be comprised mostly of $Cr_2O_3$ after a sufficient time at a suitable temperature. However, some portion of nickel-containing oxides will likely remain in the scale.

## 2.3 Mechanical testing and temperature

### (a) Possible Effects of Applied Load on Oxidation

Though knowledge of an oxide's mechanical properties is considered important [27], there are very few studies of the effect of applied load on the oxidation processes of materials, particularly superalloys, in the literature. Of those studies found [7, 9, 14-15, 19, 28], there are two schools of thought on the effects that applied stresses may have on oxidation processes. The first school of thought is that mechanical stresses and deformations could significantly reduce the oxidation resistance of a material due to an increase in oxide scale cracking [14]. This increase in oxide scale cracking is due to the fact that cracking of an oxide layer due to creep deformation occurs at smaller strain-values than the failure of the metal, because oxide layers are generally more brittle than the metal substrates [28]. Also, oxide cracking under applied stress may result from the oxide layer's inability to keep up with the substrate strain by either plastic flow or lateral growth [28]. One possible result of the cracking of the oxide layer is a local loss of protection, known as spallation or delamination of the oxide, which would cause an increased level of corrosion [28]. The majority of oxide layers, which form on heat-resistant materials, possess the ability to restore the protective effects of the oxide layers [28]. This phenomenon is known as crack healing [28]. However, the degree of internal corrosion could be increased due to repeated cracking of the oxide layer [28]. Internal corrosion changes the mechanical properties of the alloy and has been known to increase

the susceptibility of the base metal to crack formation [28]. The application of tensile strains could also reduce the oxidation resistance of an alloy by increasing its surface area that will be subjected to oxidation, which would, in turn, increase the total amount of oxidation for the material in question [28]. The main point of this school of thought is that applied stresses will reduce oxidation resistance and lead to a greater amount of oxidation as compared with unstressed materials.

The results of a previous study [15] seem to support the previously-mentioned philosophy. This study conducted creep tests under oxidizing conditions on 200-μm thick strips of Ni - 20 wt.% Cr for 120 hours or less in the temperature range of 500 - 900°C. At each temperature, the oxide obtained was much thicker than that found or calculated from the literature for specimens of equivalent composition, oxidized without applied stresses at the same temperatures [15]. The oxide-scale thickness also increased with increasing temperature [15]. However, the study also determined that in the temperature range of 600 - 900°C, the application of a tensile load modified neither the oxide layer nature nor oxide morphology [15].

Two additional studies comparing oxidation in stressed vs. unstressed conditions also found greater damage due to oxidation in stressed specimens [9, 22]. However, the experiments of these two studies were conducted in very different atmospheres than those of this study. Most of the oxidation temperatures were also outside the range of those employed in this study. The first study involved high-temperature oxidation and creep tests on Ni-Cr-Fe alloys under carburizing and oxidizing conditions (1,000°C for 1,000 hours in a gas mixture of $CO$-$H_2O$-$H_2$). A protective $Cr_2O_3$ oxide layer formed and remained stable under normal oxidizing conditions [9]. However, when companion creep

tests were conducted under low strain rates, the authors observed: carburization of grain boundaries, oxidation, grain-boundary sliding, carbon uptake, carbide precipitation, fast internal oxidation of carbides, significant reduction of cohesion in the oxide scale, chromium depletion, and repeated oxide cracking localized in or near grain boundaries [9]. For high strain-rate creep tests, carburization was not localized to grain boundaries, but had happened all over the bulk of the material due to the fact that the faster creep caused "a higher stationary density of cracks" to form in the oxide scale, leading to a greater amount of carbon uptake in the material [9]. Internal carbide formation decreased the material's ductility considerably, and voids and cavities were formed [9]. Finally, the material failed by brittle fracture [9].

The second study involved examining the effects of mode-I stresses on the oxidation of a Ni-20Cr alloy wire specimens in a sulfur-dioxide atmosphere [22]. At temperatures below 550°C, microcracks, attributed to chromium enrichment of the surface caused by the applied stresses, formed on sample surfaces, when mode-I stresses were applied [22]. At 700°C under stress, cracking was not observed and a corrosion layer of constant thickness formed [22]. Corrosion was also observed to take place along grain boundaries [22]. Additionally, the external stresses caused an increase in the reaction rate at 700°C [22]. The increased reaction with the harmful sulfur-containing atmosphere caused the protective character of the oxide layer to be continually destroyed [22].

The second school of thought on the subject of the effects of applied stresses on oxidation is that, at least over intermediate oxidizing time periods, applied stresses may increase the oxidation resistance of a material. The increase in oxidation resistance could

be caused by the ability of mechanical stresses and deformations to influence the growth kinetics and mechanisms of oxide scales by: causing excess vacancies on grain boundaries and increasing short-circuit diffusion; possibly annihilating the cation vacancy flux at the substrate/oxide interface; producing plastic flow, which increases the dislocation density and the number of vacancy sinks; modifying the number of short-circuit diffusion paths and influencing diffusivities by accelerating diffusion due to the presence of additional dislocations / defects caused by deformation [14, 28]. Additionally, if tensile deformation causes an increased amount of oxidation to form at the grain boundaries, the lateral growth of the oxide, previously associated with the formation of the protective chromia oxide layer [25], could be responsible for a greater amount of oxide formation [28]. These effects could modify the type of oxides formed, which could change the scale adhesion and oxidation properties [14].

The second school of thought also accounts for why damage to an oxide scale caused by an applied stress might not result in greater oxidation rates / damage due to oxidation, at least over moderate time periods. Simultaneous cracking and rapid diffusion of elements to the surface to reform, or heal, the protective oxide layer, also referred to as pseudoplasticity, and superplastic behavior of an oxide are two of the methods by which an oxide scale may mitigate damage due to applied stress [14]. Also, deformation of the substrates caused by the applied stress may reduce vacancies due to increased dislocation densities and result in wavy interfaces between oxide and substrate, both of which could improve the adherence of oxide layers to alloy substrates, thereby reducing the chance for spallation of the protective scales [14].

A study consisted of oxidizing two ribbons of Ni-20Cr of 0.15 mm thickness in the temperature range of 550 - 830°C for under 300 minutes [7]. A tensile load was applied to one specimen, while the other was only oxidized at the same temperature [7]. For all four temperatures studied, 550, 650, 750, and 830°C, the application of the tensile load caused a quicker decrease in the amount of nickel on the surface of the specimen and a quicker increase in the amount of Cr on the surface, suggesting that the tensile load increased the rate of formation of the protective $Cr_2O_3$ layer [7]. This effect would decrease the non-protective, transient stage of oxidation and lead to greater oxidation resistance over intermediate time periods. However, the increased rate of formation of the protective $Cr_2O_3$ layer caused by the tensile load probably also serves to deplete the chromium reservoir of the alloy faster, thus, guaranteeing a shorter material lifetime.

The effects of creep on oxidation are greatly dependant on the mechanical properties of the oxide layers [28]. Under these conditions, the oxide layer's integrity is of great importance in protecting the metal substrate from further corrosion [28].

**(b) Possible Effects of Thermal Cycling on Oxidation**

While information regarding the oxidation-rate constants and the oxidation mechanisms for alloys can be obtained in isothermal-oxidation tests, thermal cycling is typically required for high-temperature component testing for industrial applications [3]. These tests are carried out due to the fact that the likeliness of failure of a protective $Cr_2O_3$ scale is greater in situations that involve thermal cycling [2]. Since the conditions involved in thermal cycling are known to cause the spallation of protective oxide scales, the conditions of thermal cycling are widely regarded as being "more severe" than conditions of isothermal oxidation [3]. In these situations, the component material must

undergo several heating and cooling cycles over the course of its service lifetime [2]. Because oxides have lower thermal-expansion coefficients than their alloy substrates, thermal stresses are brought about when a temperature change occurs [2]. These thermal stresses can cause the oxide scale to crack and eventually spall [2]. As the alloy substrate becomes depleted of chromium due to the repeated cracking and spalling of the oxide scale, less protective oxides will form [2]. Therefore, the lifetimes of materials in high-temperature applications often depend on whether or not the oxide layer stays whole and protective or whether it breaks or spalls off during cyclic temperature changes or under applied stresses [10]. Nickel-chromium alloys generally outperform iron-based chromium-containing alloys when examined under conditions of thermal cycling, due to the fact that there is a smaller difference in the thermal expansivity between the oxide scale and the substrate [10]. This trend, in turn, causes the stress values at the oxide-substrate interface to be lower [10]. The effects of thermal cycling are still a concern for nickel-chromium alloy components and, thus, will be examined in this study.

Cyclic oxidation of Ni-Cr alloys has been studied at length [2-4]. Stresses arise in oxide scales during cyclic oxidation that consist of growth stresses caused by the change in volume of the material brought about by the growth of a surface oxide layer and thermal stresses that are caused by the thermal-expansion mismatch between the oxide layer and its alloy substrate [3, 6]. Diffusional creep and grain-boundary sliding under elevated-temperature conditions are useful for alleviating the growth stresses caused by thermal cycling [3]. However, the thermal stress, which is related to the difference in thermal-expansion coefficients of alloy and oxide, the amount of temperature change, and oxide thickness / mass gain, cannot be relieved [3]. The continuing increase in thermal

stress caused by the temperature change may result in such affects as: oxide cracking, a more serious degree of internal oxidation, chromium depletion, a reduction in activation energy, and/or spallation of the protective oxide scale [3-4, 6, 29]. The spallation may be due to some combination of: oxide-scale buckling, shear stresses generated along the substrate / oxide interface during cooling, the joining of cracks within the oxide, and / or interfacial cracks caused by defects, voids, vacancies, flaws, etc. that act as stress concentrators [6]. In situations where the Cr concentration of an alloy is too low, Cr depletion affects the alloy's ability to reform chromia after a spallation, leading to the formation of less-protective Ni-based oxides [3]. However, the thermal-cycling conditions in these studies are not considered "aggressive," and may not cause spallation.

**(c) Residual Stresses**

Residual stresses are self-equilibrating stresses that occur in a material or sample because two or more volumes within the sample are joined together such that each volume is constrained to a size other than the one it would take if it were free to expand or contact. Further, there are no external forces applied to the sample. Since residual stresses play an important part in many types of material-failure processes, residual-stress information is invaluable for predicting the strength of many engineering components [17]. While the formation of coherent and continuous oxide surface layers, such as $Cr_2O_3$ for Cr-containing alloys, can protect the alloy substrate against the damaging effects of high-temperature corrosion [2, 5, 30-31], this formation can lead to significant residual stresses [32]. The magnitude of this residual stress in an oxide layer is of great importance in understanding the failure processes of oxides [18]. Some information was available in the literature concerning the use of x-ray diffraction to determine residual-

stress values in $Cr_2O_3$ and/or NiO layers [33-38] and sometimes even in their underlying substrates as well [33-34]. Therein, residual stresses in oxide scales are composed of two kinds. The first kind of residual stresses are growth stresses that occur during the isothermal growth of the oxide scale and are believed to be generated by such phenomena as: epitaxial stresses, point defect stresses, recrystallization stresses, formation of additional oxide within an already established oxide scale, changes in volume or composition in the alloy or oxide scale, and specimen geometry [18, 23, 30, 32]. The second kind of residual stresses are the aforementioned thermal stresses that arise during cooling due to the coefficient of thermal-expansion mismatch between oxide and alloy [33-36]. However, the magnitude of these stresses may be somewhat relieved due to creep of the substrate material [18, 23, 30]. The growth-stress portion of the residual-stress values are often considered negligible when compared to the thermal-stress portion [33, 37-38]. Large compressive residual stresses were observed in the oxide scales [33, 35-38]. The magnitude of these stresses were reported as: ~ -1,000 to –3,300 MPa by one study [33], as high as –3,600 MPa in another study [35], as high as -2.9 GPa by an additional study [36], and between ~ -1,275 and –2,600 MPa in two other studies [37-38]. The magnitude of these stresses can be affected by such factors as oxidation time and temperature, and oxide and substrate thickness [33, 36-38]. Residual-stress values in the substrates were found to be smaller than those observed in the oxide scales [33-34]. A NiCr substrate demonstrated compressive residual-stress values with a maximum value of -300 MPa, significantly smaller than the residual-stress values on the oxides [33]. The substrate residual-stress values were ascribed mostly to internal oxidation of grain boundaries, which lead to compressive stresses in surrounding areas of the substrate [33].

Substrate residual-stress values have been reported to vary with oxidation time and rate [33]. Additionally, it is known that the residual-stress states of materials, such as superalloys, can be modified by thermal, mechanical, and thermomechanical loads [39-40], such as those encountered in this study.

# 3.0 Experimental Procedure

## (3.1) Overview

The gravimetric method was selected to study the oxidation behavior of the specimens due to "its directness and general convenience" [41]. The gravimetric method includes: weighing and measuring dimensions of samples, oxidizing them, reweighing and examining them by x-ray diffraction and metallographic techniques [23, 41]. The 75 alloy was considered to be a simple Ni-Cr alloy that was selected to serve as a baseline for these studies. The 230 alloy is considered to be a more complex alloy with minor alloying additions that are useful for improving oxidation resistance.

## (3.2) Independent Chemical Analyses

The first stage in the analysis of the materials was to cut approximately 5-gram square specimens out of the sheets sent by HAYNES® International. These specimens were sent to DIRATS Laboratories in Westfield, Massachusetts, for independent chemical analyses. The purpose of these analyses was to compare the data with manufacturer-supplied chemical-composition information, as well as to obtain information on the amounts of oxygen and nitrogen present in the as-received alloys. The results of these analyses were compared with chemical-composition data supplied by HAYNES® International, and the relatively comparable data sets for both alloys are listed in Table 1. The amounts of carbon and sulfur in the alloys were determined by combustion. The amounts of oxygen and nitrogen in the alloys were determined by means of the Inert Gas Method (IGF). The amounts of all other elements present in the alloys were determined by Inductively Coupled Plasma Spectrometer - Optical Emission Analysis (ICP-OE).

### (3.3) Oxidation Experiments Under No Stress

Isothermal and cyclic oxidation experiments were conducted in laboratory air in order to determine oxidation mechanisms and reaction kinetics of these alloys [3, 23]. These experiments were conducted in Lindberg resistively-heated tube furnaces. The cyclic-oxidation experiments consisted of ten 100-hour cycles at either 700 or 800°C. In between cycles, the specimens were given time to equilibrate, and their mass-change values were recorded. Specimens for these experiments were rectangular coupons with the nominal dimensions of 10 × 19 × 0.8 mm for the 75 alloy and 10 × 19 × 1.1 mm for the 230 alloy.

### (3.4) Oxidation Experiments Under Stress

Oxidation experiments under applied stresses at elevated temperatures (creep experiments) were also performed. The specimens for these experiments were dog-bone shaped tensile specimens with the nominal dimensions of 159 × 32 × 0.8 mm for the 75 alloy and 159 × 32 × 1.1 mm for the 230 alloy. The dimensions of the reduced sections of the tensile specimens were approximately 57 × 13 mm. Creep furnaces used in these experiments were Marshall Varian creep furnaces, model #1134, with Barber-Colman model #560 temperature controllers. Creep experiments were conducted with specimens sealed within environment chambers inside the furnaces so that the specimens could be protected in an Argon atmosphere during the heating and cooling portions of the experiments. The Argon gas consisted of 99.999% Argon with less than two parts per million oxygen and less than one part per million moisture. Upon reaching temperature, the Argon atmosphere was displaced with laboratory air from a blower, and the

specimens were loaded so that the surfaces of the specimens could oxidize under the applied stresses. Dial gages were used to measure the elongation of the specimens.

### (3.5) Oxidation Rate Analyses

Most research indicates that similar alloys oxidized at similar temperatures to those selected in this investigation follow parabolic oxidation [3-4, 26, 42-43]. If oxidation follows this equation, the oxide should be protective, and further oxidation should be controlled by diffusion through the oxide scale [5, 41-44]. The parabolic oxidation-rate equation based on specific mass change due to oxidation is:

$$\Delta m^2 = k_p t, \tag{1}$$

where $\Delta m^2$ is the square value of weight gain per unit area, $k_p$ is the oxidation-rate constant normally given in units of $g^2\ cm^{-4}\ sec^{-1}$, and t is time at the given temperature [41, 45]. Oxidation rate constants can also be obtained as a function of oxide thickness. The parabolic oxidation rate equation based on oxide thickness is described by:

$$x^2 = k_p' t + \text{constant}, \tag{2}$$

where x is oxide thickness and $k_p'$ is the oxidation-rate constant normally given in units of $cm^2\ sec^{-1}$ [19-20, 23, 30, 41, 44, 46-47].

### (3.6) SEM / EMPA

After the experiments were completed, the oxide morphology of all specimens was characterized by a Leo 1525 scanning-electron microscope (SEM) at an accelerated voltage of 20 keV. Following these analyses, the specimens were cross-sectioned, copper-plated, mounted in epoxy, and polished to a mirror finish for further SEM analyses and electron-microprobe analyses (EMPA) using a JEOL 8200 electron

microprobe in order to determine oxide thickness, extent of internal corrosion, and compositional changes in the oxide scale and the base metal.

**(3.7) X-ray Diffraction**

Table 2 lists the details of the experimental conditions for the x-ray measurements. Briefly, a 4-axis ($\Phi$, $\chi$, $\Omega$, $2\Theta$) goniometer [48] was employed for the stress measurements using the "$\Omega$-goniometer geometry [49]" and parallel beam optics, which eliminates sample surface displacement errors [49-50]. Due to the fact that reflections in the high 2-theta range were desired for maximum strain sensitivity the (3 3 1) and (4 2 0) reflections from the alloy were utilized for the strain measurements. The (4 1 6) reflection from the eskolaite ($Cr_2O_3$) phase was utilized for the strain measurements of the oxide layers of both alloys as it possessed the most discernable peak in the high 2-theta range. During scanning, the specimens were oscillated ± 2 mm in plane and rocked ± 5° around the $\chi$–axis to improve particle statistics for the substrate peaks [(3 3 1) and (4 2 0) peaks]. Replicate residual-stress measurements were taken for the (3 3 1) peaks of the 230-alloy specimen oxidized isothermally under 72.5 MPa of applied stress and the 230-alloy specimen oxidized cyclically under 72.5 MPa of applied stress. The (4 2 0) peaks of the 75-alloy specimen oxidized cyclically under no stress and the as-received 75-alloy specimen also received replicate stress measurements. These replicate measurements were taken for the purpose of obtaining representative standard deviation values for all of the residual-stress measurements.

Specimen alignment was accomplished using a dial-gauge probe, which was accurate to ± 5 μm. Here, the relative distance to the center of rotation is known, and the diffracting surface is positioned accordingly. Goniometer alignment was ensured by

examining $LaB_6$ powder on a zero background plate. The maximum observed peak shift for the (510) reflection of $LaB_6$ (141.7 °2Θ) was less than 0.01 °2Θ for Ω tilting as described in Table 2.

The stresses were calculated using the Dölle-Hauk method [49, 51], assuming a uniaxial stress state. The fully-expanded equation relating strain to stress is:

$$\varepsilon_{\phi\psi} = (d_{\phi\psi}-d_0)/d_0 = (1+\nu)/E \bullet \{\sigma_{11}\cos^2\phi + \sigma_{12}\sin 2\phi + \sigma_{22}\sin^2\phi - \sigma_{33}\} \bullet \sin^2\psi + (1+\nu)/E \bullet \sigma_{33} - \nu/E \bullet (\sigma_{11} + \sigma_{22} + \sigma_{33}) + (1+\nu)/E \bullet \{\sigma_{13}\cos\phi + \sigma_{23}\sin\phi\} \bullet \sin 2\psi \,, \quad (3)$$

and may be reduced to

$$\varepsilon_{\phi\psi} = (1+\nu)/E \bullet \sigma_{11} \bullet \sin^2\psi - \nu\sigma_{11}/E, \quad (4)$$

assuming $\sigma_{12}=\sigma_{22}=\sigma_{13}=\sigma_{23}=\sigma_{33}=\phi=0$. ε, d, ν, E and σ are the strain, interplanar spacing, Poisson's ratio, Young's modulus, and stress, respectively. The room-temperature Young's modulus values for each alloy ($E_{75}$ = 221 GPa and $E_{230}$ = 211 GPa) were taken from manufacturer data and selected as the E-values for the alloy peaks. The E-value for the oxide peaks ($E_{chromia}$ = 273 GPa) was obtained from a reference [27]. The room-temperature Poisson's ratio for the 230 alloy ($\nu_{230}$ = 0.32) was taken from manufacturer data to be the ν - value for the alloy peaks of the 230 specimens. The ν - values for the 75 alloy and oxide peaks were both estimated to be 0.3. The variables and subscripts ϕ, ψ, and 0, refer to the azimuthal angle, tilt angle, and strain-free angle, respectively. $d_{\phi=0,\psi=0}$ was taken as the strain-free interplanar spacing, $d_0$, for the alloy substrates. In the case of the oxide surface layers, $d_0$ was determined from the x-ray data, employing the analysis of Hauk et al [49].

# 4.0 Results

## (4.1) Creep

Creep strain rate versus time data are presented in Figures 2 (a) and (b) for the 75 and 230 alloys, respectively. The temperature and stress values were selected with the objective of approximating a lifetime's worth of creep damage for each specimen within the 1,000-hour oxidation period. The applied-stress values were interpolated from manufacturer data to be approximately 75% of the stress-value to cause rupture for each material in sheet condition at each temperature. The chosen applied stress values were well under the interpolated 0.2%-offset yield-strength values for each material in sheet condition at each temperature (~ 220 MPa for the 75 alloy at 700°C, ~ 122 MPa for the 75 alloy at 800°C, ~ 254 MPa for the 230 alloy at 700°C, ~ 249 MPa for the 230 alloy at 800°C), though. An additional creep experiment consisting of a 75-alloy specimen at 800°C with a reduced stress value of 6.7 MPa was also conducted in order to determine the effects of the degree of applied stress on oxidation. Another reason for the additional creep experiment was that the 75-alloy specimen under the reduced stress did not experience tertiary creep, making it a better comparison for the creep behavior of the 230-alloy specimens. Figure 2 (a) reveals that the 75-alloy specimens at 700°C under an applied stress of 37.7 MPa and at 800°C under an applied stress of 13.5 MPa exhibited periods of primary creep followed by abbreviated periods of secondary creep around 200 and around 135 hours, respectively. Both specimens then abruptly transitioned into a tertiary creep phase. Under the reduced stress, the 75-alloy specimen exhibited a period of primary creep up until around 300 hours, followed by a period of secondary creep. No

tertiary creep was observed for this specimen. The 230-alloy specimens [Figure 2 (b)] under applied-stress values of 133 MPa at 700°C and 72.5 MPa at 800°C experienced a period of primary creep and transitioned into a secondary or steady-state creep period at around 250 hours. No tertiary phase of creep damage was observed.

**(4.2) Oxidation Mass Gain**

Figure 3 presents the specific mass-change values, measured in mg of mass gain due to oxidation divided by the specimen surface area in $cm^2$. A second set of values is presented for the unstressed specimens for comparison purposes. Figure 4 presents oxidation data for specimens of both alloys oxidized cyclically with and without stress at 800°C. The slopes of the linear portions of these curves are proportional to the parabolic rate constants. Cyclic-oxidation experiments under stress at 700°C were not conducted due to time and equipment constraints. The oxidation rate constants ($k_p$-values) for each specimen as well as its specific mass gain under each condition are listed in Table 3 in order of increasing $k_p$-value. The values of specific mass change for unstressed specimens are about two to three times greater than those of the stressed specimens (see Figure 3). This trend is consistent with the rates approximated from Fig. 4. In the case of the reduced-stress 75-alloy specimen, reducing the applied stress value by approximately one half did not seem to have a dramatic effect on the specific mass-change value.

To a first approximation, spallation of the oxide layers under the applied stresses was not significant / noticeable when examining the surfaces of the stressed specimens. However, spallation of the oxide layers under applied stress could not be entirely ruled out due to the fact that no fixture was available for the collection of possible oxide spallation for specimens oxidized under applied stress (creep experiments).

### (4.3) Oxide Surface Morphology

Figures 5 (a) to (e) and 6 (a) to (c) are plane-view SEM micrographs of 75-alloy specimens oxidized isothermally and cyclically, respectively, under various conditions of temperature and stress. Figures 7 (a) to (d) and 8 (a) to (c) are plane-view SEM micrographs of 230-alloy specimens oxidized isothermally and cyclically, respectively, under various conditions of temperature and stress. These figures were used to examine the effects of the various oxidizing conditions on the surface morphology of specimens. Figures 5 (a) and (c) reveal that when oxidized isothermally at 700°C, the oxide microstructure of the 75 alloy specimen goes from a moderately coarse, grainy structure with small amounts of faceting in the unstressed condition to a coarser, more heavily faceted structure at 800°C. Figures 5 (b) and (d) reveal that the application of stress has the opposite effect on oxide morphology. The degree of faceting is reduced, and a finer, more nodular structure develops. Figure 5 (e) suggests that when the amount of stress applied is reduced by roughly half, the degree of faceting increases. For the 230 alloy specimen oxidized at 700°C [Figure 7 (a)], the microstructure goes from a fine microstructure to a much more coarse faceted microstructure at 800°C [Figure 7 (c)]. In the stressed condition at 800°C [Figure 7 (d)] some faceting is present, but largely the microstructure of the 230-alloy becomes finer and more nodular. For the 230 alloy specimen oxidized under stress at 700°C [Figure 7 (b)], a microstructure consisting of a few large faceted crystals and many thin rod-like structures developed. It is unclear as to what mechanism caused this effect. Perhaps the change in microstructure is due to the fact that this specimen was under the greatest degree of stress (133 MPa). Faceting is observed in the unstressed condition at 800°C in specimens of both alloys [Figures 5 (c)

and 7 (c)]. The faceted structures were larger for the 75 alloy, but located more uniformly across the surface of the 230 alloy. When stress was applied, however, a comparison could not be made, as both microstructures appeared similar. This trend was also observed for the cycled/unstressed [Figures 6 (a) and (b) and Figures 8 (a) and (b)] vs. cycled/stressed specimens to some extent [Figures 6 (c) and 8 (c)].

**(4.4) Oxide Thickness and Internal Oxidation**

Figures 9 (a)-(e) through Figures 10 (a)-(c) and Figures 11 (a)-(d) through Figures 12 (a)-(c) are SEM images of cross-sectioned specimens of the 75 and 230 alloys, respectively. The specimens were copper-plated in order to protect the oxides from damage that might be incurred during preparation for these analyses. Table 3 contains oxide-thickness and standard-deviation data for all specimens. Oxide scales were thicker at 800°C than at 700°C, and 230-alloy oxides were generally thinner than 75-alloy oxides (see Figure 13). In contrast to the specific mass-change data, the oxide-thickness data did not show large changes for the conditions tested. For example, the applied stresses did not greatly modify the oxide thicknesses at 700°C or at 800°C for the isothermally-oxidized 230-alloy specimens. For the 230-alloy specimen oxidized isothermally at 800°C under an applied stress of 72.5 MPa [Figure 11 (d)], there are gaps between the oxide and the copper plating as well as between the oxide and the alloy substrate. These gaps were not considered in the oxide-thickness calculations. For the 230-alloy specimen oxidized cyclically for ten 100-hour cycles at 700°C [Figure 12 (a)], most of the oxide is concentrated on the left side of the image, with much thinner portions to the right of the figure. While the trends in the oxide-thickness data generally follow those of the specific mass-change data, the oxide-thickness data was not considered as representative of each

sample as a whole, due to the fact that the thickness measurements were taken from one image of a small portion of each oxide scale.

Table 3 also contains data on the average and maximum depth of internal-oxidation penetrations (thin protrusions of oxide from the scale down into the substrate). The average and maximum depth of internal oxidation penetrations increased at 800°C, as compared with specimens oxidized at 700°C. Though the application of stress generally caused the number of oxide penetrations to increase, the average and maximum depth of the penetrations decreased under the applied stress. The 230-alloy specimens oxidized cyclically at 800°C (stressed vs. unstressed) are the exceptions to this trend. Reducing the stress for the 75-alloy specimen oxidized isothermally at 800°C caused a decrease in both the average and maximum depth of internal oxidation penetrations.

### (4.5) Composition in and around Oxide Scales

Figures 14 (a) to (d) and 15 (a) to (e) are images / elemental maps of the cross-sections of 75-alloy specimens oxidized isothermally at 700°C and 800°C, respectively, generated by an electron microprobe. At 700°C, the Cr map contained many chromium-rich regions within the bulk [Figure 14 (c)]. At 800°C, the number of these regions was reduced, as the higher temperature promoted faster Cr diffusion to the surface [Figure 15 (c)]. Al was prevalent in the internal-oxidation penetrations at 800°C [Figure 15 (e)]. 75-alloy specimens oxidized isothermally under applied stress [Figures 18 (a) to (d), 19 (a) to (e), and 20 (a) to (e)], and those that were thermally cycled [Figures 23 (a) to (d) and 24 (a) to (e)], demonstrated similar trends between 700 and 800°C as those that were isothermally oxidized under no stress.

The isothermally-oxidized 230-alloy specimens at 700 and 800°C [Figures 16 (a) to (e) and 17 (a) to (f), respectively] also exhibited greater Cr diffusion out of the bulk and into the surface from 700 to 800°C [Figures 16 (c) and 17 (c), respectively]. Tungsten-rich precipitates [Figures 16 (e) and 17 (f)] at the two temperatures, and Al-rich internal-oxidation penetrations [Figure 17 (e)] at 800°C were observed in the bulk of the 230-alloy specimens. These trends were also exhibited in the 230-alloy specimens oxidized isothermally under applied stress [Figures 21 (a) to (e) and 22 (a) to (f)], and those that were thermally cycled [Figures 25 (a) to (e) and 26 (a) to (f)]. Thermally-cycled specimens under applied stress at 800°C of the 75 and 230 alloy [Figures 27 (a) to (e) and 28 (a) to (f), respectively] demonstrated similar trends to other specimens oxidized at 800°C. Other than an increase in the number of internal oxidation penetrations in specimens oxidized under applied stress, no significant differences in oxide composition were apparent among specimens oxidized under applied stresses, those that were thermally cycled under no stress, those that were thermally cycled under stress, and those that were isothermally oxidized under no stress using elemental mapping. Thus, more quantitative features of the microprobe were utilized.

Figures 29 (a) and (b) show concentration versus depth data from the electron microprobe for 75- and 230-alloy specimens, respectively. The Cr-profiles (purple lines) revealed Cr-depleted zones characterized by dips in the Cr-profiles encountered within the first few microns beneath the oxides. These Cr-depleted zones were due to Cr diffusion to the surface. The depletion parameter, A, was estimated by choosing a value where each Cr profile first became roughly horizontal again ($Cr_0$), and summing the differences between the depleted Cr-content points on the Cr profile and the $Cr_0$ value:

$$A = \sum^{x}_{0} Cr_0 - Cr_x, \quad (5)$$

where x is the particular depth. The results appear in Figure 30. The general trend was that the applied stress increased the Cr depletion parameter. However, the reduced-stress 75-alloy specimen had a greater depletion parameter than its higher-stress counterpart. Another exception was the cyclically-oxidized 75-alloy specimens at 800°C. Figure 31 contains maximum Cr/Ni ratio data taken by the electron microprobe within the oxide scales. The general trend was that the applied stress increased the Cr/Ni ratio. Inexplicably, the reduced-stress 75-alloy specimen had a higher Cr/Ni ratio than its higher-stress counterpart. Specimens without error bars in Figures 30 and 31 represent conditions in which only one reliable measurement was obtained.

### (4.6) Phase Identification

Theta-2theta patterns were obtained for specimens of both alloys using CuKα radiation at a wavelength of 1.540590 Angstroms, a step size of 0.02°, and a rate of 1° per minute for all scans (see Figures 32 and 33). Analyses of all the patterns using Jade software revealed the presence of a face-centered cubic (fcc) nickel-rich phase, an eskolaite phase ($Cr_2O_3$), and an unknown oxide spinel phase, possibly manganese iron chromium oxide.

### (4.7) Residual Stress (Oxides)

Analyses of the strain versus $\sin^2\psi$ plots for the oxides of both alloys revealed that the oxides of both alloys under all conditions studied exhibited linear, negative-sloping strain vs. $\sin^2$psi behavior. An example plot is presented in Figure 34. The residual-stress values for each sample condition are presented in Table 4. The residual stresses in the oxide scales ranged from 1.19 to 1.79 GPa and appeared to be independent

of sample condition. The residual-stress values in the oxides were plotted against the parabolic oxidation rate constants (see Figure 35) to determine if the oxidation rate would have a major effect on the residual-stress values in the oxides. However, no discernable trend between oxidation rate and residual stress could be obtained for the oxide scales.

**(4.8) Residual Stress (Substrates)**

Initial $\sin^2\psi$ plots showed much scatter and oscillatory behavior (see Figure 36) due to the large grain size present in the alloys. While each individual strain measurement was valid and correct showing interaction strains or elastic incompatibility strains between large grains, the heterogeneity displayed was not further interpretable. This problem was partially overcome by incorporating ± 5° chi rocking during peak measurement, which minimized the influence of the large grains by sampling over a larger number of grains. After incorporating chi rocking, strain vs. $\sin^2\psi$ plots took on a more linear, negative-sloping trend (see Figure 37), which allowed for a sensible residual-stress determination. Residual-stress values of the alloy substrates were found to be significantly less than those of the oxide surface layers. Standard deviation values were obtained from two samples of each alloy. As time constraints would not permit further replicate measurements, the largest obtained standard-deviation values were taken to be representative for the other samples of a particular alloy. The averaged values of residual stress for the two peaks, (331) and (420), were plotted against the parabolic oxidation rate constants (see Figure 38) in order to observe possible correlations between oxidation rate and residual stress in the underlying substrates. With the exception of one or two outliers, the general trend was that an increase in the oxidation rate yielded a decrease in the residual-stress values of the underlying substrates.

## 5.0 Discussion

Overall, the 230-alloy specimens demonstrated better oxidation (see Table 3) and creep (see Figure 2) resistance than the 75-alloy specimens, likely due to compositional differences, and a larger average grain size, which is known to reduce creep rates under certain conditions due to its ability to impede diffusional flow [54]. The oxide scales of the 230-alloy specimens were generally thinner and formed at slower rates than those of the 75-alloy specimens. The 230-alloy specimens also demonstrated less internal oxidation damage than those of the 75 alloy under all conditions.

Since the $k_p$-values in Table 3 are a measure of the rate of oxidation for specimens, these values were used to rank the severity of the effects of the various conditions (temperature, applied load, alloy composition, and thermal cycling) on the overall oxidation process of the two alloys. The $k_p$-values in Table 3 reveal that oxidation temperature has the greatest effect on the oxidation rates. As expected, oxidation increased as the temperature increased from 700 to 800°C. Within each oxidation temperature, applied stress had the next largest impact on $k_p$, with each stressed specimen demonstrating a lower $k_p$-value than its unstressed counterpart. Although less distinct, alloy composition seemed to be the third most important factor related to $k_p$, as the 230 alloy's $k_p$-values were less than those of the 75 alloy's in each recorded condition. Thermal cycling did not seem to have a significant impact on the $k_p$-values. This effect was likely to the fact that there were only ten 100-hour cycles. For comparison, Waspaloy, Astroloy, and Udimet 720 alloy samples that were cycled for 50 minutes at 1,000°C for at least 250 cycles initially showed weight gain due to oxidation, just as observed for the isothermally-oxidized specimens [3]. However, after around 70

to 100 cycles, periods of weight loss due to spallation were observed for only the cyclically-oxidized materials [3]. Other effects caused by the thermal cycling were irregular oxide / substrate interfaces, a greater degree of internal oxidation for specimens, and one of the materials developed a thicker, less protective oxide layer that contained a large concentration of transition oxides [3].

The $k_p$ values obtained in this study were similar to those found in the literature for alloys of similar compositions. One source lists the $k_p$ values of Waspaloy, Astroloy, and Udimet 720 alloy specimens oxidized at 750°C for around 750 to 1,000 hours to be $1.6 \times 10^{-14}$, $2.7 \times 10^{-14}$, and $6.6 \times 10^{-14}$ $g^2$ $cm^{-4}$ $s^{-1}$, respectively [3]. The Waspaloy is similar in composition to the 230 alloy, which had a $k_p$ value of $0.8 \times 10^{-14}$ $g^2$ $cm^{-4}$ $s^{-1}$ at 800°C. The oxidation rate constant for Hastelloy X was found to be $3.73 \times 10^{-14}$ [($g^2$ / $cm^4$) / sec] when oxidized at 760°C for 600 hours [4]. Table 5 contains nominal composition information for Astroloy, Hastelloy X, Udimet 720, and Waspaloy. For a Ni-20Cr foil of 200 μm thickness oxidized at 700°C, a $Cr_2O_3$ layer was found to grow at a rate of $4.3 \times 10^{-15}$ $g^2$ $cm^{-4}$ $s^{-1}$, and at a rate of $3.3 \times 10^{-14}$ $g^2$ $cm^{-4}$ $s^{-1}$ when oxidized at 800°C [25]. At 700°C, the parabolic oxidation constants for thermally-cycled specimens for both alloys employed in these studies were on the order of 2 to $7 \times 10^{-16}$ $g^2$ $cm^{-4}$ $s^{-1}$, while the $k_p$'s of isothermally-oxidized specimens were on the order of 1 to $2 \times 10^{-15}$ $g^2$ $cm^{-4}$ $s^{-1}$. These values are lower than those of the Ni-20Cr foil oxidized at 700°C, although the isothermally-oxidized $k_p$ values are close to the value of $4.3 \times 10^{-15}$ $g^2$ $cm^{-4}$ $s^{-1}$ for the Ni-20Cr foil. This result was expected due to the fact that our alloys have additional elements not present in the Ni-20Cr foils that likely improve oxidation

resistance. At 800°C, the stressed specimens of the 230 alloy had $k_p$ values around $4 \times 10^{-15}$ $g^2$ $cm^{-4}$ $s^{-1}$. The $k_p$ values of all other specimens and conditions are between 1 and 9 $\times 10^{-14}$ $g^2$ $cm^{-4}$ $s^{-1}$. Overall, the $k_p$ values for specimens in these studies obtained at 800°C were in good agreement with those obtained on similar materials at 750, 760, and 800°C in other studies, and indicate that applied tensile loads caused an order of magnitude reduction in oxidation rate of the 75 and 230 alloys.

The application of a load under oxidizing conditions generally resulted in lower specific mass-change values and thinner oxide scales (see Figures 3 and 13 and Table 3), indicating slower oxidation rates under the applied stress. These results differ from the results obtained in another study [15] and were contrary to the expectations of the researchers. A possible explanation for the slower oxidation rates of stressed specimens is likely rooted in the formation of oxide layers on a typical Ni-20Cr alloy.

In the early stages of oxidation, a continuous NiO layer forms on the outer grain surfaces, while $Cr_2O_3$ islands form in the grain boundaries [25]. As the outer NiO layer grows into the metal, it encounters islands of $Cr_2O_3$, resulting in the formation of $NiCr_2O_4$ spinel islands [23]. Since Ni-containing oxides are less protective than $Cr_2O_3$, considerable amounts of NiO and $NiCr_2O_4$ form before the more protective $Cr_2O_3$ layer forms underneath the nickel-containing oxide layers [23]. This effect is known as transient oxidation [23]. Because they are less protective, oxide scales containing higher amounts of nickel are thicker. Since the applied stresses in this study generally caused the oxide scales to be thinner, it was reasoned that faster diffusion of chromium along the grain boundaries to the alloy surface was causing the faster formation of the protective layer. The application of load under oxidizing conditions resulted in larger Cr/Ni ratios

in the oxide scales and greater chromium depletion areas directly under the oxide scales. These trends point to faster Cr diffusion to the alloy surfaces and shorter transient oxidation periods. A faster diffusion rate of Cr to the surface of an alloy of similar composition when stress was applied is supported by the results of another study [7].

The mechanism by which the applied stresses may influence diffusivities in a material is thought to be increased dislocation densities [14, 28] at the grain boundaries. Tensile deformation has been thought to modify transient oxidation rates, and promote preferrentially the formation of chromia layers over mixed oxide-spinel layers [14]. Thus, it is speculated that the applied stress causes more defects to form in the grain boundaries of the alloys. As previously stated, chromia forms immediately in grain boundaries during the initial stages of oxidation due to a greater rate of chromium diffusion in grain boundaries and preferential nucleation sites [23, 25]. The growth of the chromia scales is due to the countercurrent, grain-boundary diffusion of oxygen and chromium [25-26]. Thus, these grain-boundary defects could be helping to promote the selective oxidation of Cr, as opposed to Ni or Fe, by acting as fast diffusion paths for the Cr atoms in the grain boundaries. This effect would increase the diffusional flux of Cr ($J_{Cr}$) in the stressed specimens and result in a faster formation of the chromia layer. A schematic of this process appears in Figure 39. Although the Cr-depletion area and Cr/Ni atomic percentage results of Figures 30 and 31 are all within a large range of error, the trends suggest that the applied stress may be causing the faster formation of a more Cr-rich oxide scale. The faster formation of the protective chromia layer may have reduced the transient-oxidation period, improved oxidation resistance in the stressed specimens over the intermediate time period, and resulted in the thinner oxides and lower specific

mass-change values. Though the oxide-thickness results of Figure 13 are within the range of error at each temperature, the trend suggests that at 800°C, applied stresses generally resulted in thinner oxide scales. The faster formation of the chromia layer would result in faster depletion of Cr in the alloy, which would likely result in less favorable oxidation properties over longer time periods (5,000 to 10,000 hours or more).

Calvarin-Amiri et al. observed no change in oxide morphology and thickness between stressed and unstressed oxidized specimens [15]. The discrepancy with the results of Calvarin-Amiri et al. [15] may be due to the differences in oxidation periods of the two studies. The oxidation times of the previous study were all less than 120 hours, whereas those of the current study's were around 1,000 hours [15]. The faster diffusion rate of chromium to the surface of the alloy and quicker formation of protective oxide caused by the applied stress may not have occurred as completely after only 120 hours. More favorable oxidation properties might be obtained over a longer (e.g., 1,000-hour) time period.

The ability of the oxide layers to remain intact and show no evidence of cracking on the surfaces of the stressed specimens is curious. Some oxide scale deformation under stress has been observed without total failure of the scale [14]. This deformation is attributed to simultaneous cracking and rapid healing / re-oxidation of the oxide layer known as pseudoplasticity [14]. At higher temperatures, pseudoplasticity can cause the critical-strain value to cause failure in an oxide scale to increase by several times the critical-strain value to cause failure when the oxide is assumed to behave in a mostly elastic manner [52]. Schütze reported that a smooth oxidized surface with no visible cracks was observed on a ferritic-steel specimen with an addition of Ce. The specimen

had been oxidized at 800°C in air under a total strain of 28.8% [53], which is comparable to the highest total strain amount in the stressed specimens of this study. Cracking of the scale was reported to have occurred by acoustic-emission measurements, but rapid healing of the oxide filled in the cracks making them unnoticeable upon subsequent inspection [53]. Superplastic behavior in the oxide scales is also a possible explanation [14]. Additionally, adherence of the oxide layers to the alloy substrates can be enhanced by plastic deformation of the substrates in that deformation could help annihilate vacancies by increased dislocation densities [14]. Deformation may also cause interfaces to be wavy, which would result in improved adhesion of oxides to alloy substrates [14].

Significant compressive residual-stress values were observed for the oxides of all specimens. It has been reported elsewhere that the growth of an oxide layer on an oxidation-resistant material substrate can generate large, normally compressive, stresses in an oxide layer [23, 30, 32]. Residual-stress values in the –1,000 to –3,300 MPa range were reported for $Cr_2O_3$ oxide layers on a NiCr alloy [33], and a range of –1,275 and –2,600 MPa were reported by two other studies for $Cr_2O_3$ oxide layers on a Ni-30Cr alloy [37, 38]. Theoretical calculations of residual stresses in $Cr_2O_3$ oxide layers formed on Ni-30Cr alloys typically have values of around -3.5 GPa [36-38]. Another reference places theoretically-calculated residual-stress values of $Cr_2O_3$ oxide layers formed on NiCr alloys in the range of -4 to -4.5 GPa [33]. A method proposed by Virkar was employed in this study to calculate the oxide residual stresses for the two alloys [55]. These calculations are based on the free strain, $\Delta\varepsilon_o$, being dependent upon the thermal-expansion mismatch between the scale and the substrate [i.e. $\Delta\varepsilon_o = |(\alpha_{scale} - \alpha_{substrate})\,\Delta T|$; where $\alpha_{Cr2O3(scale)} = 7.4 \times 10^{-6}\ °C^{-1}$, $\alpha_{75(substrate1)} = 16.5 \times 10^{-6}\ °C^{-1}$, $\alpha_{230(substrate2)} = 15.2 \times$

$10^{-6}$ °$C^{-1}$, $\Delta T$ = temperature change, $E_{Cr2O3(scale)}$ = 273 GPa, $E_{75(substrate1)}$ = 221 GPa, $E_{230(substrate2)}$ = 211 GPa] [1, 27]. The predicted oxide residual-stress values employing Virkar's method were -2.2 GPa for the oxides of the 75 alloy specimens, and -1.9 GPa for the oxides of the 230 alloy specimens. While these values were closer to the measured results of this study, they still overestimated the magnitude of the residual stresses in the oxides. This overestimation is quite common and is attributed to the fact that most theoretical models of oxide residual stress do not take into account the effects of stress relaxation during cooling [33, 37-38]. Stress relaxation for Ni-30Cr alloys has been attributed to creep of both the oxide and the substrate, and cracking and spalling of the oxide layers [33, 35]. Although, cracking and spallation were not observed in the oxides of the 75- and 230-alloy specimens to a significant extent, the oxide layers are not totally homogeneous, which could lead to the mitigation of the residual stress.

As previously stated, the residual-stress values of the alloy substrates in this study were much lower in magnitude than those of their oxides, but they were still compressive in nature (see Table 4). A lower residual-stress magnitude was expected in the substrates due to the fact that there is a sizeable thickness difference between the oxides and their alloy substrates [33]. That is, the same amount of force in the thin oxide is distributed over the much thicker substrate. Calculations of substrate residual-stress values were performed for this study employing the method proposed by Virkar [55] and predicted tensile residual-stress values of 10 MPa in the substrate of the 75 alloy, and 4 MPa in the 230 alloy in order to balance the compressive stresses of the oxides [33]. It was reported by Huntz that an oxidized NiCr substrate demonstrated compressive stresses within the x-ray penetration depth, with the maximum-recorded value being -300 MPa [33]. Substrate

stresses of <0, ~0, -30, and between -100 to -200 MPa were also reported [33]. The small-magnitude, compressive stresses reported were attributed to the effects of internal oxidation, particularly in grain boundaries, which induced compressive stresses in surrounding zones [33]. The compressive stresses in the oxide and the substrate were apparently balanced by tensile stresses located deeper in the substrate [33]. For the 75 and 230 alloys, the issue may also be related to the penetration depth of the x-rays employed. A depth penetration calculation described by Cullity [56] was conducted for the two alloys employing the equation:

$$G_x = (1 - e^{-2\mu x/\sin\theta}), \quad (6)$$

where x is the penetration depth, $G_x$ is the total diffracted intensity contributed by a surface layer of depth x, $\mu$ is the material-dependent linear absorption coefficient, and $\theta$ is the diffraction angle [56]. This calculation revealed that much of the x-ray signal was coming from a depth of around 5 μm for the 75 alloy, and around 4 μm for the 230 alloy, indicating that much of the alloy signal emanated from the nickel metal in the oxide layer.

As previously stated, an increase in the oxidation rate was generally accompanied by a decrease in residual stress for the underlying substrates (Figure 38). A speculative trend in oxidation rate vs. residual stress was found for the oxide scales (Figure 35). It has been stated that specimens under applied stresses generally exhibited slower oxidation rates, which translated into lower $k_p$ values. This trend was believed to be due to the generation of defects in the grain boundaries, which acted as fast diffusion paths for Cr atoms, and caused faster diffusion of Cr to the alloy surfaces to form more protective oxide scales. At low values of $k_p$, the trends in Figures 38 and 35 could be

interpreted as the residual stress becoming more tensile and less compressive, respectively, suggesting the redistribution of force (or free strain) due to increased scale thickness. However, no explanation can be offered for the higher $k_p$ values at this time. X-ray penetration depth may also contribute to the trend exhibited in the residual stress vs. oxidation rate data (Figure 38). Greater oxidation rates translate to thicker oxides. If the oxide is thicker, the x-rays will not penetrate as deeply into the substrate, where it is likely that larger stresses are present to balance the stresses in the oxide scales.

An increase in the magnitude of residual stress was expected for the substrates of the stressed specimens due to creep and plastic deformation. However, this result was not observed to any great extent. An explanation of the lack of increase in the residual-stress magnitude of the substrates of stressed specimens was therefore desired.

The residual stresses in the substrate materials of this study may have been partially relieved under the thermo-mechanical processing. For example, significant relief of surface residual stresses (~500 to 650 MPa) due to shot peening was observed in nickel-based superalloy materials subjected to elevated-temperature conditions (~ 550 to 700°C) [39-40, 57], and the greatest degree of stress relief occurred in the early hours of exposure to elevated temperatures [40, 57]. The degree of stress relief was proportional to temperature. Residual stress relief was also observed in specimens subjected to greater applied stresses/strains under elevated temperatures [40, 57].

The increase in residual-stress relaxation experienced under thermomechanical loading is thought to be due to a complex interaction of the thermal and mechanical mechanisms of stress relief [39-40, 57]. For the purely thermal component of residual stress relief, these studies observed a rapid decrease in residual stresses followed by a

slower period of stress relief, followed in turn by the stabilization of residual-stress values [39-40, 57]. The initial period of rapid residual-stress relief, recovery, was thought to be due to the diffusion-assisted rapid annihilation and reorganization of crystalline defects such as dislocations, vacancies, etc. [39-40, 57]. The materials in this study are mostly Ni-Cr alloys comprised largely of nickel. Self-diffusion data in the relevant temperature range (540-1,400°C) for nickel was obtained [58], and used to calculate a diffusion coefficient of approximately $2.74 \times 10^{-14}$ $cm^2/sec$ [58]. Most of the diffusion constants for Cr or Ni atoms within Ni-Cr alloys obtained from this reference had to be taken from temperature ranges (~950-1,400°C) [58], which was just outside the relevant temperature range (700 to 800°C) for this study. Values for the diffusion coefficients were calculated to be in the range of $\sim 10^{-13} - 10^{-15}$ $cm^2/sec$. Diffusion coefficients in this study are likely to be slightly lower due to the lower temperature range (700 to 800°C).

The second/slower period of residual-stress relief was thought to be due to creep mechanisms in the substrate [57]. The thermal processes of residual-stress relief have been shown to be amplified by the application of stress [57]. As previously stated, some of the specimens in these studies were subjected to applied loads at elevated temperatures (see Figure 2). The applied stress ($\sigma$) / shear modulus (G) criterion obtained from Dieter was used to determine the creep mechanism for the alloys under the given conditions [59]. The potential creep mechanisms were: dislocation glide ($\sigma / G > 10^{-2}$), dislocation creep ($10^{-4} < \sigma / G < 10^{-2}$), and diffusion creep ($\sigma / G < 10^{-4}$) [59]. Shear moduli at the relevant temperatures for the two alloys were calculated from the equation:

$$G = E / (2 \times (1+\nu)), \quad (7)$$

where E is Young's modulus and ν is Poisson's ratio [59]. Table 6 contains information related to these calculations. This analysis revealed that the predicted mechanical mechanism for these alloys and conditions should be dislocation creep [59]. Dislocation creep is due to the process of dislocation glide, which is enhanced by vacancy diffusion [59].

## 6.0 Summary and Conclusions

The following conclusions were drawn from the results of this study:

1. The application of a load under oxidizing conditions generally resulted in lower specific mass-change values at 800°C, thus indicating a slower oxidation rate under the applied stress. Very little difference in specific mass-change values was observed when stress was applied at 700°C under oxidizing conditions.
2. The application of a load under oxidizing conditions generally leads to larger Cr/Ni ratios in the oxide scales, greater chromium depletion areas directly under the oxide scales, and thinner oxide scales at 800°C. These trends point to faster chromium diffusion to the alloy surfaces and shorter transient oxidation periods.
3. The application of stress resulted in a less-faceted oxide morphology possibly due to the deformation of large faceted oxide crystals.
4. In comparison with the 75-alloy specimens, the 230-alloy specimens demonstrated better creep resistance likely due to their larger average grain sizes, and better oxidation resistance likely due to their greater chromium contents and minor alloying additions.
5. Large (compressive) residual stresses in the range of -1.19 to -1.79 GPa were observed in the oxide layers likely due to thermal and growth stresses associated with oxide formation. These stresses appeared to be independent of sample condition.

6. After incorporating a $\chi$-rocking technique to mitigate grain-size effects and any preferred orientation, strain vs. $\sin^2\psi$ plots for alloy substrates demonstrated a near-linear, negative-sloping (compressive) behavior.
7. Residual stresses in the substrate materials were observed to be much smaller than those observed in the oxide layers, due to relative thickness effects between oxide and substrate, and possibly surface residual-stress relief by the diffusion-assisted rapid annihilation and reorganization of crystalline defects, as well as creep mechanisms in the unstressed specimens. These stresses were still compressive likely due to internal oxidation effects as well as x-ray penetration depth issues.
8. A complex interaction of the previously-mentioned phenomena with a mechanical mechanism, likely dislocation creep, may have been partially responsible for substrate stress relief in specimens oxidized under an applied stress.

## 7.0 Future Work

Future work should include stressed and unstressed, cycled and/or isothermal oxidation experiments at other temperatures, time durations, and stress levels for the 75- and 230-alloys, as well as other high-temperature alloys. Future studies should also involve more replicate measurements in order to enhance the certainty of the trends in the data. The results of these experiments should be incorporated into a database, which will allow for the modeling and prediction of applied stress effects on the oxidation of high-temperature alloys. A thermodynamic analysis, which includes the effects of applied stress, should also be conducted.

The oxidation rate constants calculated from specific mass-change values, $k_p$s, are a function of specimen area. Under applied stresses, however, the specimen area may be changing with time as a specimen elongates due to creep. A way of accounting for specimen area change under applied stress is needed to obtain accurate oxidation rate constants under applied stress. There were large differences in specimen area between stressed and unstressed specimens as well as differences in the heating rates of the furnaces used to oxidize unstressed versus stressed specimens. The latter concern was somewhat moderated by employing Argon during the heat-up and cool-down phases of the stressed experiments. Future studies should attempt to address these issues.

In the stressed conditions, no fixture for the collection of potential oxide spallation was available. Judging from the oxidized surfaces of the stressed specimens, spallation did not seem to be significant, but a total lack of spallation cannot be stated for certain. Future studies should incorporate a method for the collection of potentially spalled oxide from stressed specimens.

# References

1. Haynes Website, www.haynesintl.com.
2. B. Gleeson and M. A. Harper, "The Long-Term Cyclic-Oxidation Behavior of Selected Chromia-Forming Alloys," Oxidation of Metals, Vol. 49, Nos. 3/4, pgs. 373-399, 1998.
3. J. H. Chen, P. M. Rogers, and J. A. Little, "Oxidation Behavior of Several Chromia-Forming Commercial Nickel-Base Superalloys," Oxidation of Metals, Vol. 47, Nos. 5/6, pgs. 381-410, 1997.
4. A. Khee and A. R. Spencer, "Oxidation of a Nickel-Chromium-Base Alloy-RA 333," Oxidation of Metals, Vol. 7, No. 1, pgs. 71-76, 1973.
5. H. J. Grabke, R. Dennert, and B. Wagemann, "The Effect of S, N, and C on the Oxidation of Ni-20%Cr and Fe-20%Cr," Oxidation of Metals, Vol. 47, Nos. 5/6, pgs. 495-506, 1997.
6. Y. Zhang and D. A. Shores, "Study of Cracking and Spalling of $Cr_2O_3$ Scale Formed on Ni-30Cr Alloy," Oxidation of Metals, Vol. 40, Nos. 5/6, pgs. 529-553, 1993.
7. J. F. Schmitt, N. Pacia, P. Pigeat, and B. Weber, "Study of the Initial Oxidation of a Ni-20Cr Alloy in the Temperature Range 550-830°C: Influence of Mechanical Deformation," Oxidation of Metals, Vol. 44, Nos. 3/4, pgs. 429-452, 1995.
8. N. Hussain, K. A. Shalid, I. H. Khan, and S. Rahman, "Oxidation of High-Temperature Alloys (Superalloys) at Elevated Temperatures in Air: I," Oxidation of Metals, Vol. 41, Nos. 3/4, pgs. 251-269, 1994.
9. A. Schnass and H. J. Grabke, "High-Temperature Corrosion and Creep of Ni-Cr-Fe Alloys in Carburizing and Oxidizing Environments," Oxidation of Metals, Vol. 12, No. 5, pgs. 387-404, 1978.
10. W. Z. Friend, Corrosion of Nickel and Nickel-Base Alloys, John Wiley and Sons, New York, New York, 1980.
11. F. A. Khalid and S. E. Benjamin, "The Effect of Deformation Substructure on the High-Temperature Oxidation of Inconel 625," Oxidation of Metals, Vol. 54, Nos. 1/2, pgs. 63-71, 2000.
12. B. A. Pint and I. G. Wright, "Oxidation Behavior of ODS Fe-Cr Alloys," Oxidation of Metals, Vol. 63, Nos. 3/4, pgs. 193-213, 2005.
13. G. Baran, M. Meraner, and P. Farrell, "Transient Oxidation of Multiphase Ni-Cr Alloys," Oxidation of Metals, Vol. 29, Nos. 5/6, pgs. 409-429, 1988.
14. "International Workshop on High Temperature Corrosion," eds., D. L. Douglass, P. Kofstad, A. Rahmel, and G. C. Wood. Subject Area 8: Behavior of Scales Under Mechanical Loading. Chairman: M. Schütze, Secretary: J. R. Nicholls, Oxidation of Metals., Vol. 45, Nos. 5/6, pgs. 529-613, 1996.
15. G. Calvarin-Amiri, R. Molins, and A. M. Huntz, "Effect of the Application of a Mechanical Load on the Oxide-Layer Microstructure and on the Oxidation Mechanism of Ni-20Cr Foils," Oxidation of Metals, Vol. 54, Nos. 3/4, pgs. 399-426, 2000.
16. J. Stringer, B. A. Wilcox, and R. I. Jaffee, "The High-Temperature Oxidation of Nickel-20wt.% Chromium Alloys Containing Dispersed Oxide Phases," Oxidation of Metals, Vol. 5, No. 1, pgs. 11-47, 1972.
17. P. Pagliaro, M. B. Prime, B. Zuccarello, B. Clausen, and T. R. Watkins, "Validation Specimen for Contour Method Extension to Multiple Residual Stress Components,"

in Experimental Analysis of Nano and Engineering Materials and Structures: Proceedings of the 13th International Conference on Experimental Mechanics (ICEM13), Alexandroupolis, Greece, July 1-6, 2007, paper no. 246, CD-ROM. Edited by E. E. Gdoutos, Springer 2007.
18. S. J. Bull, "Modeling of Residual Stress in Oxide Scales," Oxidation of Metals, Vol. 49, Nos. 1/2, pgs. 1-17, 1998.
19. D. M. England and A. V. Virkar, "Oxidation Kinetics of Some Nickel-Based Superalloy Foils and Electronic Resistance of the Oxide Scale Formed in Air Part I," Journal of the Electrochemical Society, Vol. 146 (9), pgs. 3196-3202, 1999.
20. D. M. England and A. V. Virkar, "Oxidation Kinetics of Some Nickel-Based Superalloy Foils and Electronic Resistance of the Oxide Scale Formed in Air Part II," Journal of the Electrochemical Society, Vol. 148 (4), pgs. A330-A338, 2001.
21. D. E. Alman and P. D. Jablonski, "Low Coefficient of Thermal Expansion (CTE) Nickel Base Superalloys for Interconnect Applications in Intermediate Temperature Solid Oxide Fuel Cells (SOFC)," edited by TMS (The Minerals, Metals & Materials Society).
22. C. Mathieu and S. Toesca, "Effects of Mode-I Stresses on the Oxidation and Failure Mechanisms of Ni-20Cr and Ni-15Cr-8Fe Alloys in Sulfur Dioxide," Oxidation of Metals, Vol. 39, Nos. 3/4, pgs. 155-165, 1993.
23. N. Birks and G. H. Meier. Introduction to High Temperature Oxidation of Metals. Edward Arnold (Publishers) Ltd. London, England, 1983.
24. K. N. Strafford and J. M. Harrison, "Observations on the Oxidation Behavior of Ni-Cr Alloys Containing Minor Additions of Group III, IV, or V Elements," Oxidation of Metals, Vol. 10, No. 6, pgs. 347-359, 1976.
25. G. Calvarin-Amiri, R. Molins, and A. M. Huntz, "Oxidation Mechanism of Ni-20Cr Foils and Its Relation to the Oxide-Scale Microstructure," Oxidation of Metals, Vol. 53, Nos. 1/2, pgs. 25-48, 2000.
26. F. Rabbani, L. P. Ward, and K. N. Strafford, "A Comparison of the Growth Kinetics and Scale Morphology for Three Superalloys at 930°C in Air and Low $P_{O2}$ Environments," Oxidation of Metals, Vol. 54, Nos. 1/2, pgs. 139-153, 2000.
27. P. F. Tortorelli, "Mechanical Properties of Chromia Scales," Journal de Physique IV, Vol. 3, pgs. 943-949, 1993.
28. "International Workshop on 'Critical Issues Concerning the Mechanisms of High-Temperature Corrosion," eds. A. Rahmel, G. C. Wood, P. Kofstad, and D. L. Douglass. Subject Area 9: Interaction Between Oxidation (Sulfidation, Carburization) and Creep. Chairmen: B. Ilschner and M. Scütze, Oxidation of Metals, Vol. 23, Nos. 5/6, pgs. 251-292, 1985.
29. D. Poquillon and D. Monceau, "Application of a Simple Statistical Spalling Model for the Analysis of High-Temperature Cyclic-Oxidation Kinetics Data," Oxidation of Metals, Vol. 59, Nos. 3/4, pgs. 409-431, 2003.
30. H. E. Evans, "Stress Effects in High Temperature Oxidation of Metals," International Materials Reviews, Vol. 40, No. 1, pgs. 1-40, 1995.
31. H. Buscail, Y. P. Jacob, M. F. Stroosnijder, E. Caudron, R. Cueff, F. Rabaste, and S. Perrier, "X-ray Diffraction to Study the Oxidation Mechanism of Chromium at Elevated Temperatures," Materials Science Forum, Vols. 461-464, pgs. 93-100, 2004.

32. D. J. Srolovitz and T. A. Ramanarayanan, "An Elastic Analysis of Growth Stresses during Oxidation," Oxidation of Metals, Vol. 22, Nos. 3/4, pgs. 133-146, 1984.
33. A. M. Huntz, "Stresses in NiO, $Cr_2O_3$ and $Al_2O_3$ oxide scales," Materials Science and Engineering, Vol. A201, pgs. 211-228, 1994.
34. J. G. Goedjen, J. H. Stout, Q. Guo, and D. A. Shores, "Evaluation of Stresses in Ni-NiO and Cr-$Cr_2O_3$ during High Temperature Oxidation by *In Situ* X-ray Diffraction," Materials Science and Engineering, Vol. A177, pgs. 115-124, 1994.
35. D. Zhu, J. H. Stout, and D. A. Shores, "Determination of Stress Gradients in a Thermally Grown Oxide Layer Using X-Ray Diffraction," Materials Science Forum, Vols. 251-254, pgs. 333-340, 1997.
36. M. Kemdehoundja, J. F. Dinhut, J. L. Grosseau-Poussard, and M. Jeannin, "High Temperature Oxidation of $Ni_{70}Cr_{30}$ Alloy: Determination of Oxidation Kinetics and Stress Evolution in Chromia Layers by Raman Spectroscopy," Materials Science and Engineering A, Vols. 435-436, pgs. 666-671, 2006.
37. S. Daghigh, J. L. Lebrun, and A. M. Huntz, "Stresses in $Cr_2O_3$ Scales Developed on Ni-30Cr," Materials Science Forum, Vols. 251-254, pgs. 381-388, 1997.
38. A. M. Huntz, S. Daghigh, A. Piant, and J. L. Lebrun, "Evidence of Stress Relaxation in Thermally Grown Oxide Layers – Experiments and Modelling," Materials Science and Engineering Vol. A248, pgs. 44-55, 1998.
39. M. Khadhraoui, W. Cao, L. Castex, and J. Y. Guedo, "Experimental Investigations and Modelling of Relaxation Behaviour of Shot Peening Residual Stresses at High Temperature for Nickel Base Superalloys," Materials Science and Technology, Vol. 13, pgs. 360-367, 1997.
40. W. Cao, M. Khadhraoui, B. Brenier, J. Y. Guedo, and L. Castex, "Thermomechanical Relaxation of Residual Stress in Shot Peened Nickel Base Superalloy," Materials Science and Technology, Vol. 13, pgs. 360-367, 1997.
41. O. Kubaschewski and B. E. Hopkins. Oxidation of Metals and Alloys. 2nd edition. Butterworth and Co. Ltd., London, England, 1962.
42. N. Hussain, K. A. Shalid, I. H. Khan, and S. Rahman, "Oxidation of High-Temperature Alloys (Superalloys) at Elevated Temperatures in Air. II," Oxidation of Metals, Vol. 43, Nos. 3/4, pgs. 363-378, 1995.
43. C. L. Angerman, "Long-Term Oxidation of Superalloys," Oxidation of Metals, Vol. 5, No. 2, pgs. 149-167, 1972.
44. www.mse.arizona.edu/classes/mse435/oxidation.pdf.
45. B. Pieraggi. "Calculations of Parabolic Reaction Rate Constants," Oxidation of Metals, Vol. 27, Nos. 3/4, pgs. 177-185, 1987.
46. J. M. West. Basic Corrosion and Oxidation. Ellis Horwood Limited, Market Cross House, Cooper Street, Chichester, West Sussex, PO19 1EB, England, 1980.
47. P. Huczkowski, N. Christiansen, V. Shemet, J. Piron-Abellan, L. Singheiser, and W. J. Quadakkers, "Oxidation Limited Life Times of Chromia Forming Ferritic Steels," Materials and Corrosion, Vol. 55, No. 11, pgs. 825-830, 2004.
48. H. Krause and A. Haase, "X-Ray Diffraction System PTS for Powder, Texture and Stress Analysis," Experimental Techniques of Texture Analysis, DGM Informationsgesellschaft•Verlag, Oberursel, ed., H. J. Bunge, pgs. 405-408, 1986.

49. I. C. Noyan and J. B. Cohen, Residual Stress, Measurement by Diffraction and Interpretation, Springer-Verlag, New York, 1987.
50. T. R. Watkins, O. B. Cavin, J. Bai, and J. A. Chediak, "Residual Stress Determinations Using Parallel Beam Optics," Advances in X-Ray Analysis, Vol. 46 CD ROM, eds., T. C. Huang et al., ICDD, Newtown Square, PA, pgs. 119-129, 2003.
51. P. Rudnik and J. B. Cohen, "Errors Due To Counting Statistics in the Triaxial Strain (Stress) Tensor Determined by Diffraction," Advances in X-Ray Analysis, eds., J. B. Cohen et al., Plenum Press, NY, Vol. 29, pgs. 79-88, 1985.
52. M. Schütze, "Mechanical Properties of Oxide Scales," Oxidation of Metals, Vol. 44, Nos. 1/2, pgs. 29-61, 1995.
53. M. Schütze, "Deformation and Cracking Behavior of Protective Oxide Scales on Heat-Resistant Steels under Tensile Strain," Oxidation of Metals, Vol. 24, Nos. 3/4, pgs. 199-232, 1985.
54. F. R. N. Nabarro and H. L. de Villiers, The Physics of Creep and Creep-Resistant Alloys, Taylor and Francis Publishers, London, England, 1995.
55. A. V. Virkar, J. L. Huang, and R. A. Cutler, "Strengthening of Oxide Ceramics by Transformation-Induced Stresses," Journal of the American Ceramic Society, Vol. 70, No. 3, pgs. 164-170, 1987.
56. B. D. Cullity, Elements of X-RAY DIFFRACTION, Second Edition, Addison-Wesley Publishing Company, Inc., Reading Massachusetts, 1978.
57. S.-B. Kim, A. Evans, J. Shackleton, G. Bruno, M. Preuss, and P. J. Withers, "Stress Relaxation of Shot-Peened UDIMET 720Li under Solely Elevated-Temperature Exposure and under Isothermal Fatigue," Metallurgical and Materials Transactions A, Vol. 36A, pgs. 3041-3053, 2005.
58. E. A. Brandes, ed., Smithells Metals Reference Book, Sixth Edition, Butterworth and Co. Ltd., London, England, 1983.
59. G. E. Dieter, Mechanical Metallurgy, Third Edition, McGraw Hill, Boston Massachusetts, 1986.

# Appendices

## Appendix A (Tables)

Table 1: Actual chemical compositions of 75 and 230 alloys in weight percent.

| Element | 75 Alloy (Independent) | 75 Alloy (HAYNES®) | 230 Alloy (Independent) | 230 Alloy (HAYNES®) |
|---|---|---|---|---|
| **Ni** | 73.75 | 73.92* | 59.88 | 59.84* |
| **Cr** | 20.19 | 19.94 | 22.55 | 22.05 |
| **W** | 0.05 | <0.10 | 13.64 | 14.01 |
| **Fe** | 3.63 | 3.76 | 1.01 | 1.28 |
| **Mo** | 0.58 | 0.59 | 1.33 | 1.30 |
| **Si** | 0.49 | 0.50 | 0.39 | 0.41 |
| **Mn** | 0.32 | 0.32 | 0.52 | 0.48 |
| **Al** | 0.26 | 0.25 | 0.36 | 0.35 |
| **Ti** | 0.41 | 0.43 | 0.01 | <0.01 |
| **Co** | 0.12 | 0.13 | 0.10 | 0.12 |
| **C** | 0.11 | 0.11 | 0.092 | 0.10 |
| **Nb** | 0.03 | <0.050 | 0.03 | Not given |
| **V** | 0.01 | Not given | 0.04 | Not given |
| **Cu** | 0.01 | 0.04 | 0.01 | 0.04 |
| **Mg** | 0.01 | 0.005 | <0.01 | Not given |
| **Ce** | <0.01 | Not given | <0.01 | Not given |
| **La** | <0.01 | Not given | <0.01 | 0.016 |
| **Pb** | Not given | <0.0005 | Not given | Not given |
| **Ta** | <0.01 | <0.100 | <0.01 | Not given |
| **Zr** | <0.01 | <0.010 | <0.01 | Not given |
| **B** | 0.002 | 0.004 | 0.002 | 0.004 |
| **P** | <0.002 | <0.005 | <0.002 | <0.005 |
| **Y** | <0.0003 | Not given | <0.0003 | Not given |
| **N** | 143 ppm | Not given | 289 ppm | Not given |
| **O** | 24 ppm | Not given | 18 ppm | Not given |
| **S** | <10 ppm | 0.004 | <10 ppm | <0.002 |

*Weight percentages of nickel were originally given as "balance." Elements with unknown weight-percent values (preceded by < signs) were omitted in the calculation of the weight percentages of nickel.

Table 2: Experimental conditions of the x-ray measurements.

| Parameter | Condition |
|---|---|
| Equipment | MAC Science 18 kW rotating-anode generator<br>Osmic CMF multilayer mirror<br>Scintag PTS goniometer<br>Scintag liquid $N_2$-cooled Ge detector |
| Power | 8 kW; 40 kV, 200 mA |
| Radiation | Cu, $\lambda$ = 1.54059 Å |
| Incidence slit width | 0.5 mm |
| Receiving slit acceptance | 0.25°; radial divergence limiting (RDL) Soller slit |
| Source to specimen distance | 360 mm |
| Specimen to back slit distance | 280 mm |
| Tilt axis and angles (oxides) | $\Omega$; 0, ± 28.2, ± 42, ± 55 ° (equal steps of $\sin^2\Psi$) |
| Tilt axis and angles (75 as-received, stressed (13.5 MPa) / isothemal, unstressed / cycled) | $\Omega$; 0, ± 13.1, ± 18.7, ± 23.2, ± 27, ± 30.5, ± 33.8, ± 36.9, ± 40, ± 43, ± 45.9, ± 48.9, ± 51.9, ± 55, ° (equal steps of $\sin^2\Psi$) |
| Tilt axis and angles (75 stressed (6.7 MPa) / cycled, stressed (6.7 MPa) / isothermal) | $\Omega$; 0, ± 18, ± 26, ± 32.4, ± 38.3, ± 43.8, ± 49.3, ± 55, ° s (equal steps of $\sin^2\Psi$) |
| Tilt axis and angles (230 alloy) | $\Omega$; 0, ± 18, ± 26, ± 32.4, ± 38.3, ± 43.8, ± 49.3, ± 55, ° (equal steps of $\sin^2\Psi$) |
| Scans (oxide) | 0.02 °2$\Theta$/step; 0.20 °2$\Theta$/minute |
| Scans (alloy) | 0.02 °2$\Theta$/step; 16 s/step |

Table 3: Comparison of mass gain, parabolic-oxidation-rate constant ($k_p$), thickness, and internal-oxidation data for unstressed and stressed specimens.

| Alloy | Cond. | Stress (MPa) | Temp. (°C) | Total Specific Mass Gain (mg / $cm^2$) | $k_p$ [$g^2$ / ($cm^4$ × sec)] | Thickness (μm)* | Max. Int. Oxid. Depth (μm) | Avg. Int. Oxid. Depth (μm) |
|---|---|---|---|---|---|---|---|---|
| 230 | Cyc. | 0 | 700 | 0.03 | 1.8E-16 | N.A. | N.A. | N.A. |
| 75 | Cyc. | 0 | 700 | 0.02 | 2.3E-16 | 0.6 ± 0.2 | 1.5 | 1.2 |
| 230 | Cyc. | 0 | 700 | 0.012 | 2.8E-16 | 0.2 ± 0.1 | 1.25 | 1.1 |
| 75 | Iso. | 37.7 | 700 | 0.03 | 2.8E-16 | 1.0 ± 0.3 | 1.5 | 1.3 |
| 75 | Cyc. | 0 | 700 | 0.06 | 7.1E-16 | N.A. | N.A. | N.A. |
| 230 | Iso. | 0 | 700 | 0.06 | 1.0E-15 | N.A. | N.A. | N.A. |
| 230 | Iso. | 0 | 700 | 0.07 | 1.2E-15 | 0.7 ± 0.2 | 2.4 | 1.5 |
| 75 | Iso. | 0 | 700 | 0.08 | 1.7E-15 | N.A. | N.A. | N.A. |
| 75 | Iso. | 0 | 700 | 0.09 | 2.0E-15 | 1.0 ± 0.4 | 2.8 | 2.0 |
| 230 | Iso. | 72.5 | 800 | 0.11 | 3.6E-15 | 2.1 ± 0.6 | 4.5 | 3.0 |
| 230 | Cyc. | 72.5 | 800 | 0.10 | 4.4E-15 | 1.6 ± 0.3 | 11.0 | 5.9 |
| 75 | Iso. | 6.7 | 800 | 0.19 | 1.0E-14 | 2.9 ± 0.5 | 7.0 | 4.3 |
| 75 | Iso. | 13.5 | 800 | 0.20 | 1.1E-14 | 2.8 ± 0.6 | 10.5 | 4.6 |
| 75 | Cyc. | 6.7 | 800 | 0.19 | 1.1E-14 | 3.0 ± 0.9 | 6.0 | 4.0 |
| 230 | Iso. | 0 | 800 | 0.26 | 1.8E-14 | N.A. | N.A. | N.A. |
| 230 | Iso. | 0 | 800 | 0.26 | 1.8E-14 | 2.1 ± 0.8 | 17.2 | 2.9 |
| 230 | Cyc. | 0 | 800 | 0.25 | 1.8E-14 | 2.4 ± 0.9 | 9.5 | 4.1 |
| 230 | Cyc. | 0 | 800 | 0.25 | 1.9E-14 | N.A. | N.A. | N.A. |
| 75 | Cyc. | 0 | 800 | 0.45 | 6.3E-14 | N.A. | N.A. | N.A. |
| 75 | Iso. | 0 | 800 | 0.48 | 6.3E-14 | 3.7 ± 0.7 | 10.7 | 5.8 |
| 75 | Cyc. | 0 | 800 | 0.51 | 7.0E-14 | 4.3 ± 1.1 | 7.5 | 4.4 |
| 75 | Iso. | 0 | 800 | 0.57 | 8.9E-14 | N.A. | N.A. | N.A. |
| 230 | Iso. | 133 | 700 | N.A.** | N.A.** | 0.7 ± 0.2 | 1.5 | 1.1 |

* ± Standard Deviation, Oxide-thickness values were obtained by taking the average of over twenty measurements across each oxide scale.

** For the 230-alloy specimen oxidized under an applied stress of 133 MPa at 700°C, an unreliable value for specific mass change was observed due to the fact that its pre-oxidation mass had been recorded immediately after it had been cleaned with acetone, which caused the mass to be unusually high. Thus, this specimen's specific mass change data point was considered untrustworthy and removed.

Table 4: Calculated residual-stress values for oxides and substrates of the 75 and 230 alloys oxidized under various conditions at 800˚C.

| **Alloy** | **Oxidizing Condition** | **Applied Stress (MPa)** | **Residual Stress 416 peak (GPa) Oxide** | **Residual Stress 331 peak (MPa) Substrate** | **Residual Stress 420 peak (MPa) Substrate** | **Average Residual Stress (MPa) Substrate** |
|---|---|---|---|---|---|---|
| 230 | isothermal | 72.5 | -1.6 | -89 ± 18** | -63 | -76 |
| 230 | cyclic | 72.5 | -1.7 | -4.5 ± 16 *** | -54 | -29 |
| 75 | isothermal | 6.7 | -1.8 | -77 | -20 | -49 |
| 75 | isothermal | 13.5 | -1.4 | -44 | -27 | -36 |
| 75 | cyclic | 6.7 | -1.6 | -55 | -36 | -46 |
| 230 | isothermal | 0 | -1.2 | -17 | -23 | -20 |
| 230 | cyclic | 0 | -1.6 | -37 | -25 | -31 |
| 75 | cyclic | 0 | -1.5 | -85 | -30 ± 14* | -58 |
| 75 | isothermal | 0 | -1.6 | - | - | - |
| 75 | as-received | 0 | - | -60 | -51 ± 4* | -56 |
| 230 | as-received | 0 | - | -100 | -170 | -140 |

*average of four sets of residual-stress measurements
[-13, -44, -26, -37 MPa for the 75-alloy specimen oxidized cyclically under no stress]
[-45, -54, -51, -53 MPa for the as-received 75-alloy specimen]

**average of five sets of residual-stress measurements
[-113, -86, -69, -101, -75 MPa]

***average of six sets of residual-stress measurements
[-13, -18, 7, 8, 13, -24 MPa]

Table 5: Nominal-composition information for additional alloys used in other studies for comparison purposes.

| Element | Astroloy | Hastelloy X | Udimet 720 | Waspaloy |
|---|---|---|---|---|
| **Ni** | 55.41** | 47[a] | 55.155** | 58.4835** |
| **Cr** | 15.0 | 22 | 18.0 | 19.5 |
| **Co** | 17.0 | 1.5 | 15.0 | 13.5 |
| **Mo** | 5.0 | 9 | 3.0 | 4.0 |
| **Ti** | 3.5 | - | 5.0 | 3.0 |
| **Al** | 4.0 | - | 2.5 | 1.4 |
| **C** | 0.06 | 0.10 | 0.02 | 0.06 |
| **B** | 0.03 | 0.008* | 0.035 | 0.0065 |
| **Zr** | - | - | 0.04 | 0.05 |
| **W** | - | 0.6 | 1.25 | - |
| **Fe** | - | 18 | - | - |
| **Mn** | - | 1* | - | - |
| **Si** | - | 1* | - | - |

[a]As balance
*Maximum
**Calculated

Table 6: Mechanical-mechanism-determination data.

| **Temp. (°C)** | **Alloy** | **Applied Stress, σ (MPa)** | **E (GPa)** | **υ** | **G (GPa)** | **σ / G** | **Mechanism** |
|---|---|---|---|---|---|---|---|
| 700 | 75 | 37.7 | 173 | 0.3* | 66.5 | $5.7 \times 10^{-4}$ | Dislocation creep |
| 700 | 230 | 133 | 171 | 0.339** | 63.9 | $2.1 \times 10^{-3}$ | Dislocation creep |
| 800 | 75 | 6.7 | 165 | 0.3* | 63.5 | $1.1 \times 10^{-4}$ | Dislocation creep |
| 800 | 75 | 13.5 | 165 | 0.3* | 63.5 | $2.1 \times 10^{-4}$ | Dislocation creep |
| 800 | 230 | 72.5 | 164 | 0.344** | 61.0 | $1.2 \times 10^{-3}$ | Dislocation creep |

*assumed value

**interpolated from manufacturer data

## Appendix B (Figures)

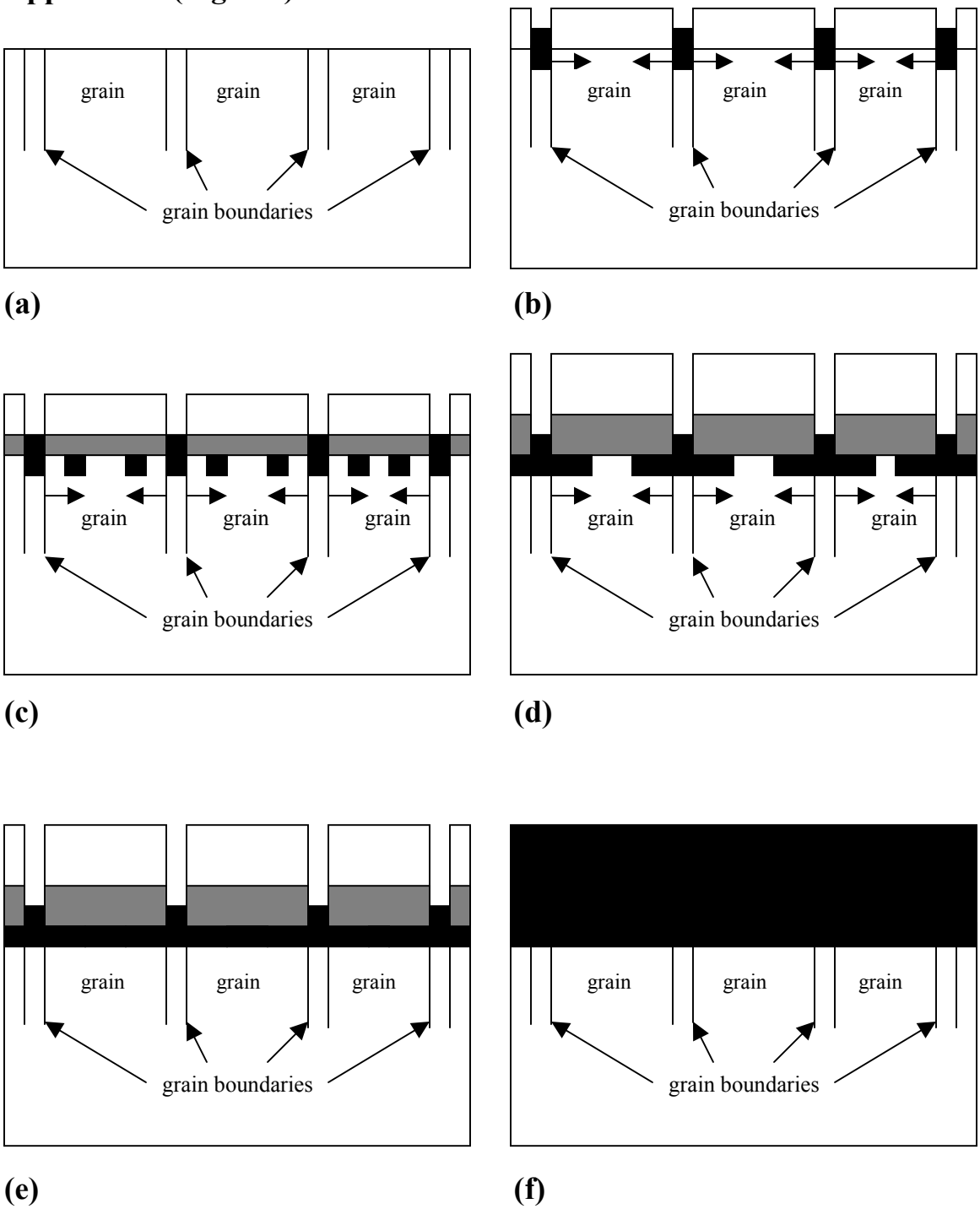


Figure 1: Schematic diagram of the oxidation process in Ni-Cr alloys showing the pre-oxidized substrate (a), the formation and growth of NiO (white layer), $NiCr_2O_4$ (gray layer), and growth of $Cr_2O_3$ (black layer) by lateral diffusion (b) to (e), as well as the eventual supplanting of the nickel-containing oxides by the protective chromia layer after appreciable oxidation times (f).

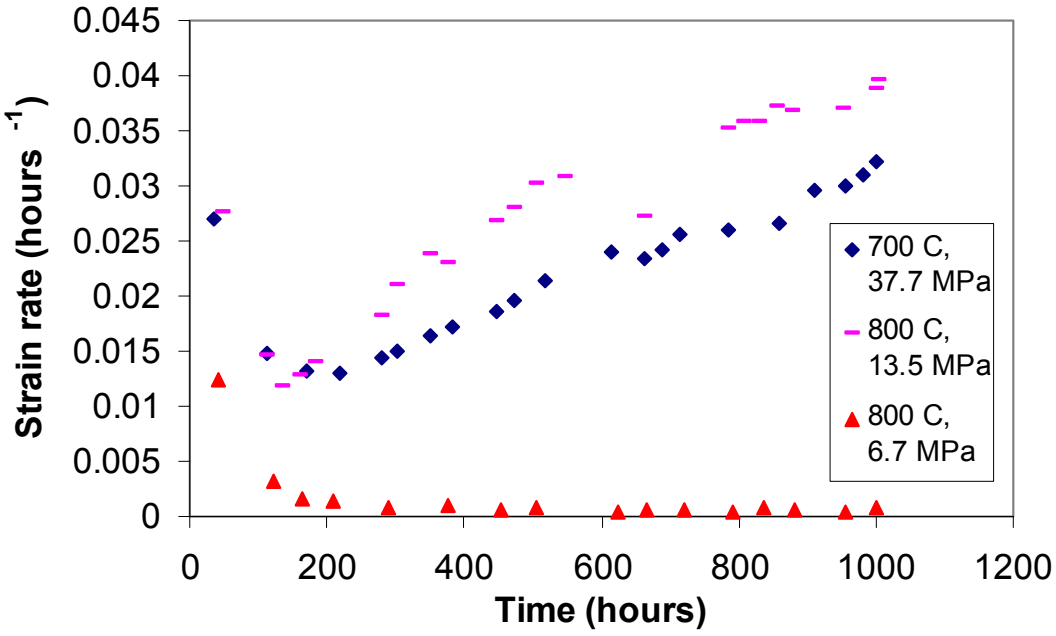


(a)

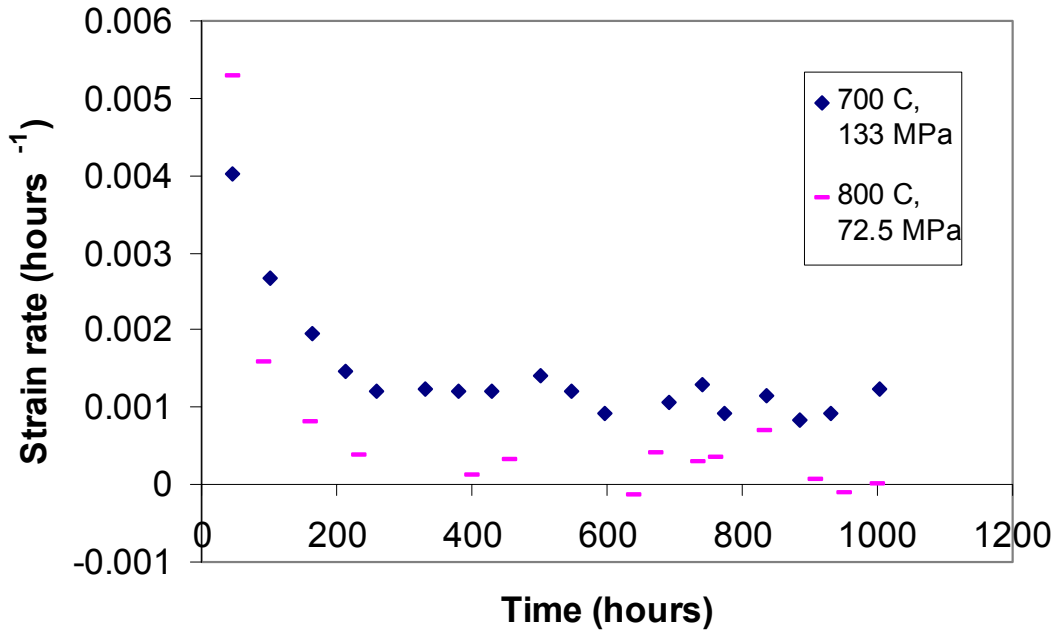


(b)

Figure 2: (a) Creep-strain rate versus time of 75-alloy specimens after 1,000 hours, (b) Creep-strain rate versus time of 230-alloy specimens after 1,000 hours.

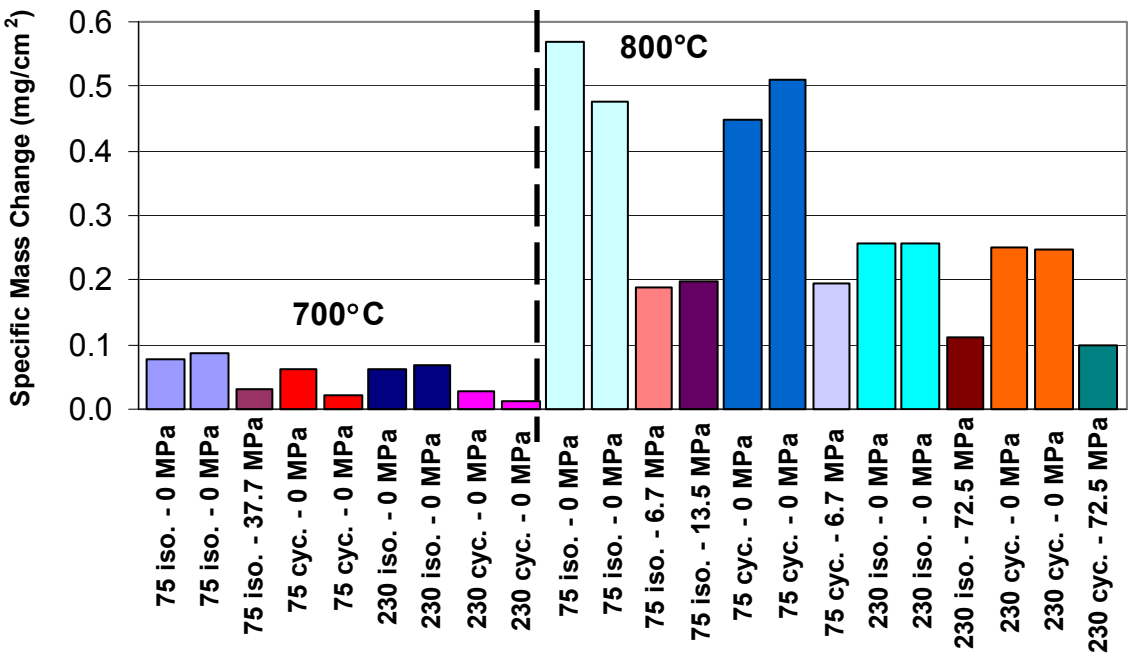


Figure 3: Bar graph of specific mass change data.

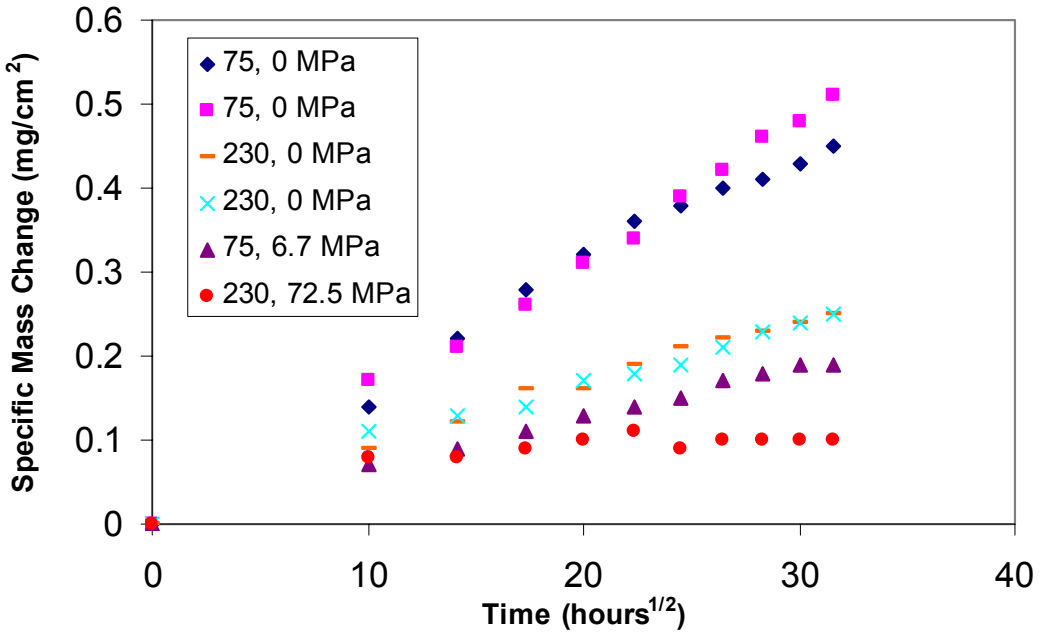


Figure 4: Cyclic-oxidation data for 75- and 230-alloy specimens undergoing ten 100-hour cycles at 800°C in the stressed and unstressed conditions.

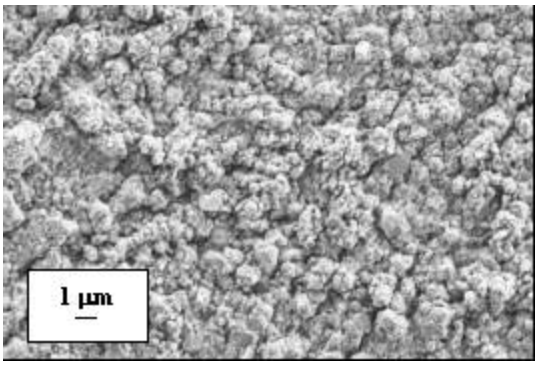


(a)

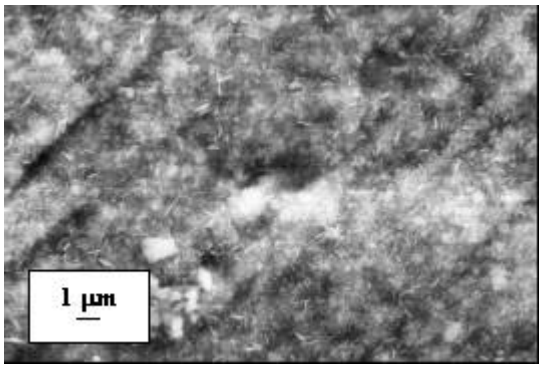


(b)

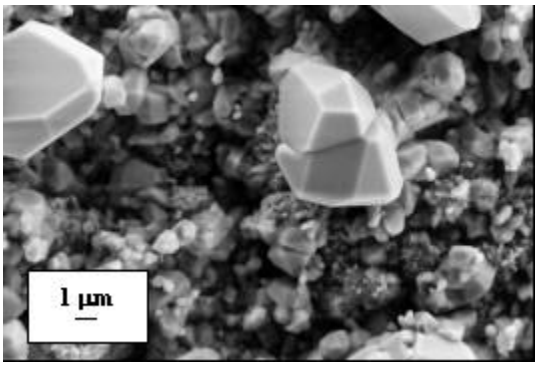


(c)

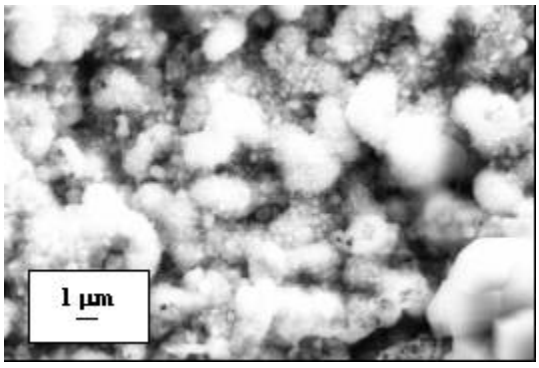


(d)

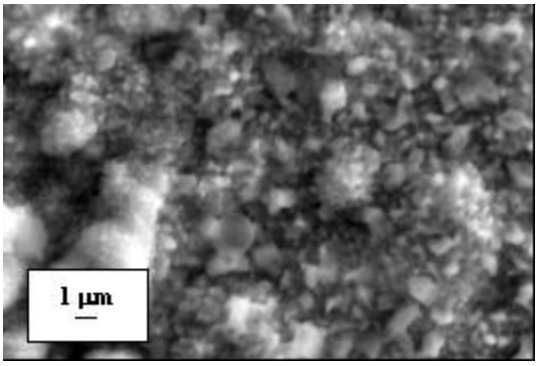


(e)

Figure 5: SEM image of the plane view of a 75-alloy specimen oxidized isothermally for 1,000 hours at: (a) 700°C, (b) 700°C under an applied stress of 37.7 MPa, (c) 800°C, (d) 800°C under an applied stress of 13.5 MPa, and (e) 800°C under an applied stress of 6.7 MPa.

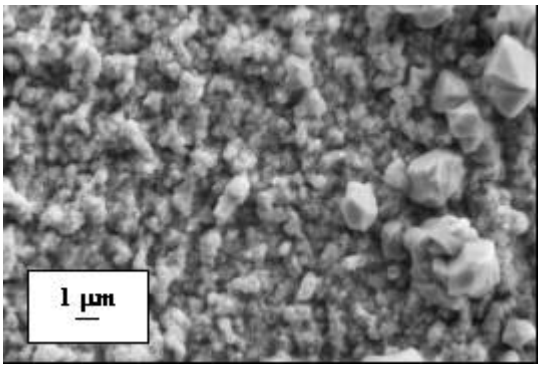


(a)

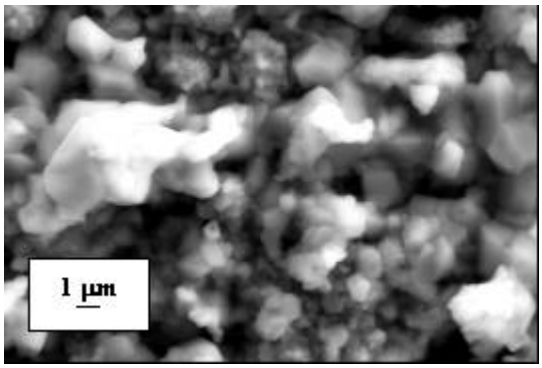


(b)

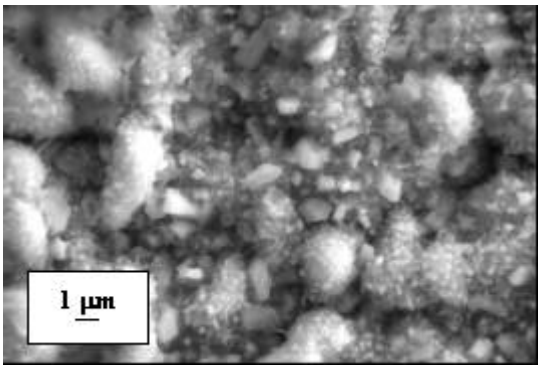


(c)

Figure 6: SEM image of the plane view of a 75-alloy specimen oxidized cyclically for ten 100-hour cycles at: (a) 700°C, (b) 800°C, and (c) 800°C under an applied stress of 6.7 MPa.

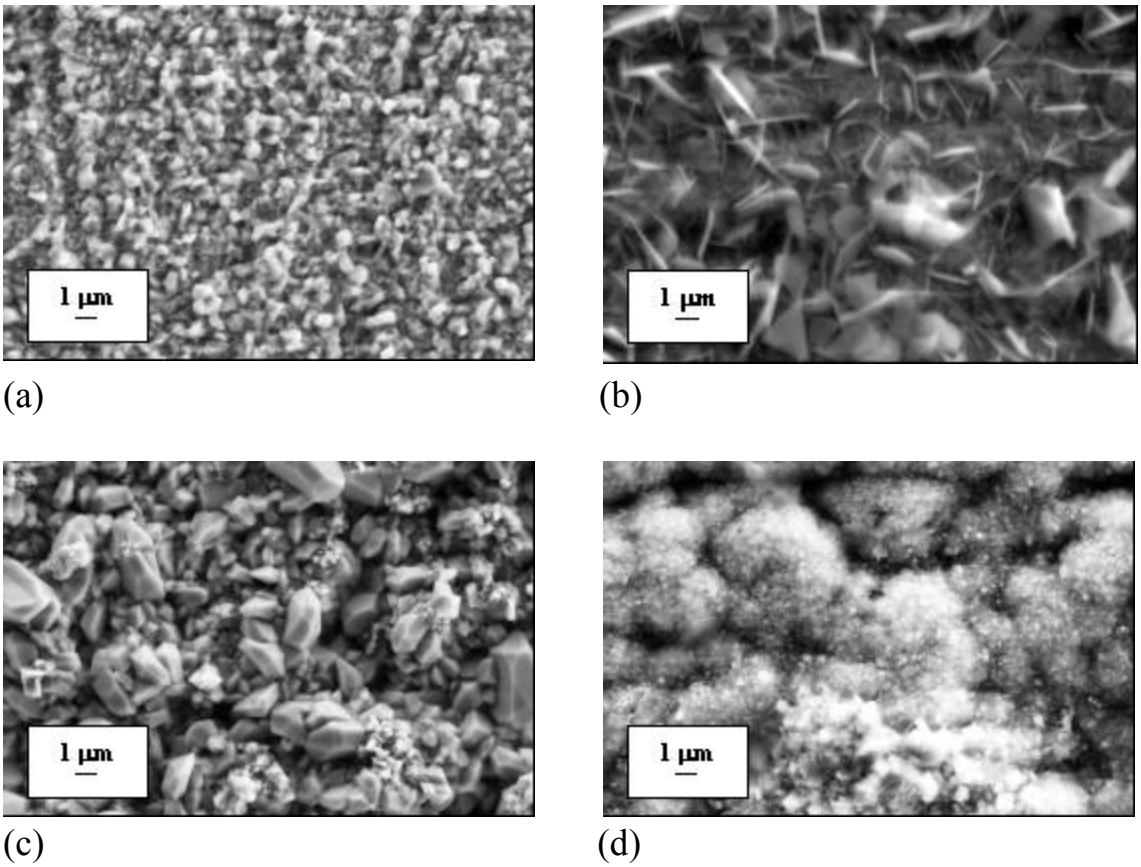


Figure 7: SEM image of the plane view of a 230-alloy specimen oxidized isothermally for 1,000 hours at: (a) 700°C, (b) 700°C under an applied stress of 133 MPa, (c) 800°C, and (d) 800°C under an applied stress of 72.5 MPa.

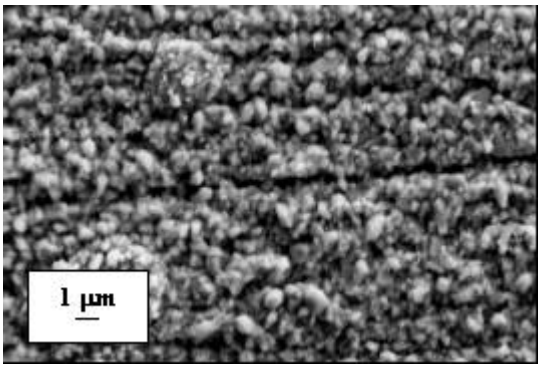


(a)

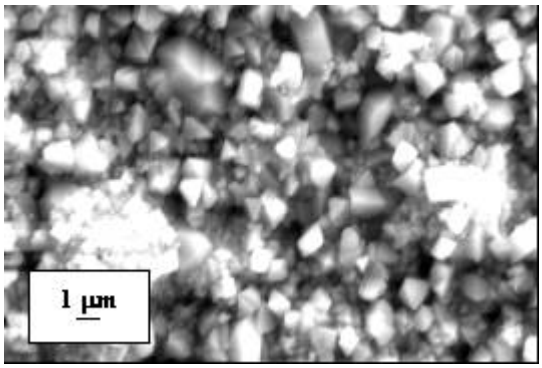


(b)

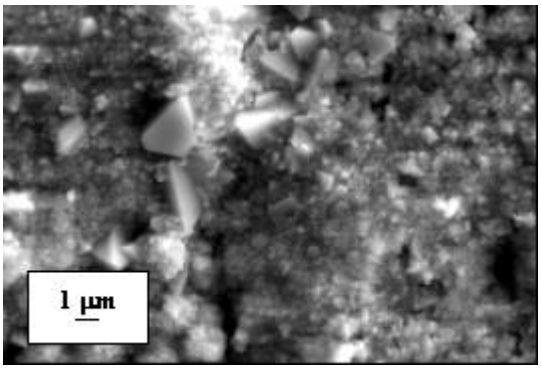


(c)

Figure 8: SEM image of the plane view of a 230-alloy specimen oxidized cyclically for ten 100-hour cycles at: (a) 700°C, (b) 800°C, and (c) 800°C under an applied stress of 72.5 MPa.

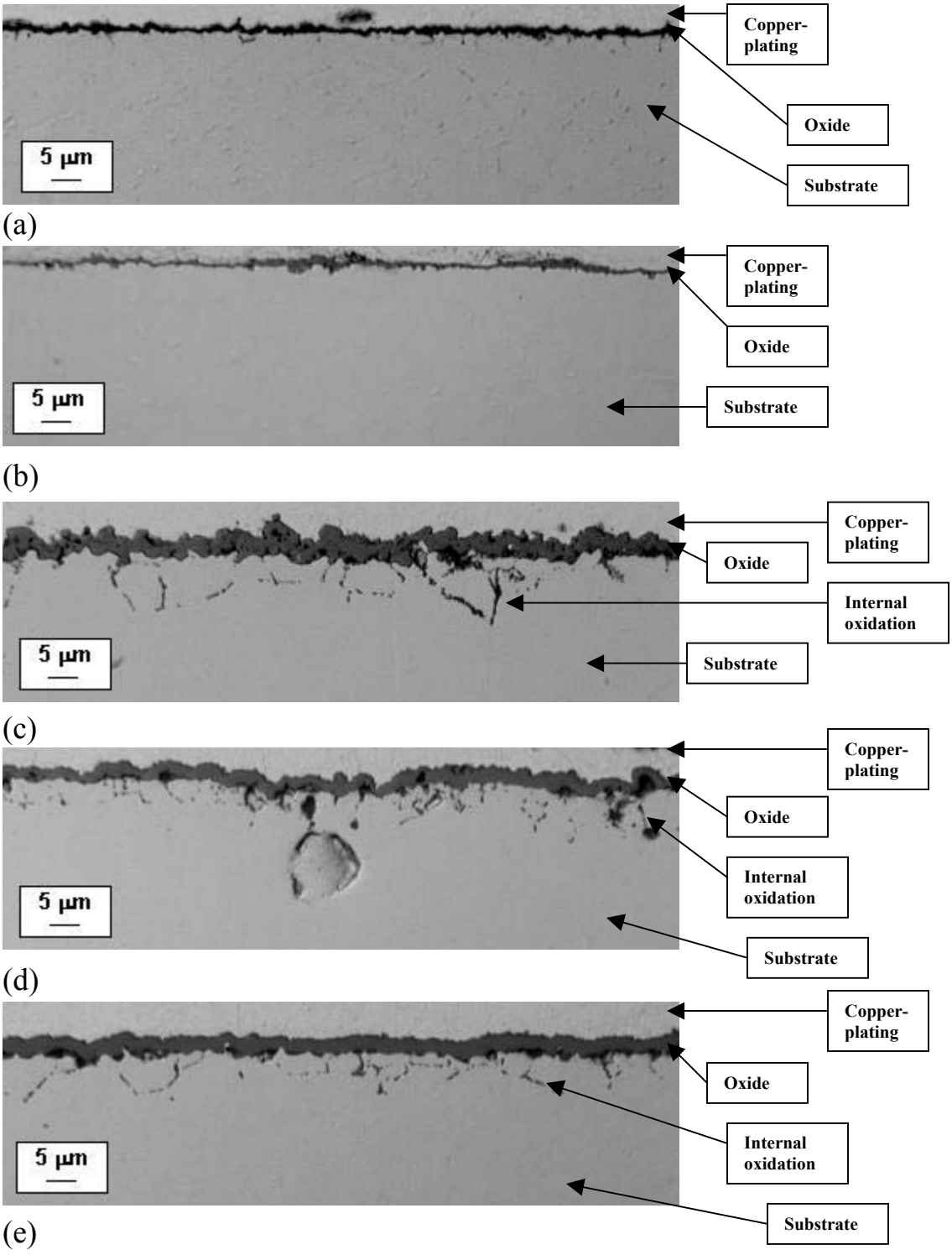


Figure 9: Light-microscopy image of the cross-section of a 75-alloy specimen oxidized isothermally for 1,000 hours at: (a) 700°C, (b) 700°C under an applied stress of 37.7 MPa, (c) 800°C, (d) 800°C under an applied stress of 13.5 MPa, and (e) 800°C under an applied stress of 6.7 MPa.

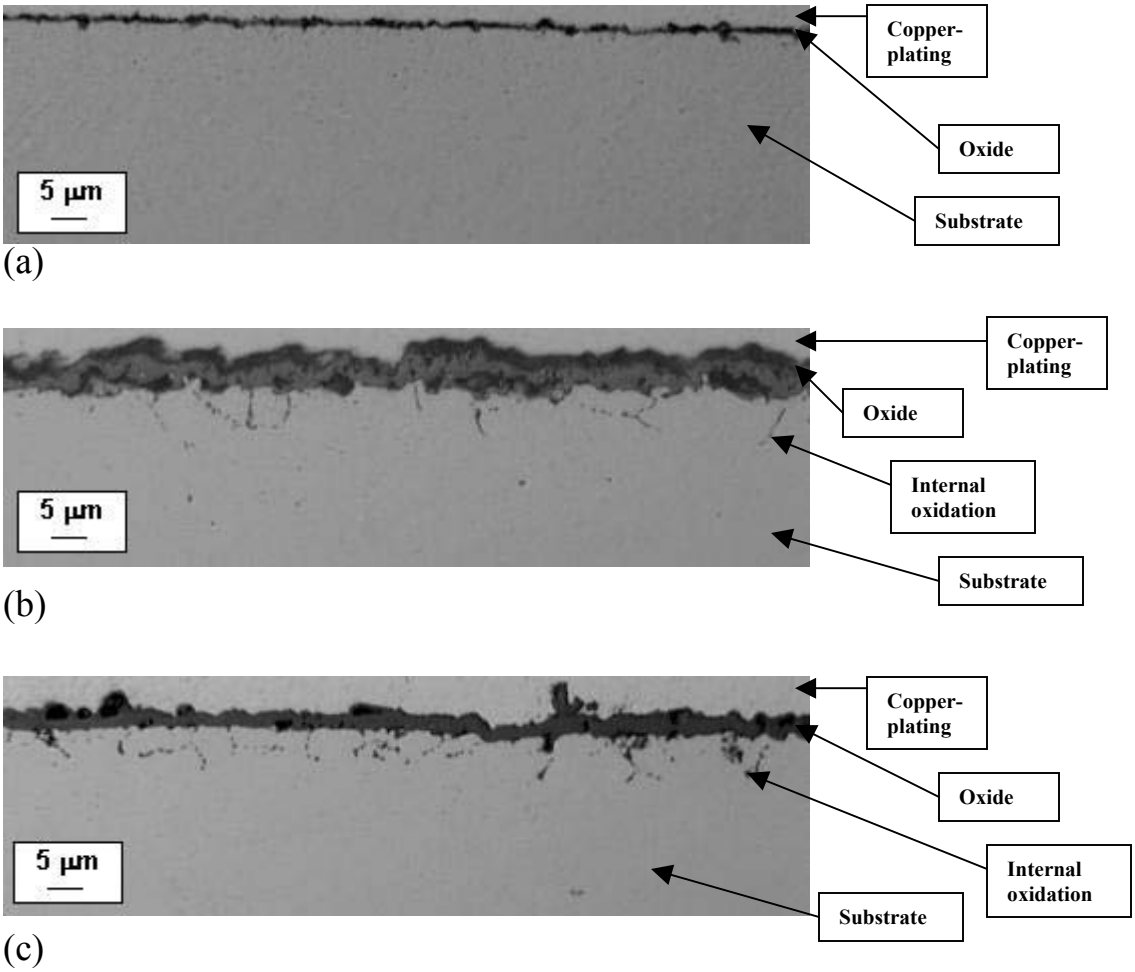


Figure 10: Light-microscopy image of the cross-section of a 75-alloy specimen oxidized cyclically for ten 100-hour cycles at: (a) 700°C, (b) 800°C, and (c) 800°C under an applied stress of 6.7 MPa.

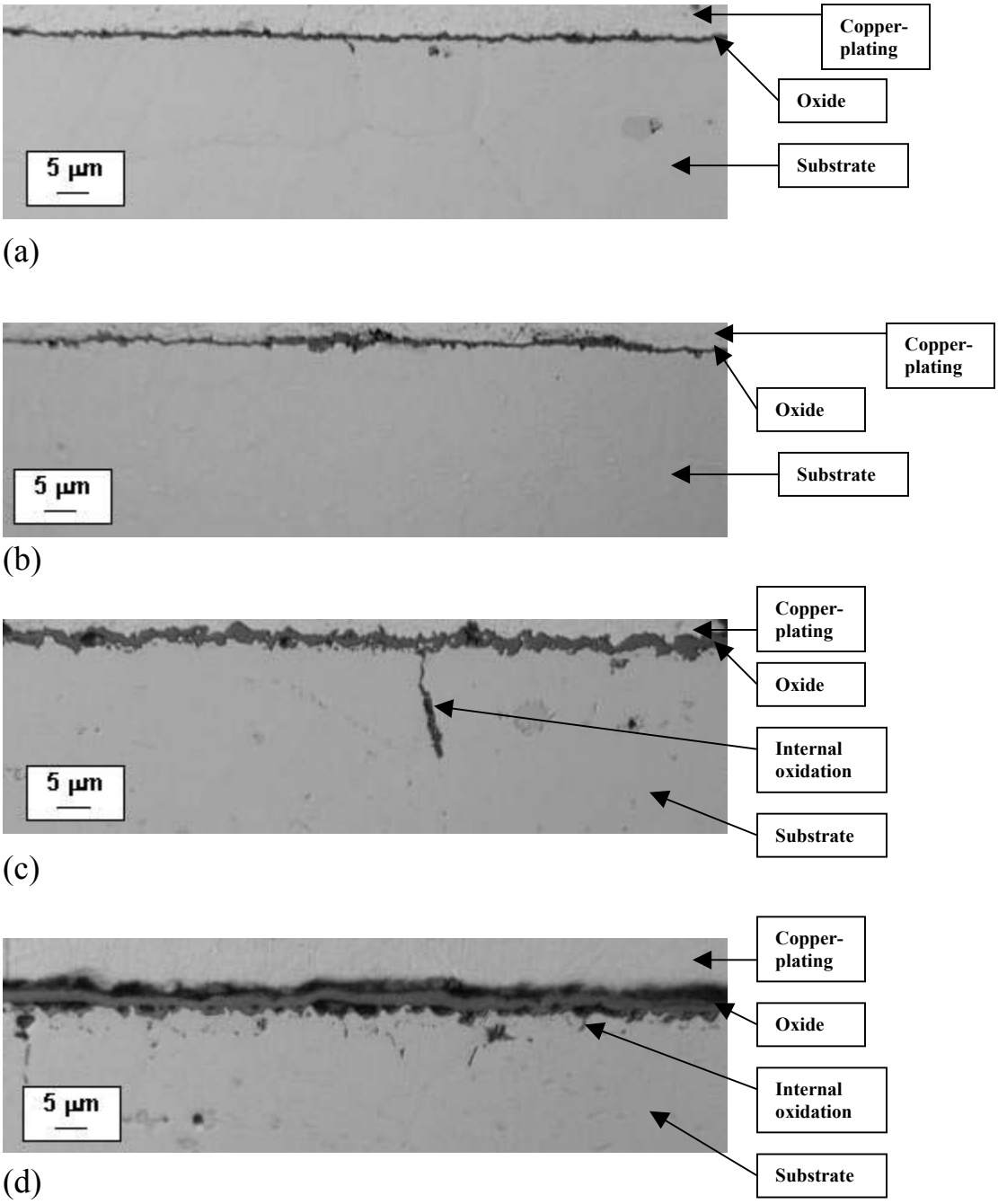


Figure 11: Light-microscopy image of the cross-section of a 230-alloy specimen oxidized isothermally for 1,000 hours at: (a) 700°C, (b) 700°C under an applied stress of 133 MPa, (c) 800°C, and (d) 800°C under an applied stress of 72.5 MPa.

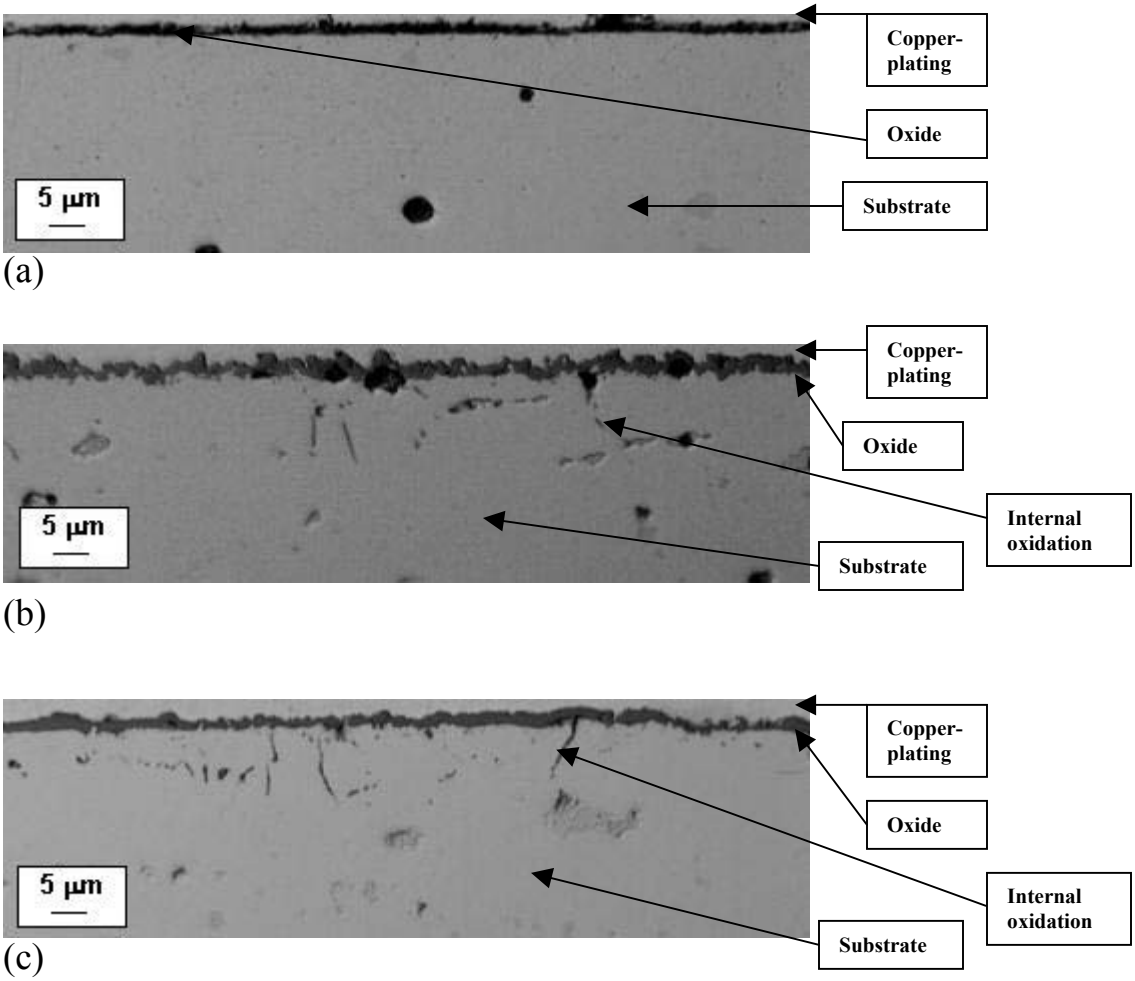


Figure 12: Light-microscopy image of the cross-section of a 230-alloy specimen oxidized cyclically for ten 100-hour cycles at: (a) 700°C, (b) 800°C, and (c) 800°C under an applied stress of 72.5 MPa.

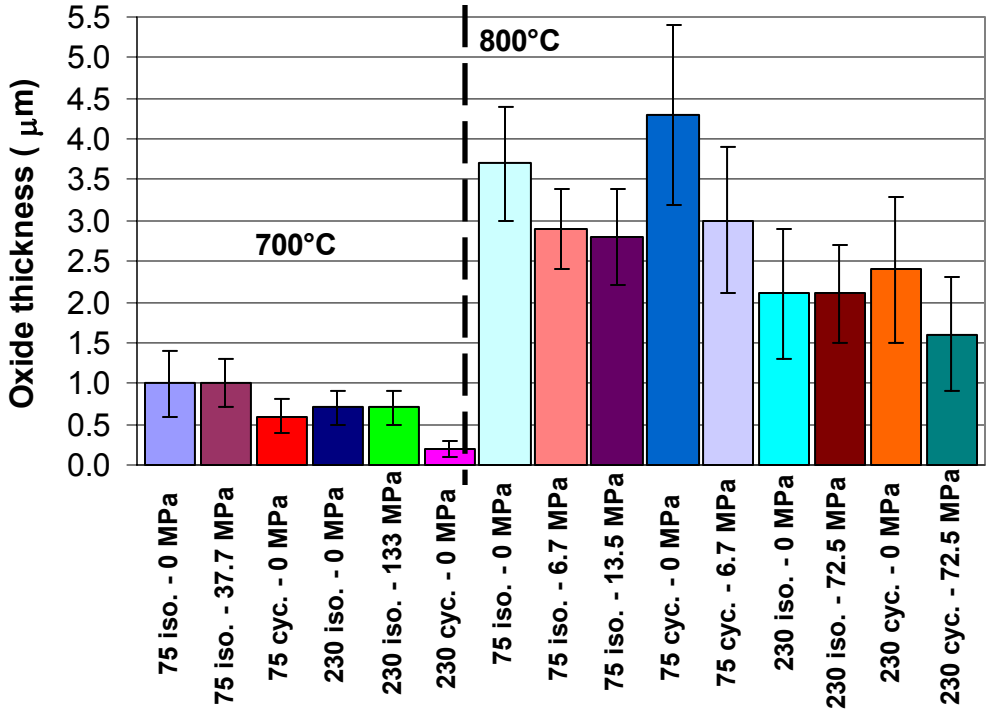


Figure 13: Bar graph of oxide-thickness data.

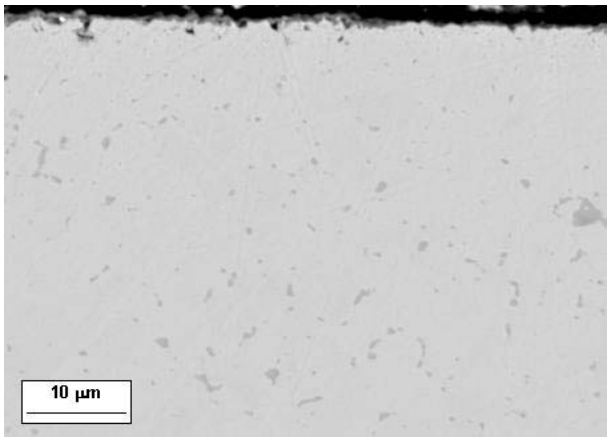


**(a)**

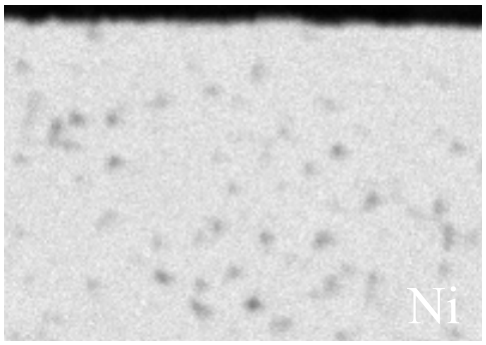


**(b)**

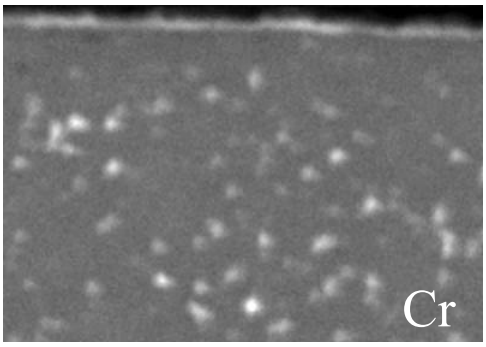


**(c)**

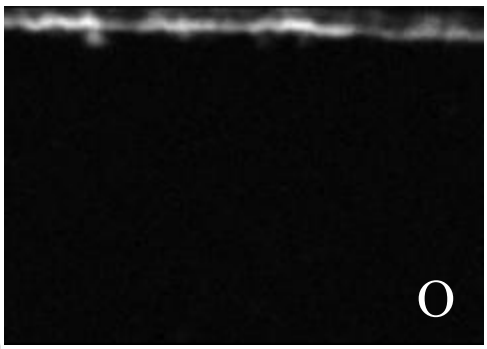


**(d)**

Figure 14: EPMA element maps of a 75-alloy specimen isothermally oxidized at 700°C – (a) Backscattered Image, (b) Ni, (c) Cr, and (d) O.

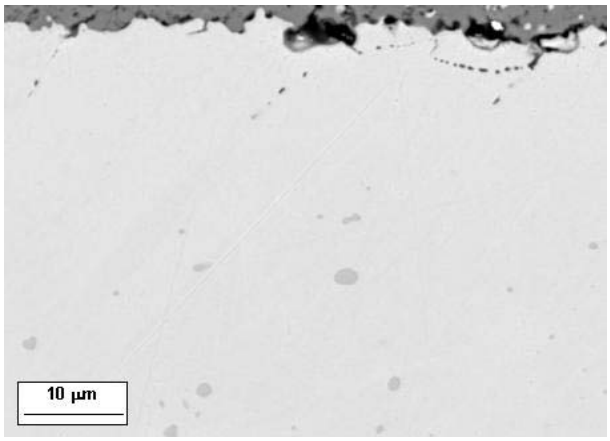


**(a)**

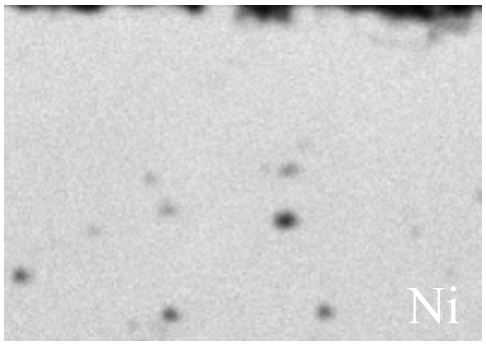


**(b)**

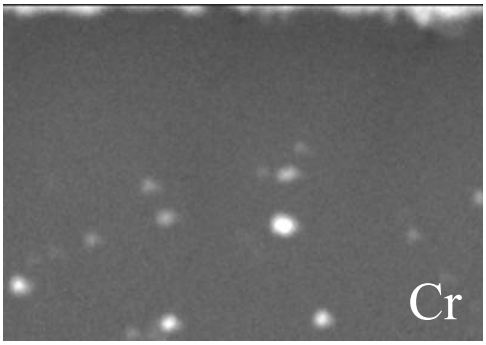


**(c)**

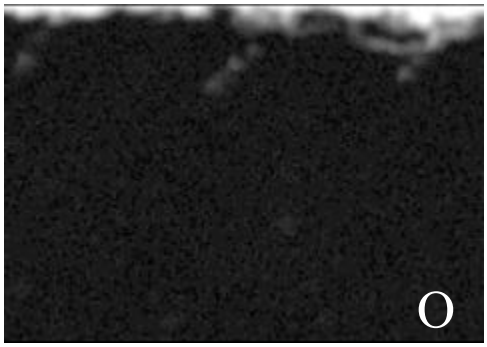


**(d)**

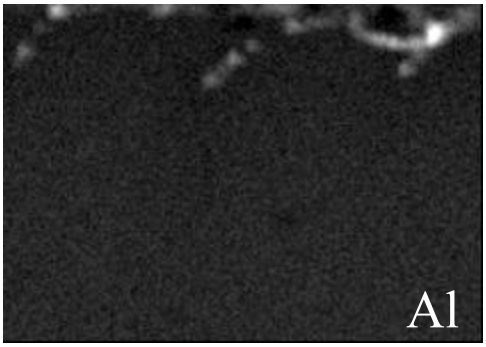


**(e)**

Figure 15: EPMA element maps of a 75-alloy specimen isothermally oxidized at 800°C – (a) Backscattered Image, (b) Ni, (c) Cr, (d) O, and (e) Al.

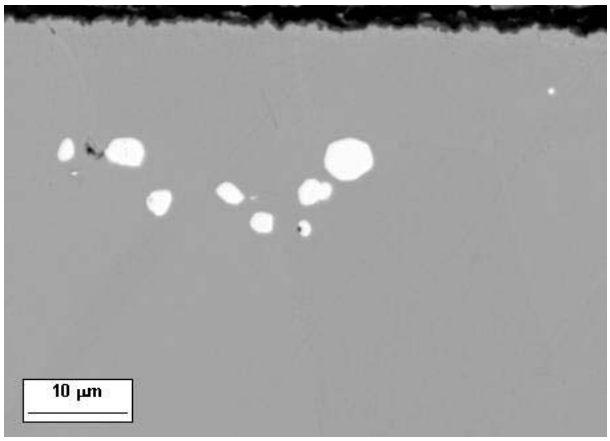


**(a)**

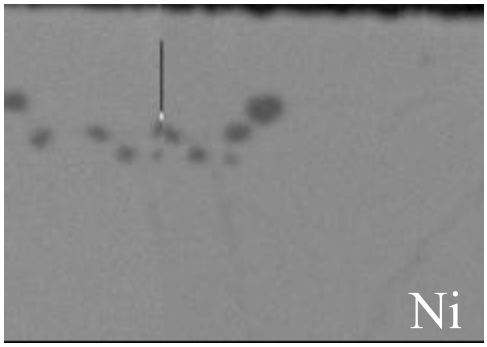


**(b)**

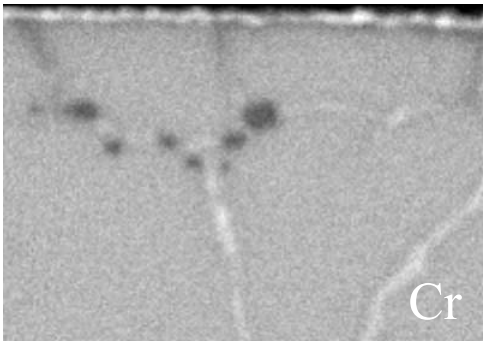


**(c)**

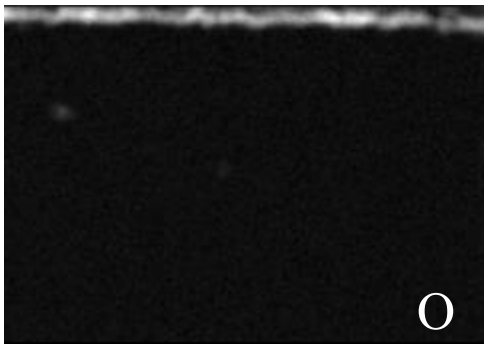


**(d)**

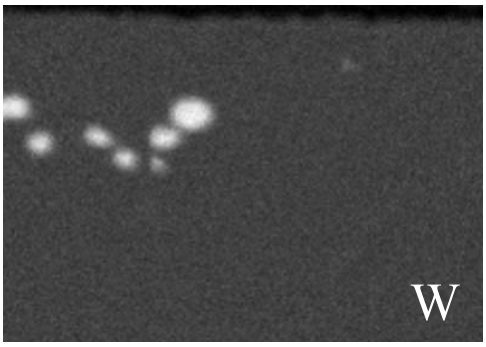


**(e)**

Figure 16: EPMA element maps of a 230-alloy specimen isothermally oxidized at 700°C – (a) Backscattered Image, (b) Ni, (c) Cr, (d) O, and (e) W.

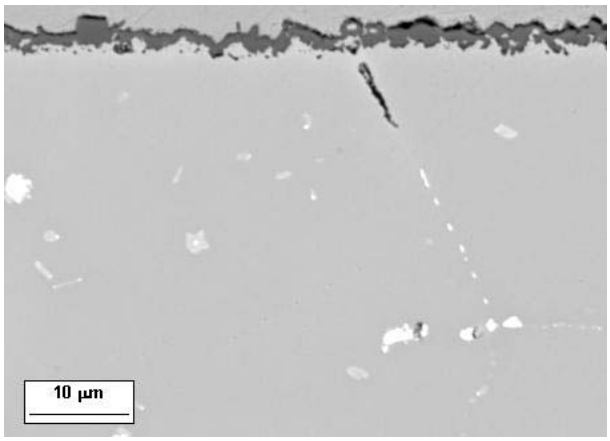


(a)

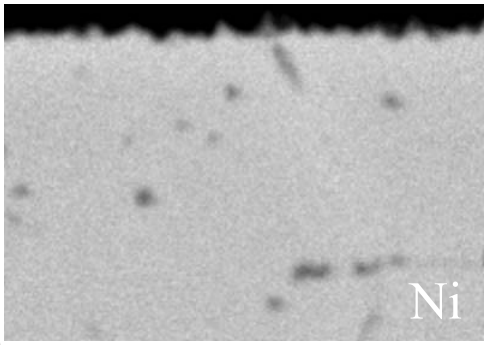


(b)

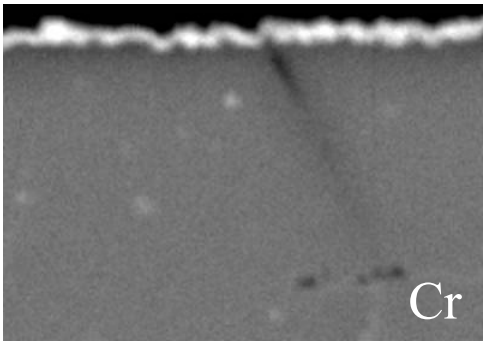


(c)

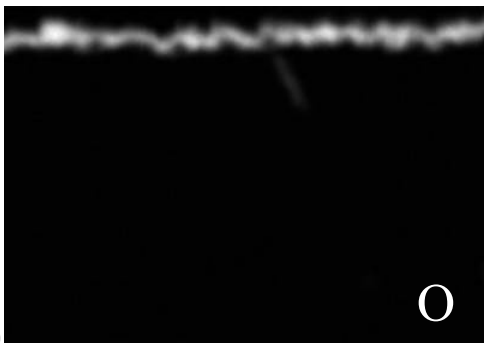


(d)

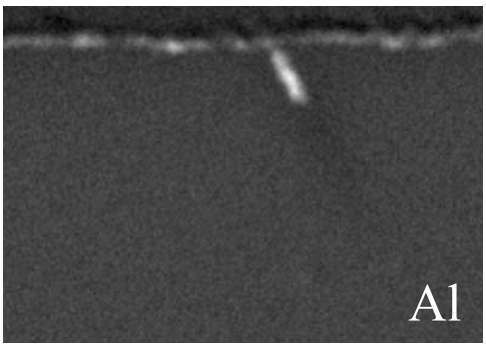


(e)

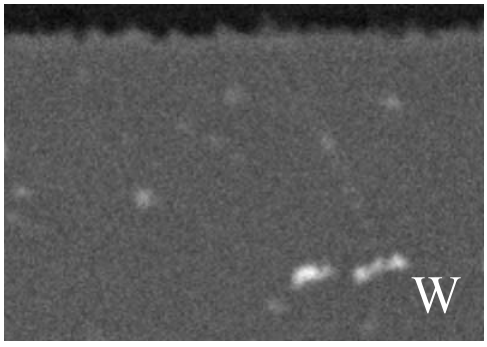


(f)

Figure 17: EPMA element maps of a 230-alloy specimen isothermally oxidized at 800°C – (a) Backscattered Image, (b) Ni, (c) Cr, (d) O, (e) Al, and (f) W.

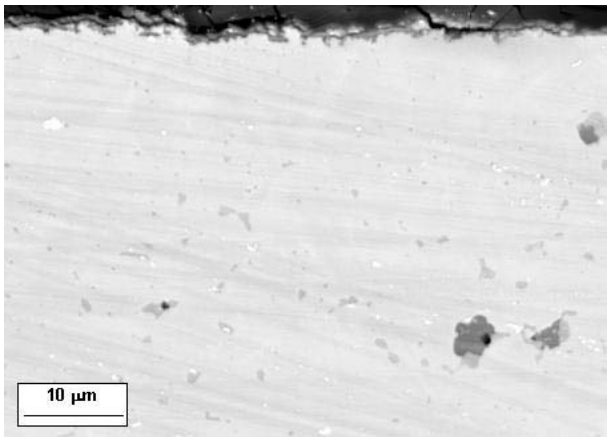


**(a)**

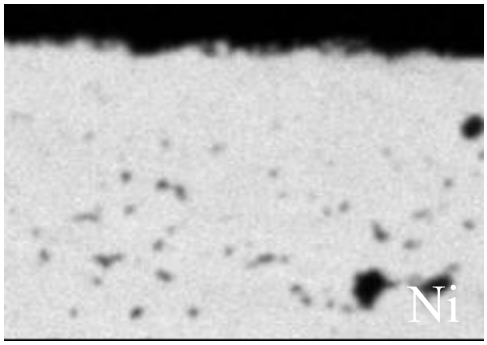


**(b)**

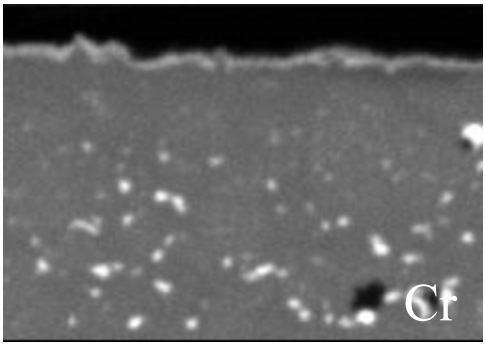


**(c)**

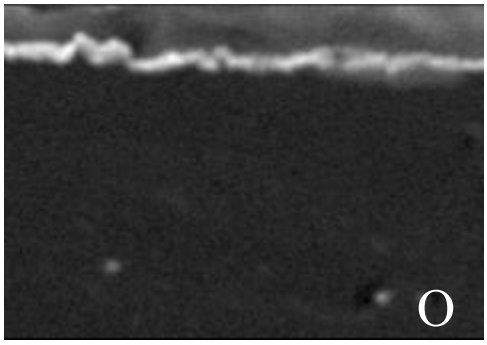


**(d)**

Figure 18: EPMA element maps of a 75-alloy specimen isothermally oxidized at 700°C and 37.7 MPa – (a) Backscattered Image, (b) Ni, (c) Cr, and (d) O.

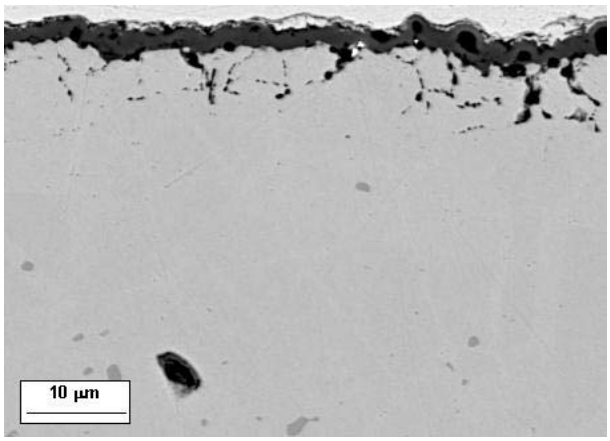


**(a)**

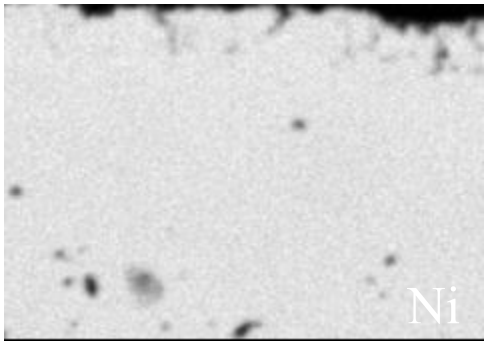


**(b)**

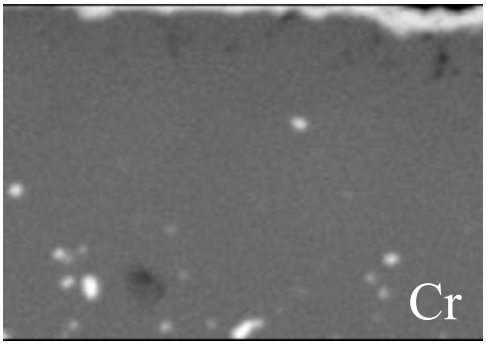


**(c)**

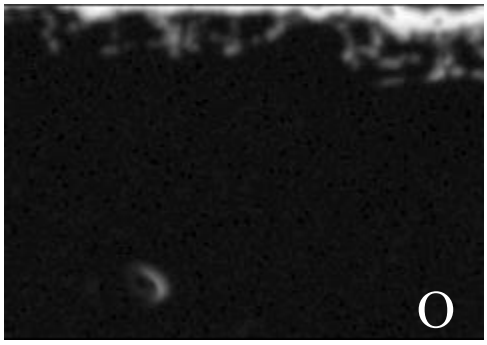


**(d)**

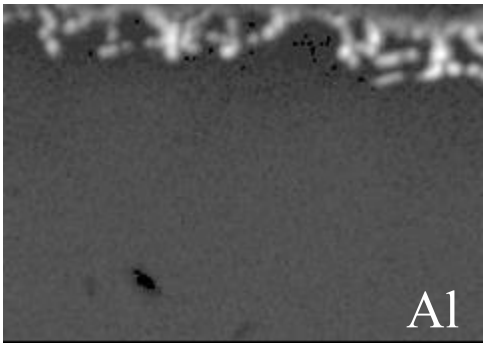


**(e)**

Figure 19: EPMA element maps of a 75-alloy specimen isothermally oxidized at 800°C and 13.5 MPa – (a) Backscattered Image, (b) Ni, (c) Cr, (d) O, and (e) Al.

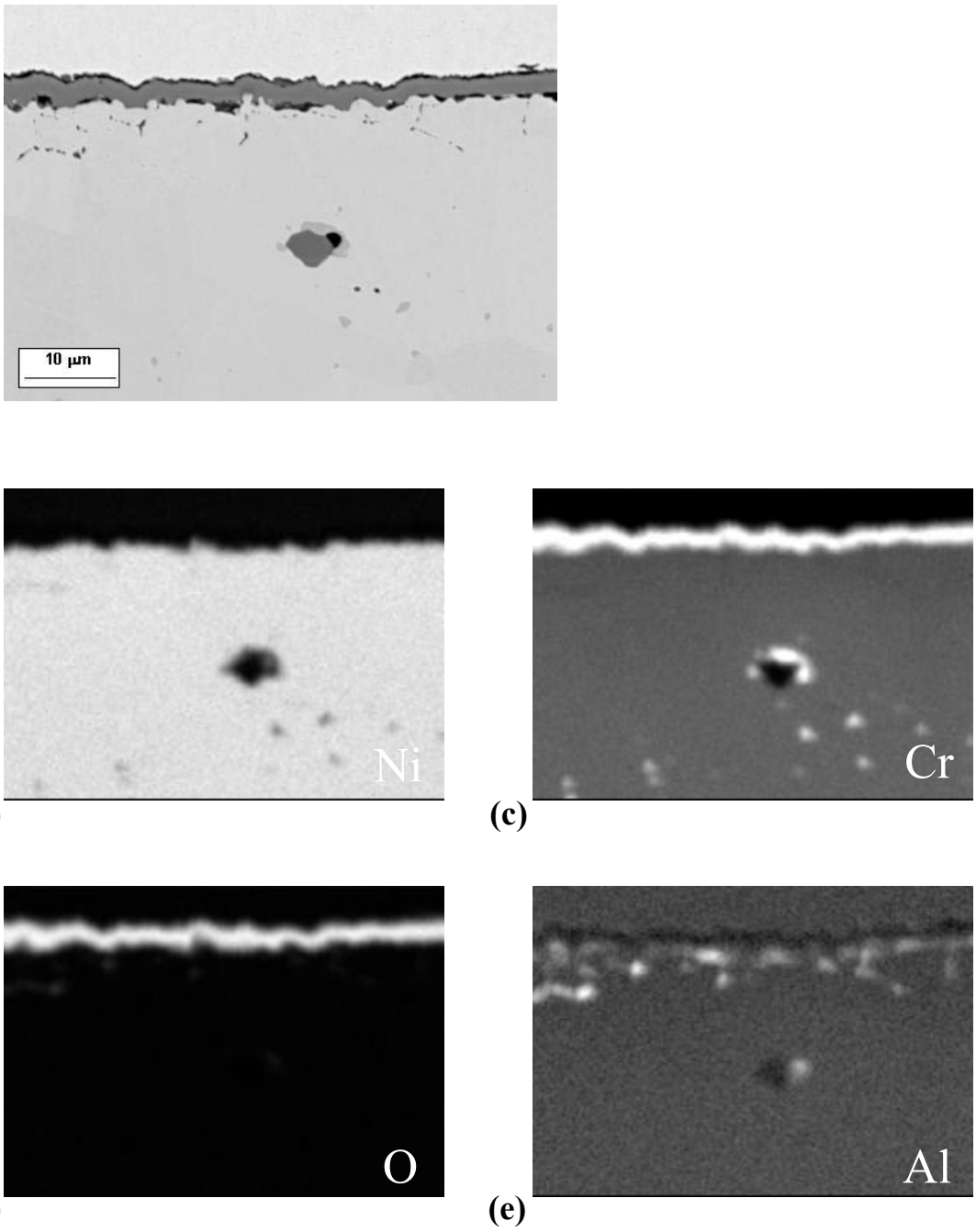


Figure 20: EPMA element maps of a 75-alloy specimen isothermally oxidized at 800°C and 6.7 MPa – (a) Backscattered Image, (b) Ni, (c) Cr, (d) O, and (e) Al.

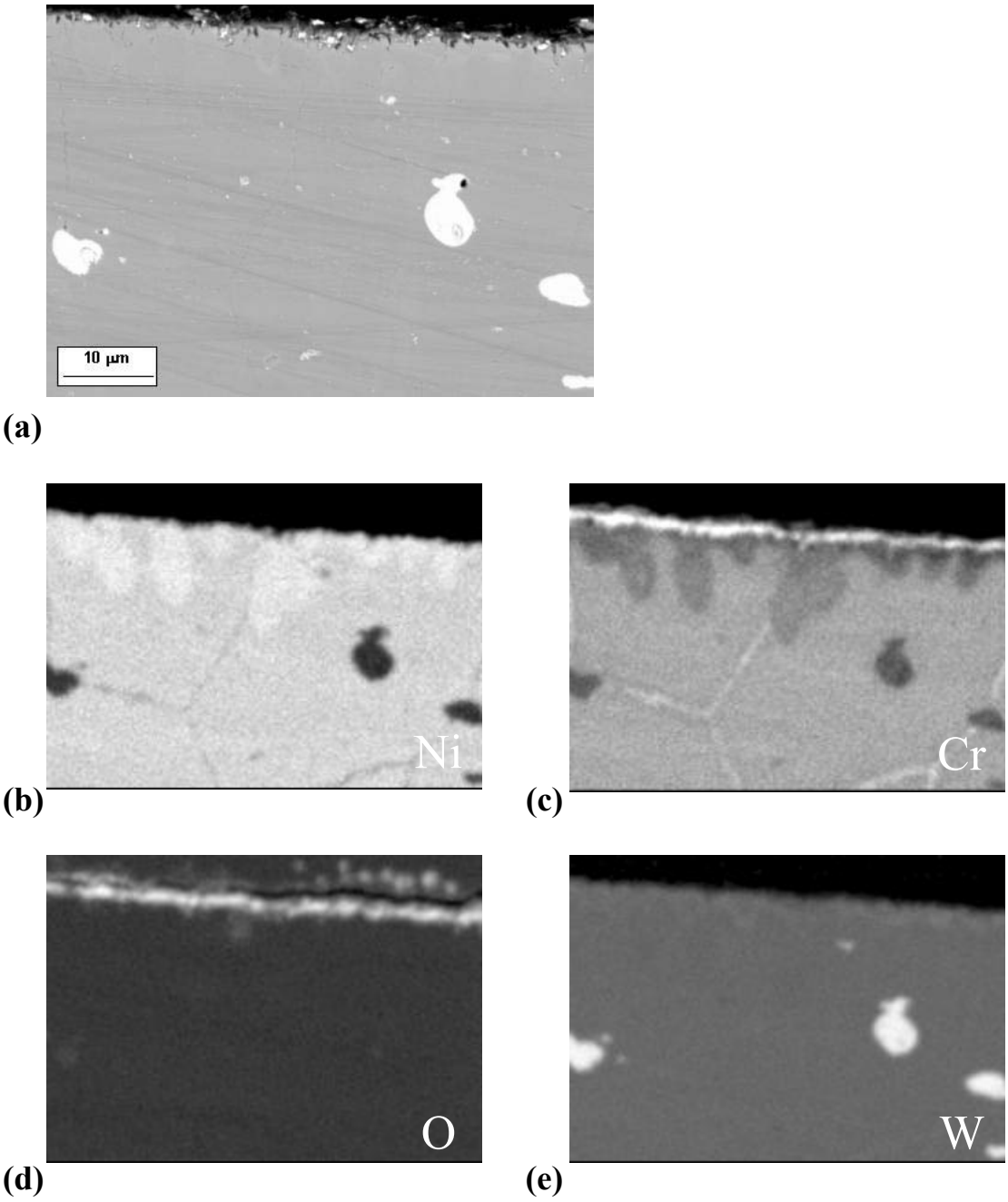


Figure 21: EPMA element maps of a 230-alloy specimen isothermally oxidized at 700°C and 133 MPa – (a) Backscattered Image, (b) Ni, (c) Cr, (d) O, and (e) W.

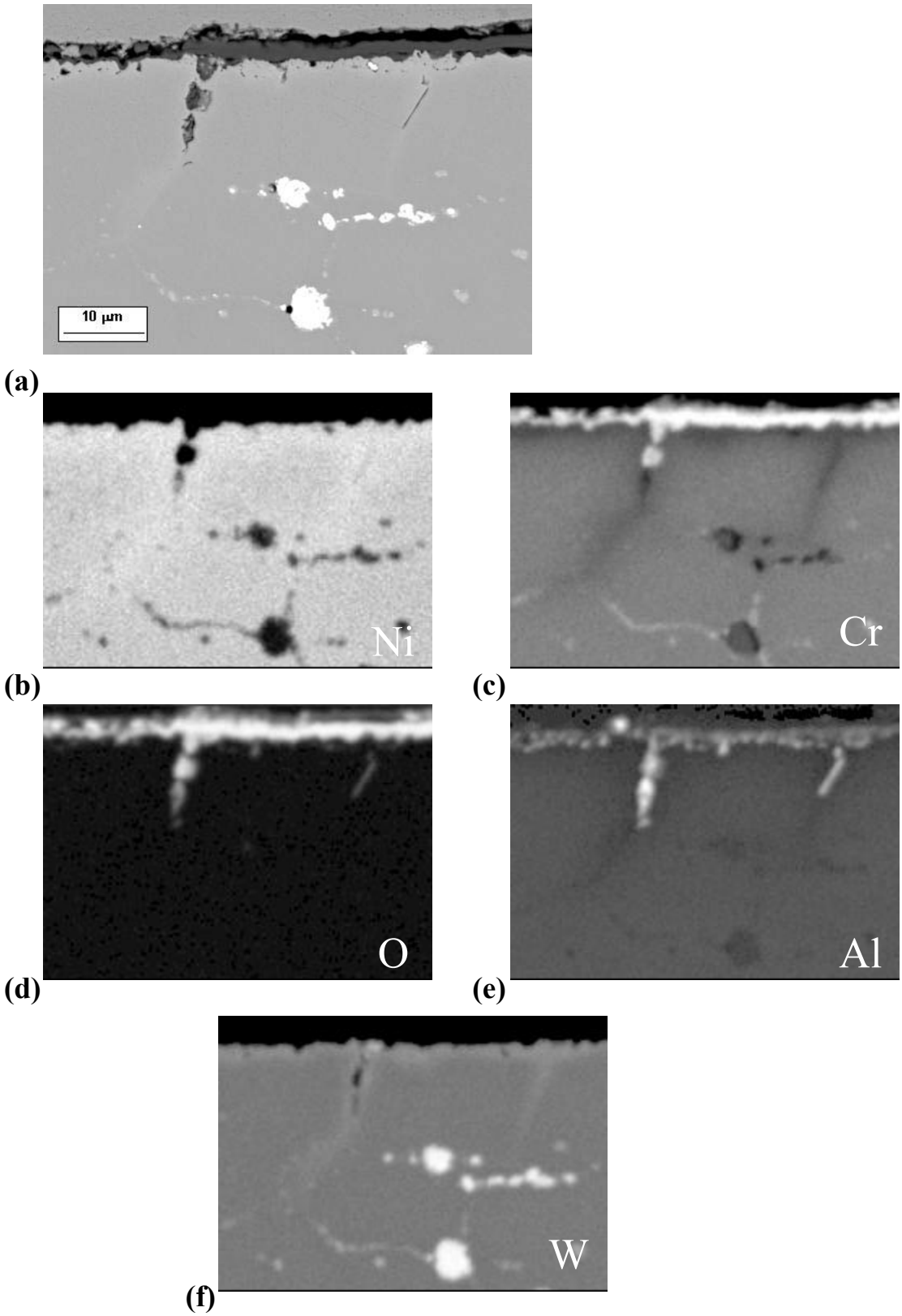


Figure 22: EPMA element maps of a 230-alloy specimen isothermally oxidized at 800°C and 72.5 MPa – (a) Backscattered Image, (b) Ni, (c) Cr, (d) O, (e) Al, and (f) W.

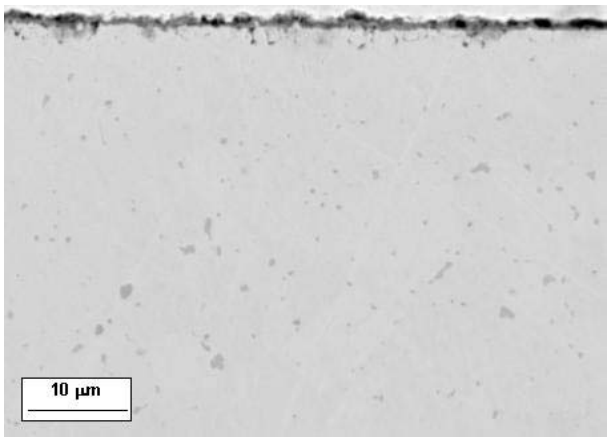


**(a)**

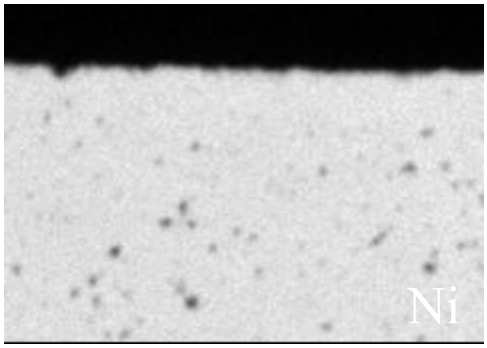


**(b)**

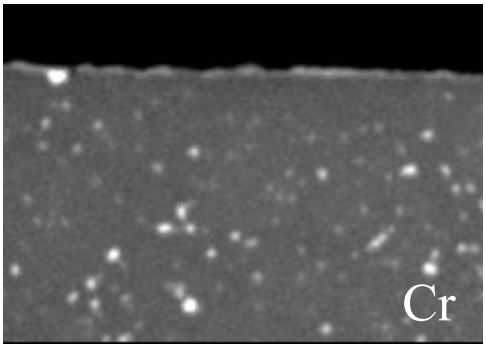


**(c)**

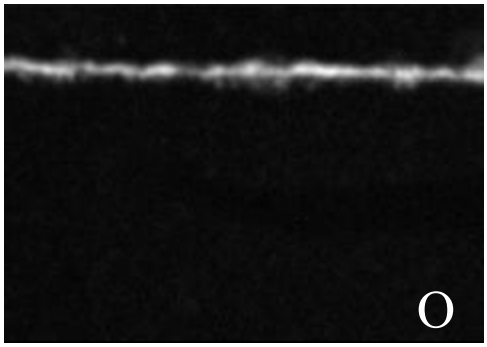


**(d)**

Figure 23: EPMA element maps of a 75-alloy specimen cyclically oxidized at 700°C – (a) Backscattered Image, (b) Ni, (c) Cr, and (d) O.

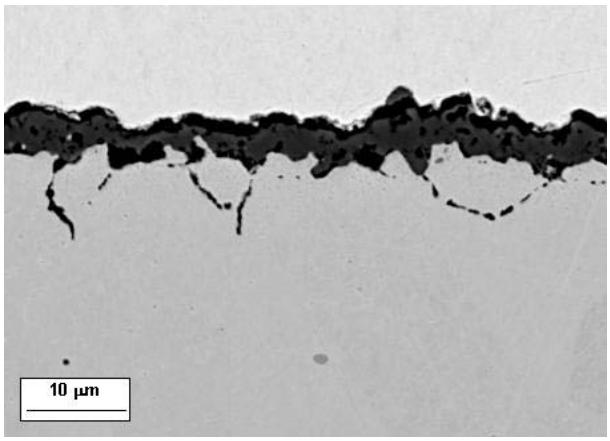


(a)

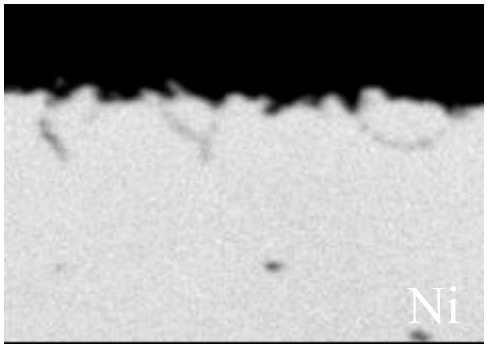


(b)

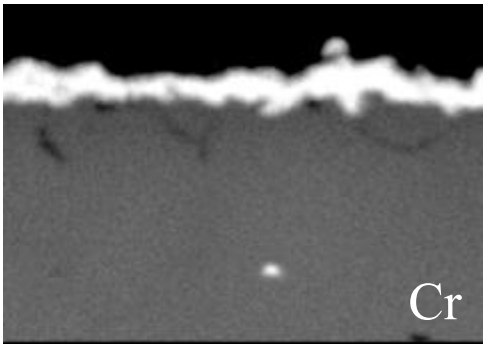


(c)

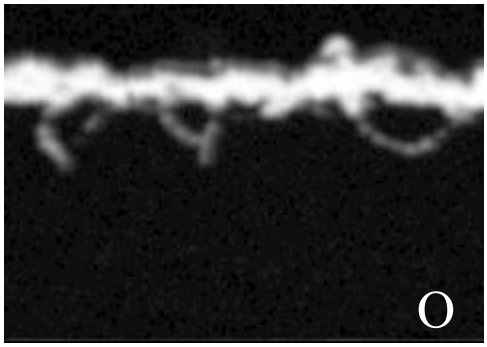


(d)

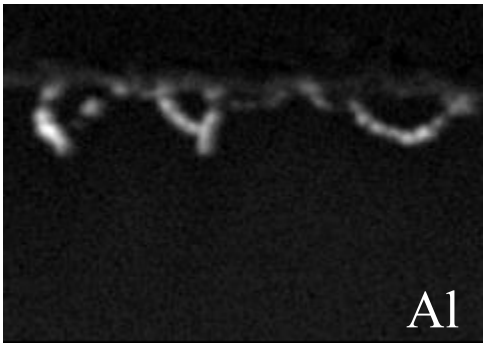


(e)

Figure 24: EPMA element maps of a 75-alloy specimen cyclically oxidized at 800°C – (a) Backscattered Image, (b) Ni, (c) Cr, (d) O, and (e) Al.

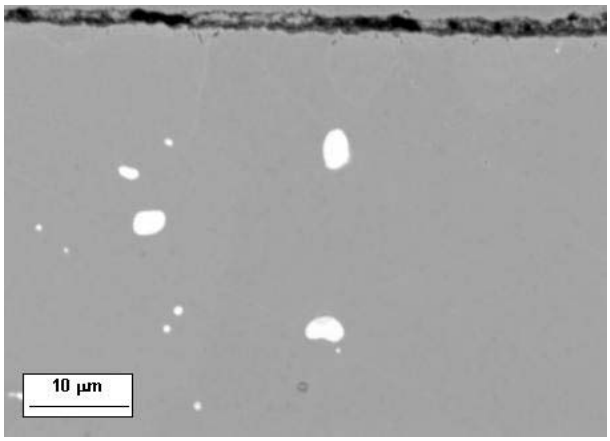


**(a)**

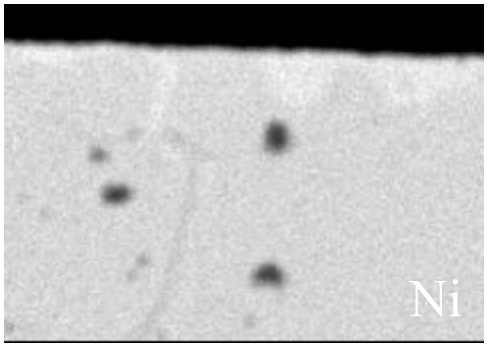


**(b)**

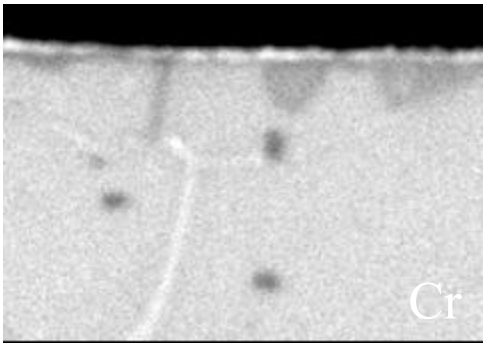


**(c)**

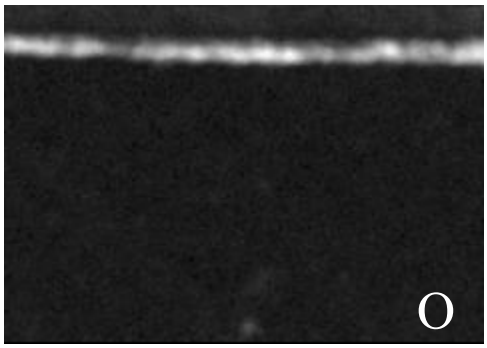


**(d)**

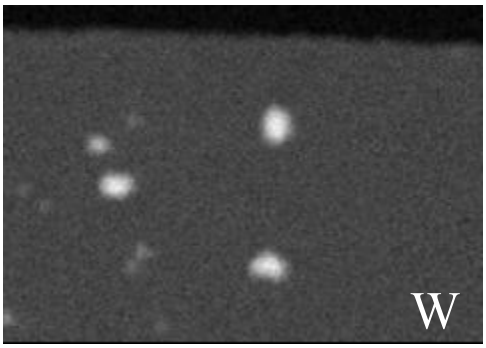


**(e)**

Figure 25: EPMA element maps of a 230-alloy specimen cyclically oxidized at 700°C – (a) Backscattered Image, (b) Ni, (c) Cr, (d) O, and (e) W.

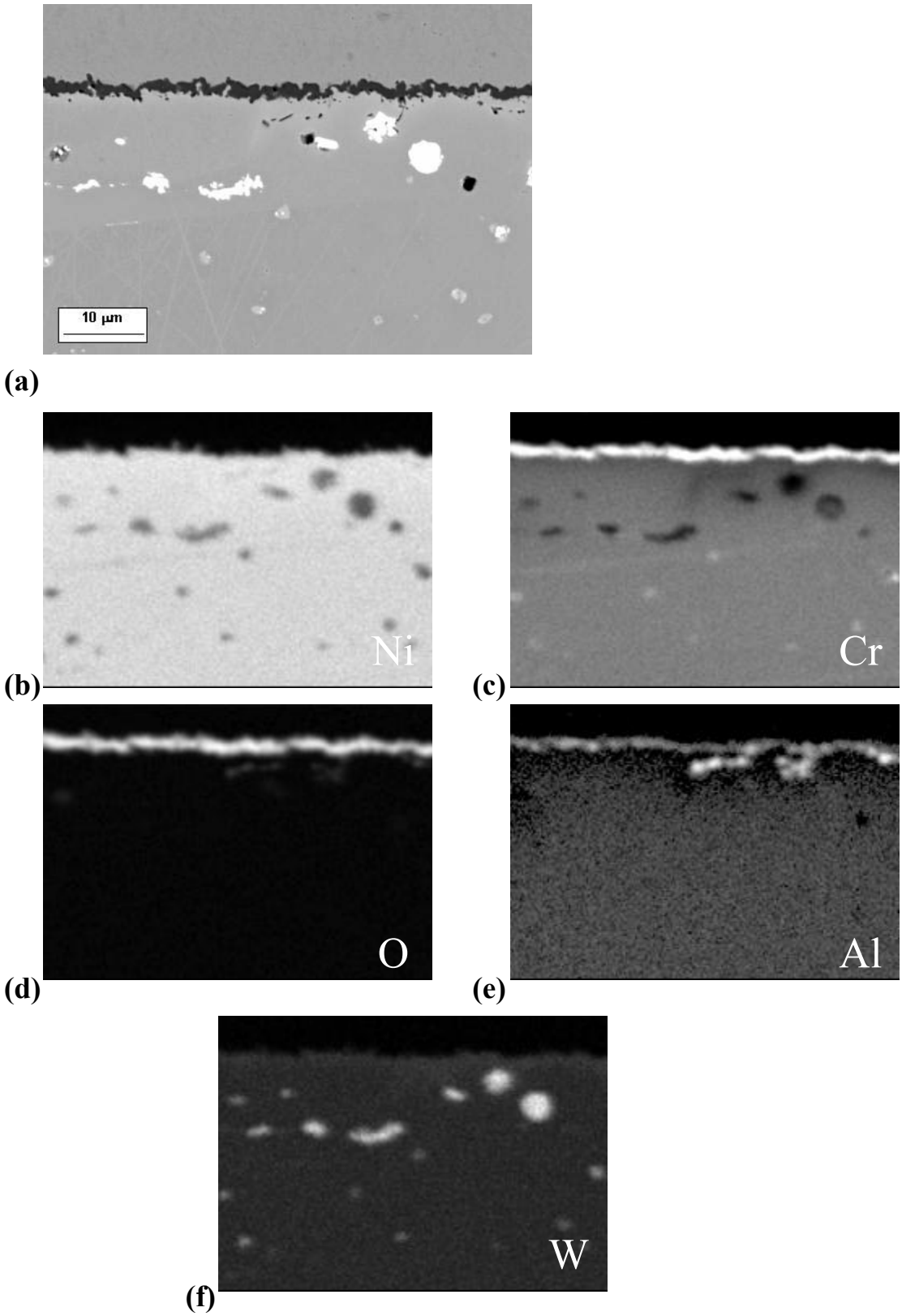


Figure 26: EPMA element maps of a 230-alloy specimen cyclically oxidized at 800°C – (a) Backscattered Image, (b) Ni, (c) Cr, (d) O, (e) Al, and (f) W.

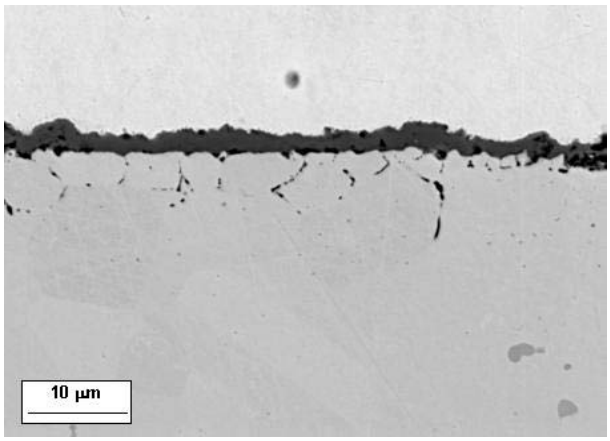


**(a)**

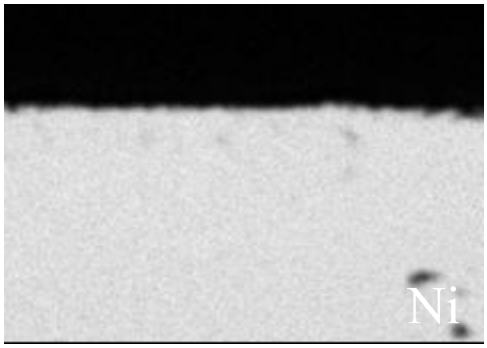


**(b)**

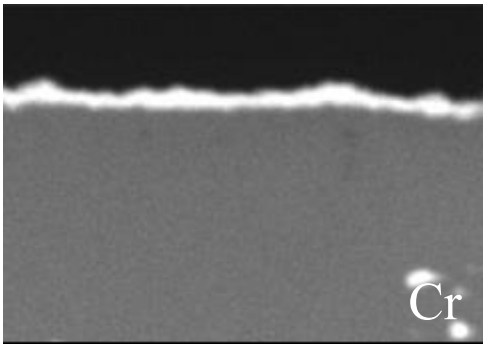


**(c)**

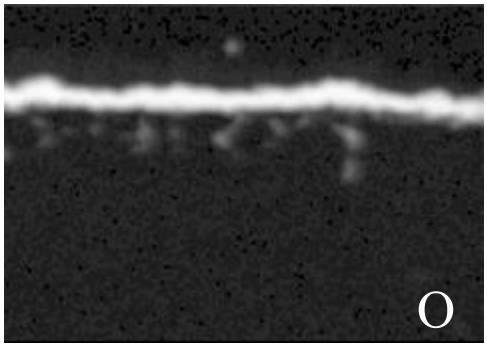


**(d)**

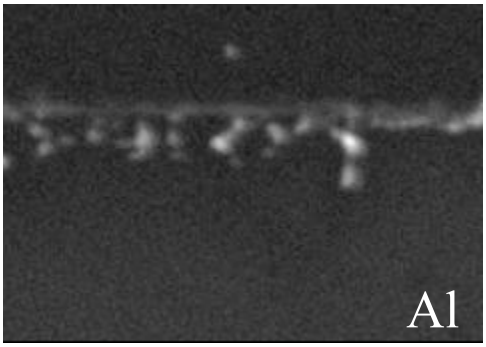


**(e)**

Figure 27: EPMA element maps of a 75-alloy specimen cyclically oxidized at 800°C and 6.7 MPa – (a) Backscattered Image, (b) Ni, (c) Cr, (d) O, and (e) Al.

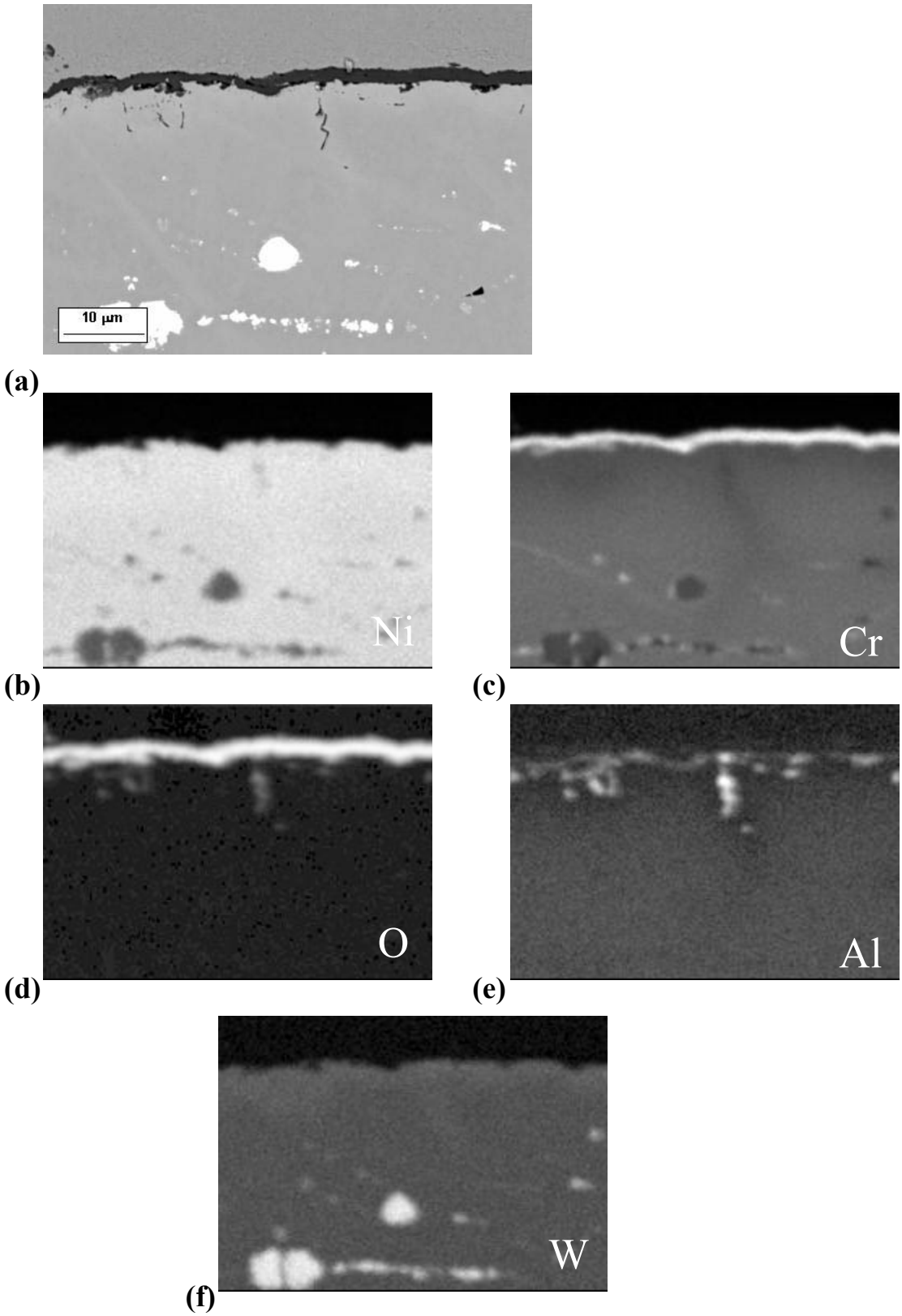


Figure 28: EPMA element maps of a 230-alloy specimen cyclically oxidized at 800°C and 72.5 MPa – (a) Backscattered Image, (b) Ni, (c) Cr, (d) O, (e) Al, and (f) W.

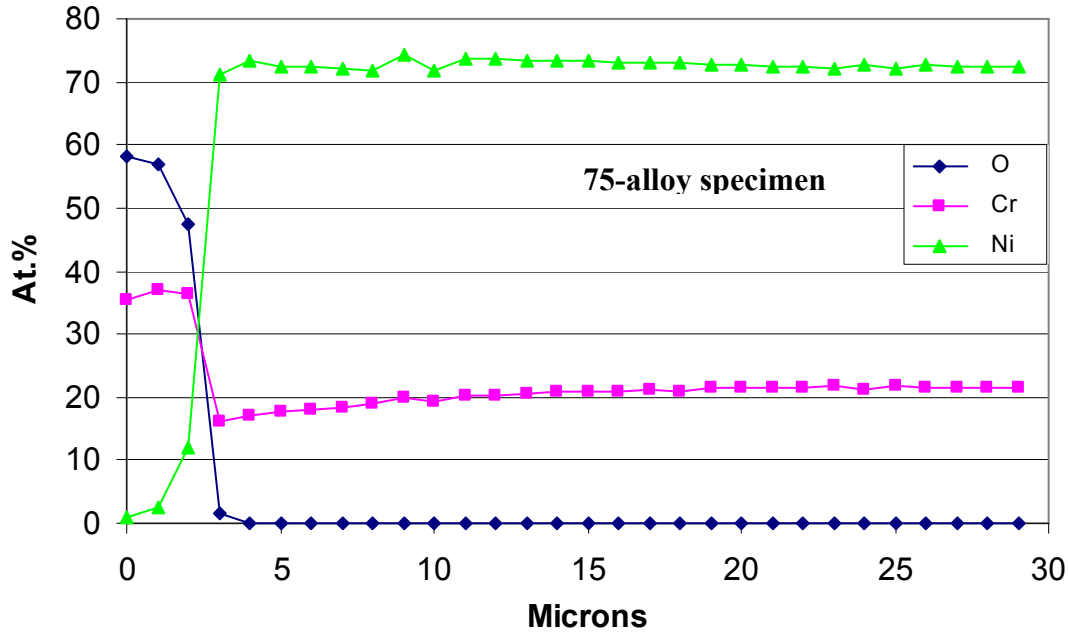


(a)

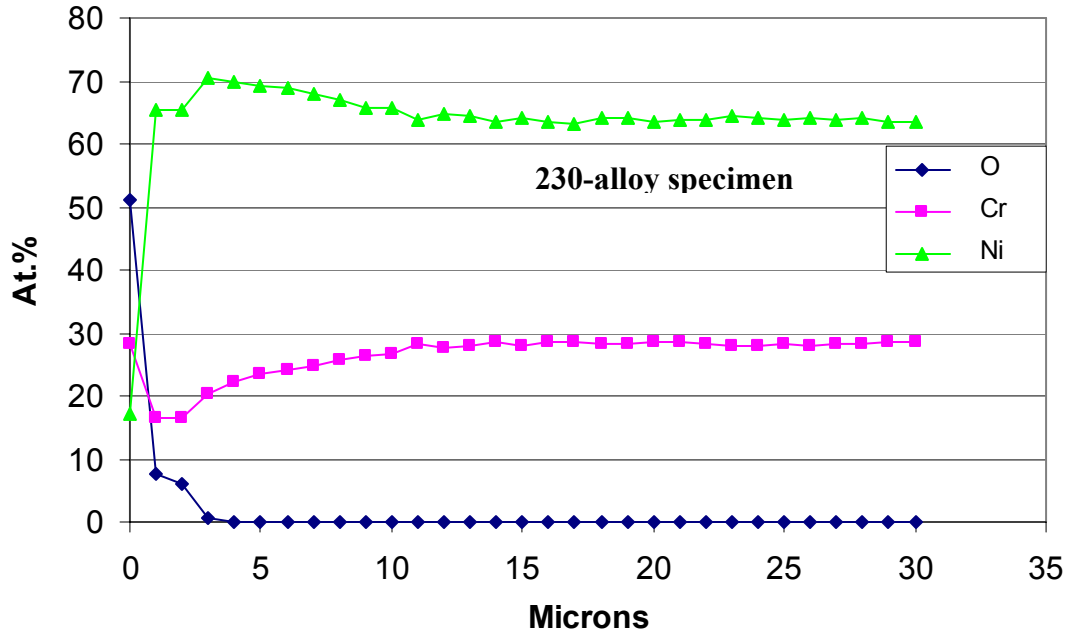


(b)

Figure 29: Composition vs. depth plots showcasing chromium depletion in (a) 75-alloy specimen oxidized cyclically at 800°C under no applied stress, and (b) 230-alloy specimen oxidized isothermally at 800°C under a stress of 72.5 MPa.

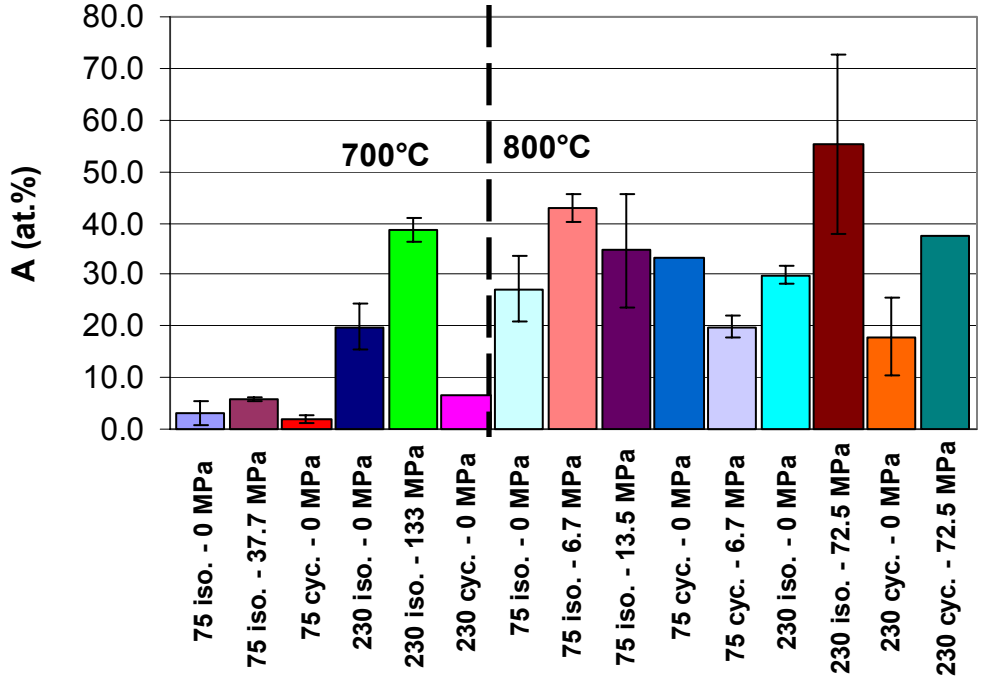


Figure 30: Bar graph of depletion-parameter data.

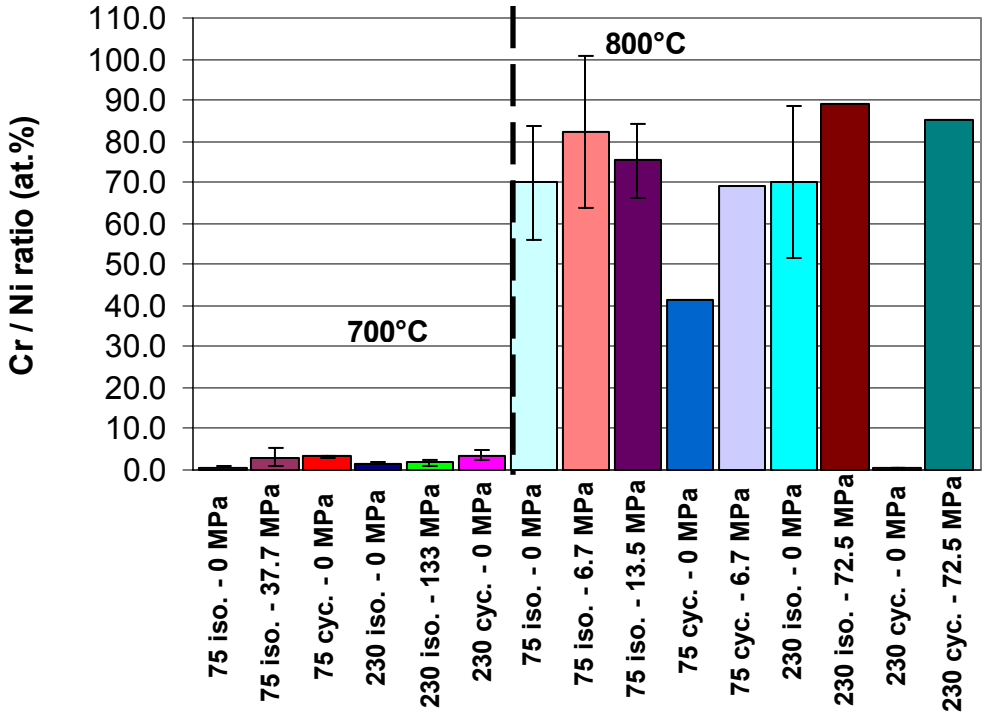


Figure 31: Bar graph of maximum Cr/Ni-ratio data.

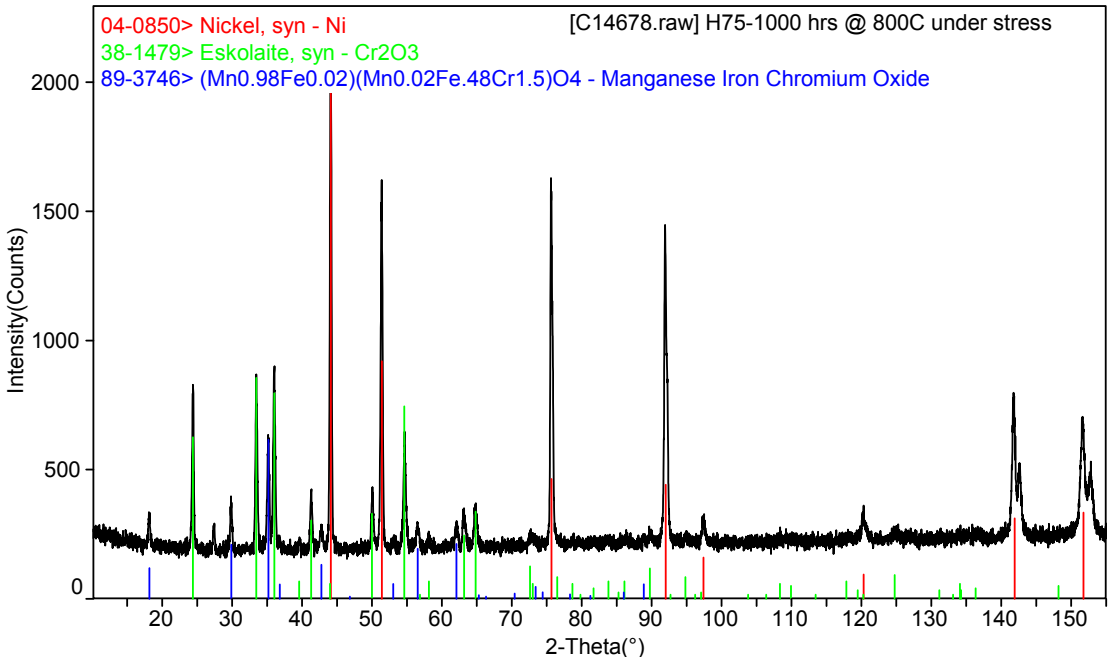


Figure 32: Theta-2theta scan for a 75-alloy specimen oxidized isothermally at 800˚C for 1,000 hours under an applied stress of 13.5 MPa obtained at a scan rate of one degree per minute.

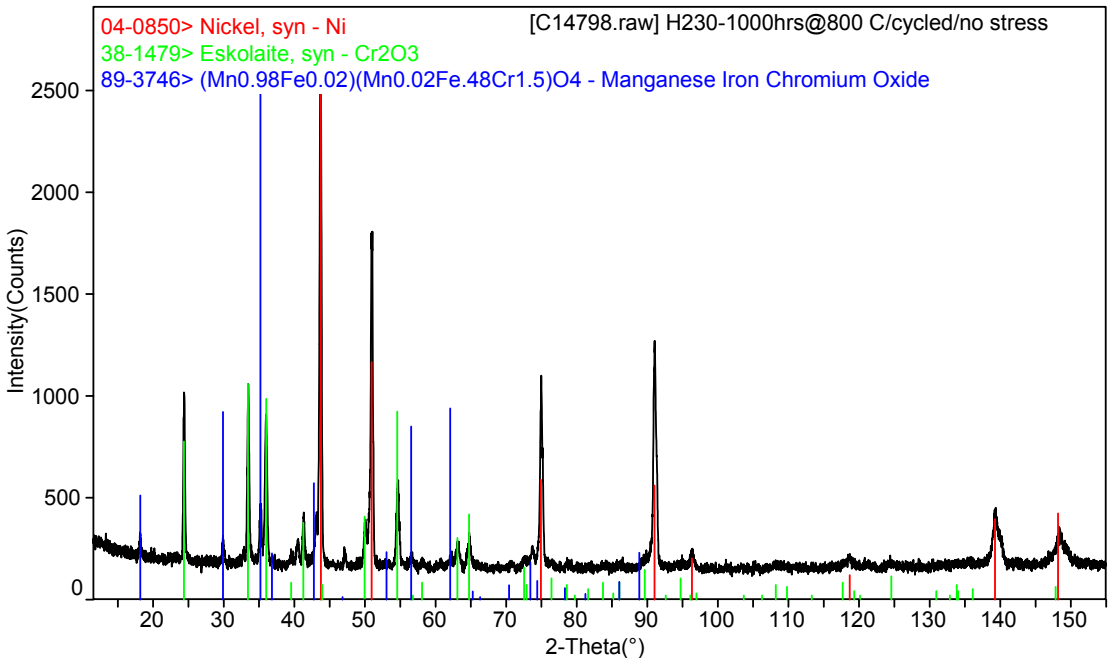


Figure 33: Theta-2theta scan for a 230-alloy specimen oxidized cyclically at 800˚C for 1,000 hours obtained at a scan rate of one degree per minute.

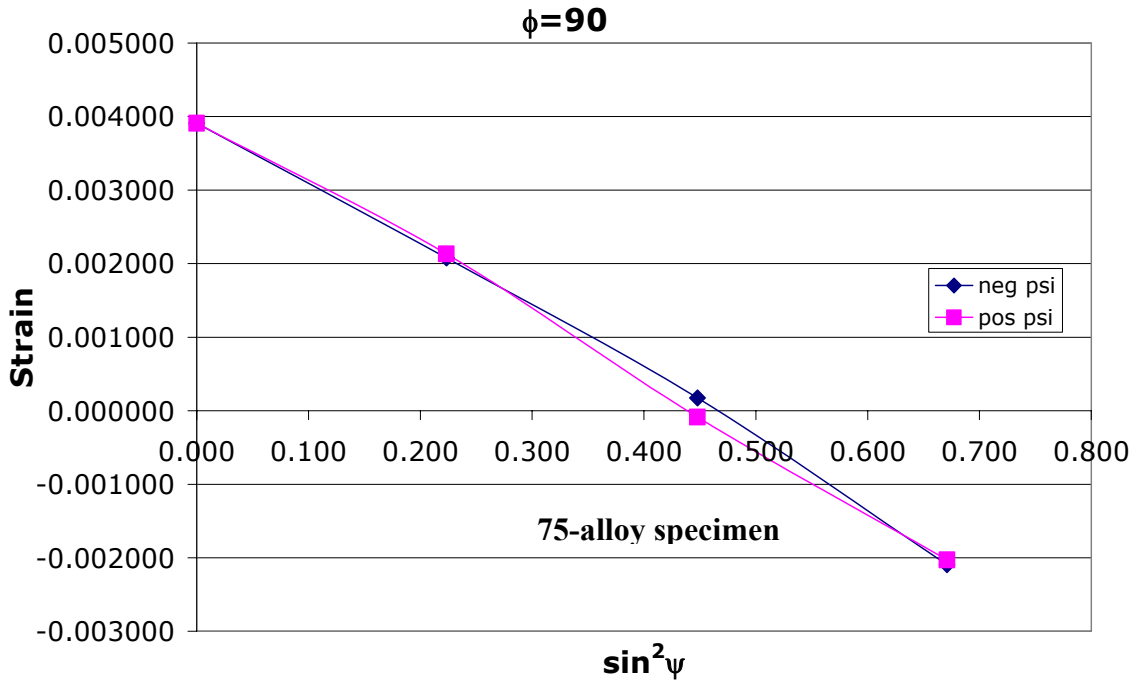


Figure 34: Strain vs. $\sin^2\psi$ plot for the (416) peak of a 75-alloy specimen oxidized isothermally at 800˚C for 1,000 hours under an applied stress of 6.7 MPa.

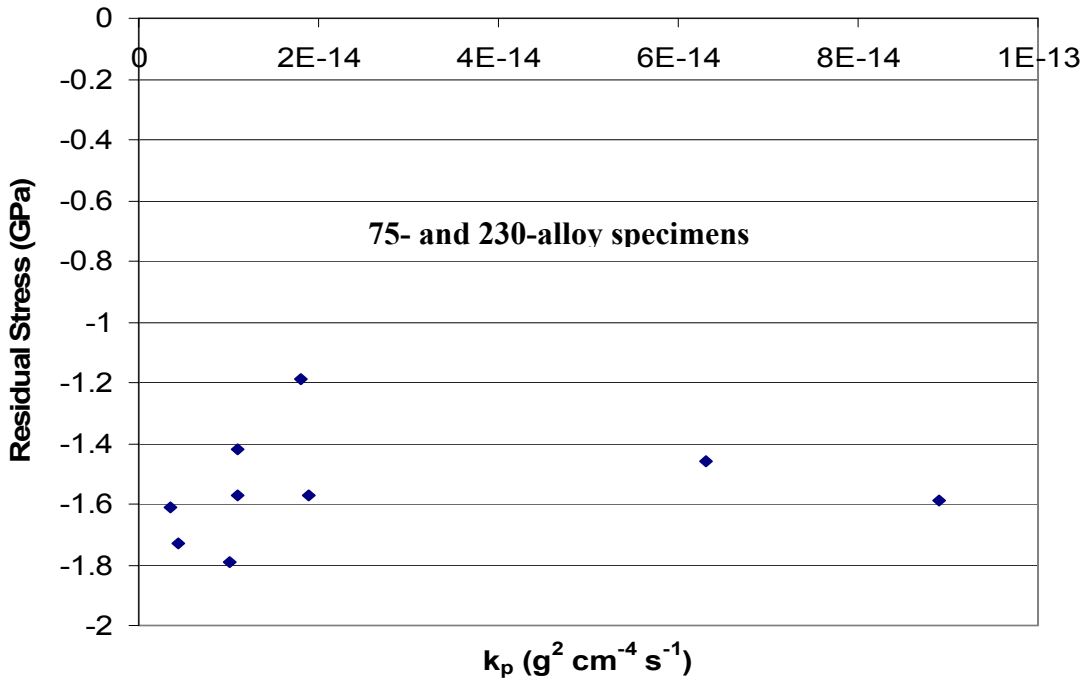


Figure 35: Residual stress vs. parabolic-oxidation-rate constant ($k_p$) for oxide (416) peaks.

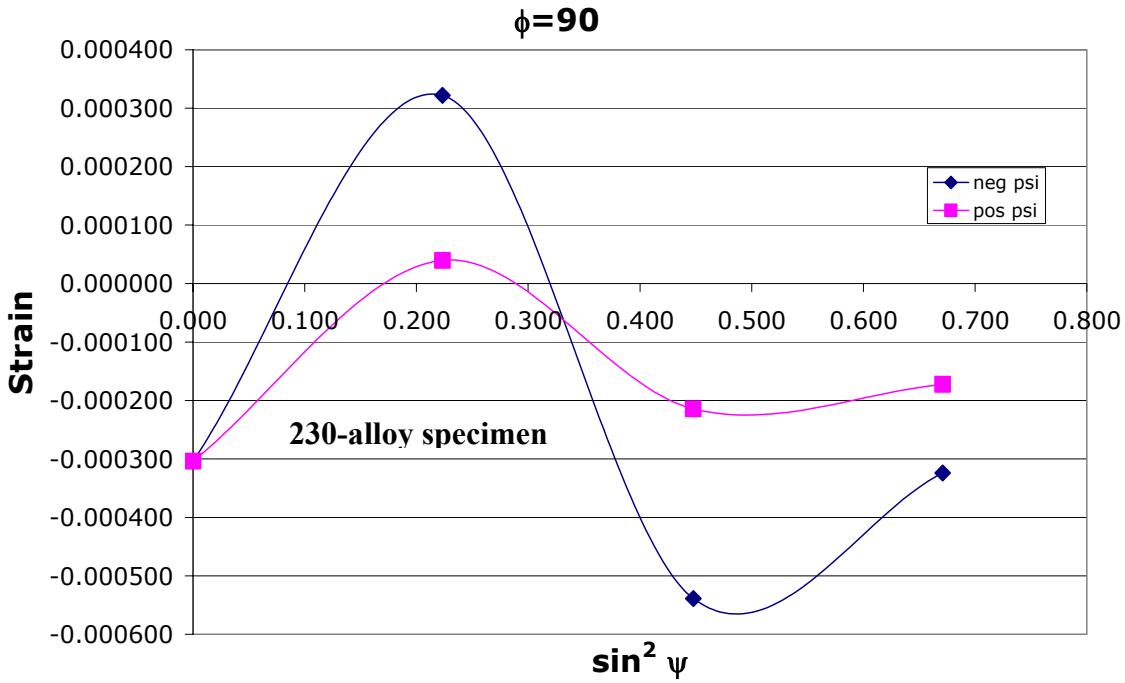


Figure 36: Strain vs. $\sin^2\psi$ plot for (420) peak of a 230-alloy specimen oxidized cyclically at 800˚C for 1,000 hours under an applied stress of 72.5 MPa.

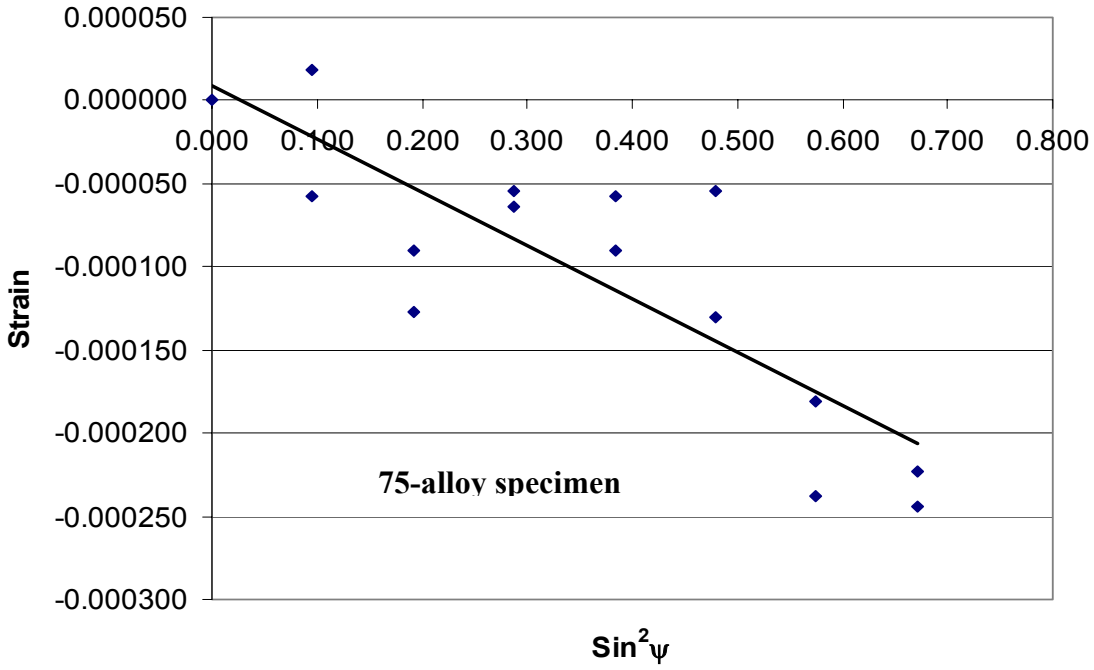


Figure 37: Strain vs. $\sin^2\psi$ plot for (331) peak of a 75-alloy specimen oxidized cyclically at 800˚C for 1,000 hours under an applied stress of 6.7 MPa.

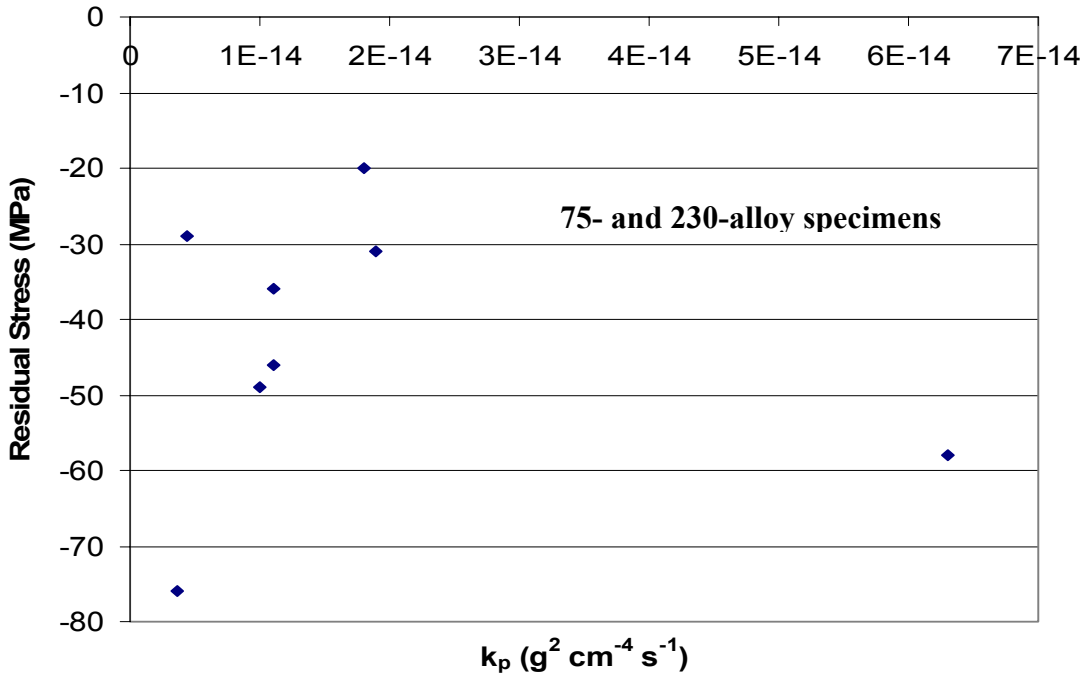


Figure 38: Residual stress in the substrates vs. parabolic-oxidation-rate constant ($k_p$) for averaged alloy (331) and (420) peaks.

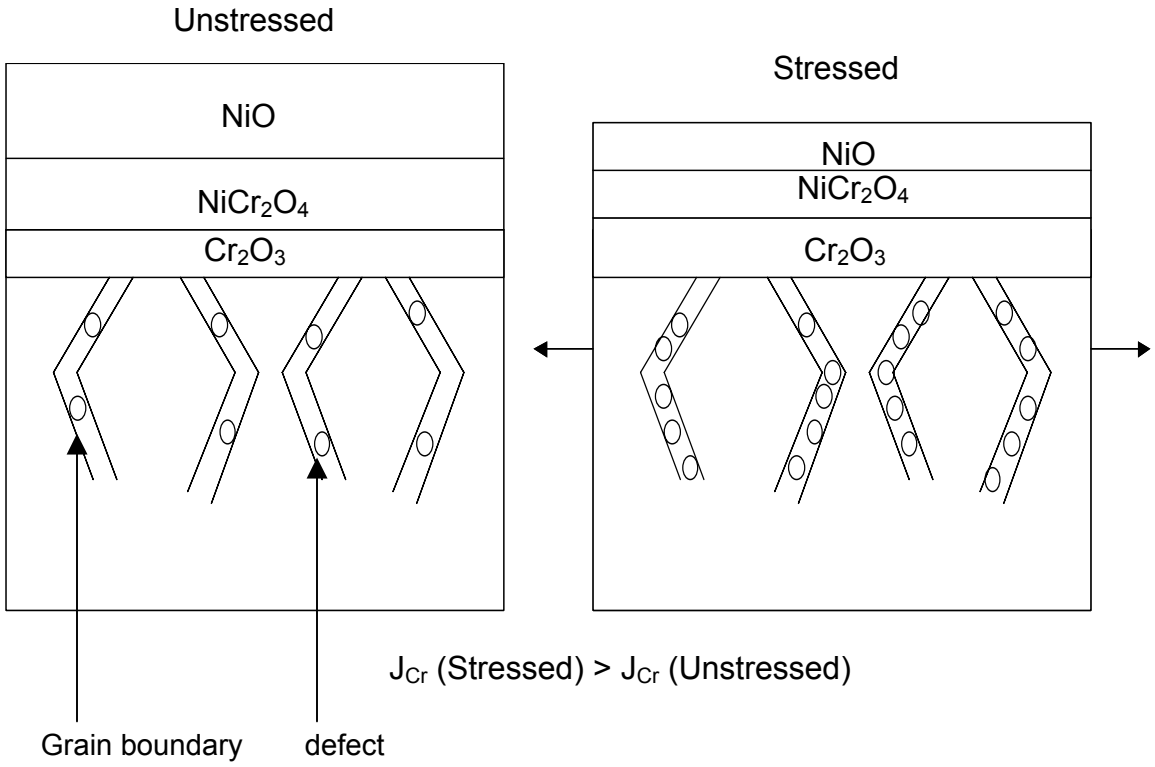


Figure 39: Schematic of the oxidation process in stressed and unstressed specimens.

# Vita

Mr. Bryan Barnard is a native of Strawberry Plains, TN. He is the son of Mr. Randall and Mrs. Darless Barnard. He obtained an A.S. degree in Pre-Engineering in 1998 and a General A.A. degree in 1999, both from Walters State Community College. He obtained his B.S. degree in Materials Science and Engineering from The University of Tennessee in 2002. He then entered graduate school in the Materials Science and Engineering Department at the University of Tennessee. He joined Professor Peter K. Liaw's research group where he worked with professionals at Oak Ridge National Laboratory, Wright-Patterson Air Force Base, and the California Institute of Technology. He published four journal articles, and obtained his M.S. in Materials.